UC Berkeley
UC Berkeley Electronic Theses and Dissertations

Title

Ring-shaped and Dual-electrode Bimorph Piezoelectric Micromachined Ultrasonic Transducers

Permalink

https://escholarship.org/uc/item/17b0s1c3

Author

Eovino, Benjamin

Publication Date

2018

Peer reviewed|Thesis/dissertation

Ring-shaped and Dual-electrode Bimorph Piezoelectric Micromachined Ultrasonic Transducers

by

Benjamin Eovino

A dissertation submitted in partial satisfaction of the

requirements for the degree of

Doctor of Philosophy

in

Engineering - Mechanical Engineering

in the

Graduate Division

of the

University of California, Berkeley

Committee in charge:

Professor Liwei Lin, Chair
Professor Tsu-Jae King Liu
Professor George C. Johnson

Fall 2018

Ring-shaped and Dual-electrode Bimorph Piezoelectric Micromachined Ultrasonic Transducers

Abstract

Ring-shaped and Dual-electrode Bimorph Piezoelectric Micromachined Ultrasonic Transducers

by

Benjamin Eovino

Doctor of Philosophy in Engineering - Mechanical Engineering

University of California, Berkeley

Professor Liwei Lin, Chair

The potential widespread usages of ultrasonic transducer technology have inspired the development of microelectromechanical systems (MEMS)-based devices. The research presented in this dissertation focuses on enhancing the performance of piezoelectric micromachined ultrasonic transducers (PMUTs) by devising innovative design structures, analytically deriving models to understand and optimize performance, and using these findings to demonstrate PMUT-based systems with increased capabilities. The ring-shaped PMUT is firstly introduced as a high-performance PMUT architecture, which is demonstrated both analytically and experimentally to show several important advantages over traditional designs. Due to specific effects of acoustic interactions that have not been previously studied, an extremely wide bandwidth can be achieved with aptly defined ring-shaped PMUTs in liquid-coupled operation. Specifically, fabricated devices are measured to have a velocity bandwidth of up to 160%, which is more than 60% greater than the highest bandwidth of any reported standalone PMUT and is tunable by altering device dimensions. PMUT arrays are used to demonstrate a new type of ultrasonic flow sensor that offers a robust, simple, and low-power chip-scale solution. The sensor operates in the pulse-echo mode to detect changes in flow with a measured sensitivity that is 286% of that for previously reported MUT-based flow meters, all without commanding any voltage over 5 V. The enhancement is a result of four unique features reported herein: (1) the high-sensitivity bimorph structure of the fabricated PMUTs; (2) the spatial separation between the transmitter and receiver transducer elements; (3) the high directivity of the transmitted acoustic pulse; and (4) the differential readout. Finally, arrays of PMUTs are also proposed for high intensity applications, beginning with the development of an equivalent circuit network model that accounts for the inter-transducer acoustic coupling and leads to

practical design equations with interesting implications for the design of high-power arrays. The findings are corroborated by experimental results from several fabricated prototypes, which also use electronic phased array focusing to achieve acoustic outputs that demonstrate feasibility for many high-intensity applications, especially for those requiring small transducer sizes. The prototype device exhibits an output pressure as high as $3.2 \ \mathrm{kPa/V}$ in standard transmission, which can be boosted to $12.2 \ \mathrm{kPa/V}$ by applying phased array focusing at a depth of 2 mm. Furthermore, a linear relationship between focal pressure and applied voltage is observed with a maximum measured pressure of $187 \ \mathrm{kPa}$ peak-to-peak, demonstrating feasibility to reach the intensity ranges required for medical operations in the future.

To my parents: Paul and Sandi

Contents

List of Figures

List of Tables

Acknowledgments

Looking back on my last nine years of university education and all the lessons learned along the way, both academic and otherwise, none stand out more than the realization that nothing of significance is ever achieved alone. The culmination of this PhD work is no exception; my own contributions to this accomplishment have been equaled, if not surpassed, by the relentless support of all the amazing people in my life and the stimulating, vibrant environments they created.

Along these lines, I would first and foremost like to thank my incredible parents Paul and Sandi. They have instilled in me the values of hard work, dedication, doing right by others, and most importantly, living with balance (they have more fun than me these days!). For every milestone - and roadblock - their perspective and unconditional support was never far behind. To them both: you have always managed to bring the best out in me, and I am truly grateful for all you do.

I would also like to thank my PhD advisor, Professor Liwei Lin. Throughout the past three years he gave me the independence to explore, expand, and direct my academic interests - a freedom that I do not take for granted, and gained an immense amount from. My journey to graduate school began when I was fortunate enough to have the excitement and passion of my undergraduate research advisor Professor Sumita Pennathur rub off on me while working in her lab. I thank her for taking an active stance on inspiring young students such as myself to push themselves and pursue success, and look forward to seeing many more come from her lab in the future. I also deeply appreciate the insights and advice from my dissertation committee, Professors George Johnson and Tsu-Jae King Liu.

I have been extremely fortunate to work beside such great labmates in my time at UC Berkeley. To Joy Jiang, Yichuan Wu, Hyun Sung Park, Levent Beker, Simon Liu, Hong Ding, Emmeline Kao, Ilbey Karakurt, and so many others, I appreciate all the help and stimulating discussions, and will always look back on the good times we had. Special thanks goes out to Sina Akhbari, who laid the groundwork for much of my PhD research and taught me the ins and outs of PMUTs when I joined the lab; much of what I was able to accomplish would not have been possible without your initial guidance. Now as I leave, I know the project is in good hands with Luna Liang, and I am excited to see all the interesting advancements that will be thought up under her watch. In the course of this project, all fabrication was done in the Marvell Nanofabrication Laboratory at UC Berkeley, and I am indebted to the incredibly knowledgeable staff there for all their help and guidance.

Outside of the lab, I am lucky to have taken part in the rich and profoundly different cultures at UC Santa Barbara and Berkeley. The former brought me balance, especially with the help of my lifelong friends Sloane Viola, Tyler Wilson, Mara Howes, Shaun Moinpour, Mia Weber, and Mark Simon - you all taught me not to take work too seriously but to stay dedicated, both of which have come in handy countless times. At UC Berkeley, I was constantly surrounded by some of

the most intelligent minds I will ever know, and grew more than I ever thought possible. Thanks to my great friends who made my time there rewarding and fun - Brett Kelly, Nick Errico, Jessica Lee, Anna D'Alessio, Hannah Gramling, and many others. And to my brother Matt who, if I may ever justifiably claim any semblance of mental toughness, is undoubtedly the one responsible. All kidding aside, while our reunions may be too few and far between, our shenanigans are always a much-needed escape from the world, and knowing I can count on your judgment-free, honest opinions has helped me more than I can say throughout the years.

And last but not least, miss Vida Mae Fernandez. My rock. You have exposed me to a whole new refreshing world outside my engineering bubble, and the pure happiness you bring to my life has gotten me through more than you know. It is no stretch to say that whatever I may have accomplished in this dissertation, you have had a hand in as well. I look forward to all the adventures (and free time!) to come.

Chapter 1

Introduction

From its advent as a method of detecting submarines in World War I, ultrasound technology has evolved into an appealing platform in a host of applications over the last century. Specifically, ultrasound is now: (1) the gold standard in many instances of medical diagnostics and imaging [1]; (2) widely used in non-destructive testing for structural integrity [2]; (3) a reliable method for object detection and rangefinding [3]; and (4) utilized for its beneficial therapeutic effects in medical operations, including hyperthermia for cancer treatment, lithotripsy for noninvasive surgery, and low-intensity pulsed ultrasound (LIPUS) for accelerated healing of tissue and bone [4], [5].

The structure and operating principle of standard ultrasonic transducers (UTs) is described by using a medical ultrasound probe as an illustrative example in Figure 1.1. Conventional UTs rely on thickness-mode vibrations of piezoelectric elements, most commonly lead zirconate titanate (PZT), mounted on a backing material to transmit and receive acoustic signals [6] as shown in the expanded view of Figure 1.1. This operation is typically characterized by a large impedance mismatch with the acoustic medium, making mechanoacoustic transduction inefficient and limiting axial resolution [7]. The addition of a matching layer somewhat mitigates this issue, however it does so at the expense of added fabrication complexity, especially considering the tight tolerances required in the layer thickness and the effects of the required adhesion material. Such fabrication complexities complicate an already labor intensive manufacturing process [8]: the transduction element is traditionally formed by pressing and sintering PZT powder, which is then lapped, polished, and diced to the narrow element width shown in Figure 1.1 before finally being attached to the backing. As a result of their heavily involved processing, conventional UTs can suffer from low yield [9], which precludes their use in mass-produced consumer electronics. Furthermore, their large form-factor and high power consumption rule out most portable applications [10], [11].
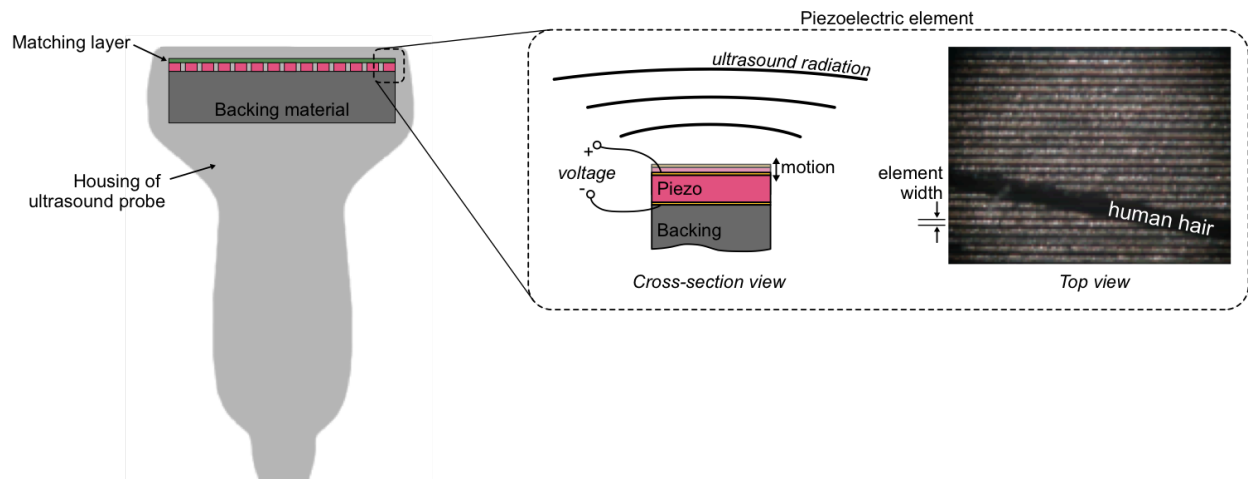
Figure 1.1: Conceptual diagram of the structure and operating principle of a medical ultrasound probe. Piezoelectric element top view image from *http://www.ndk.com/en/sensor*.

1.1 Micromachined Ultrasonic Transducers

In recent years, researchers have developed microelectromechanical systems (MEMS)-based ultrasound devices that alleviate many of the aforementioned issues with conventional UTs [12]. The structure of micromachined ultrasonic transducers (MUTs) is typically that of a diaphragm clamped around its periphery as shown in Figure 1.2; flexural vibrations afford MUTs a lower acoustic impedance which more closely matches that of the surrounding medium, resulting in wider bandwidths and higher efficiencies than that of conventional ultrasound devices without requiring matching layers [13]. By vibrating in the flexural mode rather than the thickness mode, the resonance frequency of MUTs is defined by lateral dimensions and the diaphragm thickness, allowing a wide range of frequencies to be reached as dictated by the specific application. Additionally, MUTs draw from well-established MEMS fabrication processes, allowing for high yield, batch processing, small form-factors, and integration with CMOS electronics [14].

MUTs are typically classified as either capacitive (CMUTs) [15] or piezoelectric (PMUTs) [16] based on their transduction mechanisms, which are conceptually explained in Figure 1.2. In transmission, an applied voltage leads to a vertical electrostatic force on the diaphragm of a CMUT causing out of plane vibrations. Conversely, PMUTs are actuated by the 31-mode piezoelectric effect: an applied vertical electric field induces an in-plane piezoelectric stress that is offset from the neutral axis of the diaphragm due to the elastic layer, and is therefore translated into a bending moment and out of plane motion. When receiving ultrasound, the converse of these effects results in the generation of an electrical signal. In general, CMUTs exhibit higher electromechanical coupling and bandwidth, but suffer from inherently nonlinear operation, the need for large bias voltages, reliability issues associated with dielectric charging, and limited displacements (and
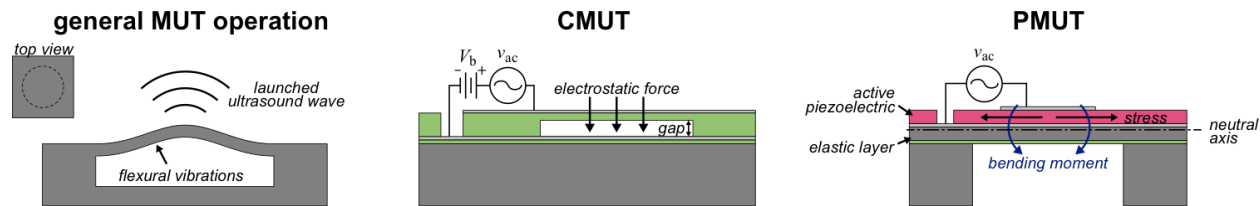
Figure 1.2: Schematic illustration of the general operation of a MUT (left), along with the mechanisms by which electromechanical transduction occurs in CMUTs (middle) and PMUTs (right).

therefore output pressures) due to small transduction gaps [17], [18]. Conversely, PMUTs typically use PZT or aluminum nitride (AlN) as a piezoelectric and have lower efficiencies and bandwidths than CMUTs, but exhibit linear responses and are capable of large displacements. Furthermore, the lack of high DC bias voltage makes PMUTs uniquely suited for battery-powered mobile devices and in-vivo applications [19], [20]. As such, the topic of improving the performance of PMUTs has garnered much attention in recent research endeavors, including those presented in this dissertation.

1.2 Performance Metrics and Prior Works

In order to understand what metrics are used to quantify PMUT performance, it is helpful to establish how the transducers are typically characterized and operated. Two prominent examples are the frequency response and pulse-echo measurement, shown in Figures 1.3(a) and (b), respectively. In a frequency response, the PMUT is driven and its displacement or velocity is measured at each frequency of interest. MUTs typically behave as single degree of freedom mass-spring-damper systems, so that their frequency response is characterized by a peak velocity u_p at a resonance frequency f_0 and with a 3 dB fractional bandwidth BW_f that is the inverse of the quality factor Q, i.e., $BW_f = 1/Q$. In pulse-echo operation, the PMUT is driven at its resonance frequency with a few pulses to transmit ultrasound, at which point it switches operation modes to a receiver and the acoustic echoes from surrounding objects are measured. Pulse-echo is fundamentally how imaging ultrasound systems operate, and is also utilized in object detection and rangefinding. With these measurement schemes in mind, the importance of the performance metrics revealed by each will be examined in the next few paragraphs.

One of the most critical metrics that has limited PMUT performance is the fractional bandwidth BW_f, and while it can be measured directly from a frequency response, the fractional bandwidth also has profound impacts on pulse-echo measurements. When driven by a sinusoidal pulse, it takes about $Q = 1/BW_f$ cycles for a PMUT to ring up to full amplitude, and another Q cycles to ring back down, meaning that a narrow fractional bandwidth results in a long pulse in the time domain. This can have a strong effect on the pulse-echo resolution; for the example shown in
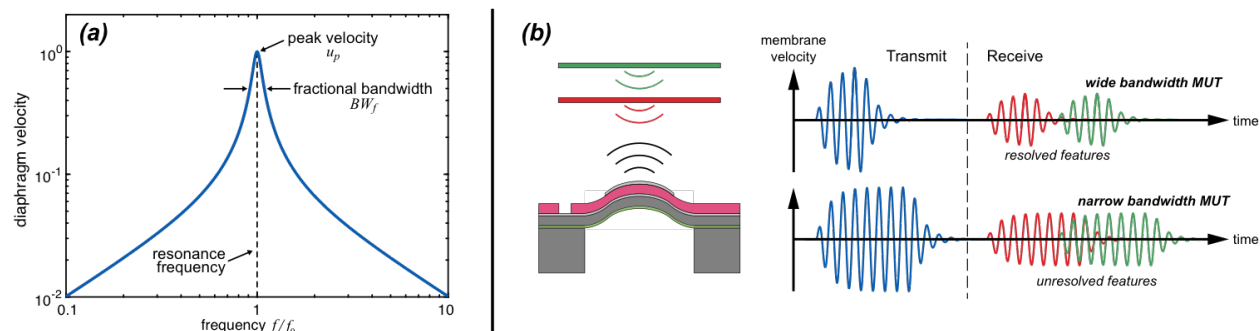
Figure 1.3: (a) Velocity frequency response and (b) pulse-echo measurement, which are common ways to characterize and operate PMUTs.

Figure 1.3(b), the wide bandwidth transducer (top waveform) is able to resolve the red and green objects, whereas the echoes are merged for the PMUT with a low BW_f (bottom waveform) and therefore the objects are not resolved. Similar effects also cause the bandwidth to limit the minimum measurement range. Furthermore, a wide fractional bandwidth indicates the presence of a strong energy loss mechanism, which can in fact be advantageous for ultrasound transducers. While many undesirable loss mechanisms may exist, such as thermoelastic damping and anchor losses, the transfer of energy from the PMUT diaphragm to the surrounding medium as acoustic power is also a loss mechanism and should in fact be strong for efficient mechanoacoustic transduction. Therefore, larger BW_f can indicate more efficient PMUTs, so long as it is for the right reasons.

In this realm, liquid-coupled CMUTs have shown remarkable success in achieving bandwidths in excess of 100% [21]. In contrast to PMUTs, which require thicker diaphragms to accommodate elastic layers and sufficient piezoelectric layers, CMUTs can be fabricated with extremely thin structures so that the mechanical impedance is significantly lower than that of the acoustic medium, thereby increasing the bandwidth. As such, researchers have had to devise alternate ways to boost the bandwidth of PMUTs. In two similar works, Lu *et al.* [22] and Wang *et al.* [23] achieved broad pressure bandwidths as high as 97% in liquid by designing long rectangular PMUTs with higher order vibration modes closely matched in frequency with the fundamental mode, with the two resonances merging when operated in liquid. This approach, however, does not enhance efficiency as it relies on acoustically inefficient higher vibration modes, and also requires large PMUT dimensions. Kusano *et al.* were able to boost the bandwidth by a factor of 8 by tuning the bias voltage of air-coupled PZT-based PMUTs with a similar long rectangular structure, but this effect is not observed in AlN and the introduction of a bias voltage diminishes the advantage of PMUTs. On the other hand, bandwidth increases have been reported in arrayed PMUT implementations. Hajati *et al.* found that by designing large arrays of PMUTs with 5 different sizes, and thus 5 different resonance frequencies, the resonances became merged when operated in liquid leading to a wide bandwidth of 55% [24]. This behavior has turned out to not require multiple PMUT sizes, however, as Akhbari *et al.* reported large arrays of equal-size transducers with a pressure bandwidth of over

150% that is caused by the increased damping created by the mutual coupling of PMUTs through the acoustic medium [25]. By leveraging arrays, however, these approaches require burdensome wafer footprints. Along these lines, one of the major contributions of this dissertation research is the development of a novel PMUT architecture that is capable of extending the bandwidth of standalone PMUTs due to acoustical effects that have not been previously studied or utilized.

Aside from bandwidth, another fundamental performance metric is the peak velocity u_p, the importance of which is derived from its intrinsic relation to transmission-mode pressure output p_{out} as the two quantities are proportional, i.e., $u_p \propto p_{out}$. Ultrasound-based medical therapies typically require a threshold acoustic intensity, commanding high transducer velocities for their generation. In imaging and pulse-echo operations, higher pressure output leads to improved signal-to-noise ratio (SNR) in the received waveform, thereby improving image quality and increasing the maximum achievable working distance [26]. As such, several works have focused on boosting the displacement and velocity of PMUT structures. Through the use of a spherical-shape diaphragm that is fabricated by means of an isotropic wet etch [27] or by stress engineering [28], Akhbari *et al.* were able to show a profound $50\times$ increase in static displacement compared to their flat PMUT counterparts. Leveraging the extensive work in bimorph cantilever MEMS systems, PMUTs with multiple active piezoelectric layers have shown nearly a factor of 2 increase in displacement [29] compared to those with a unimorph construction. Conversely, a sloped PMUT diaphragm was used by Luo *et al.* to reduce anchor losses and increase displacement at resonance by a factor of 3, although at the cost of a decreased bandwidth [30].

As another approach to increasing pressure output, array implementations have also been used. An array of bimorph PMUTs capable of generating suitable acoustic intensities for medical operations such as LIPUS at low driving voltages was reported by Akbhari *et al.* [31], however the footprint of this array is large and limits its usage to percutaneous treatments. A high packing density of $1261 \, \mathrm{transducers/mm^2}$ was reported by Lu *et al.* to generate acoustic output of about $2 \, \mathrm{kPa/V}$ that is impressive when considering the small array footprint of less than $1.2 \, \mathrm{mm^2}$ [32], but which is still substantially lower than the level required for medical therapies. These numbers can be improved by driving PMUTs within an array with variable time delays to focus the acoustic energy, resulting in a measured a pressure increase of $1.6\times$ [33] and $3\times$ [34], however further advancements are still required. Inspired by these works, within this dissertation is the introduction of PMUT arrays with novel geometries that yield exceptional acoustical outputs and more effective acoustic focusing.

On the other hand, the amplitude of the echo signals in pulse-echo operation are not only affected by the performance of the transducer in transmission, but also in reception; a more accurate figure of merit for pulse-echo sensitivity is therefore the electromechanical coupling factor k^2 [35], which has a theoretical maximum value of 1, and is a function of the piezoelectric material properties and boundary conditions. Extensive efforts to improve the electromechanical coupling have accordingly spanned both the structural design of PMUTs along with piezoelectric material innovations. The dual-electrode bimorph architecture reported by Akhbari *et al.* increases the amount

of active material within a PMUT by a factor of 4 to increase the electromechanical coupling by the same amount [25]. Lu *et al.* have cleverly utilized a series transduction scheme on a PMUT with two electrodes in order to reduce the capacitance and increase k^2 by $2\times$ [36]. Moving away from planar diaphragms, Hajati *et al.* designed a dome-shaped PMUT based on PZT that exhibits remarkably high $k^2 \approx 45\%$ due to the vertical contributions of the piezoelectrically-induced stress [24] and approaches the material limit of PZT $k^2 = 58\%$[37]. By comparing PMUTs composed of AlN and PZT, Lu *et al.* found the latter to exhibit superior electromechanical transduction with $k^2 = 12.5\%$ [38]. This is corroborated by theoretical findings that k^2 in PZT is about 50% higher than AlN [33], however AlN is still the more common PMUT material choice due to the existence of high-quality and CMOS-compatible film deposition techniques that are fairly mature due to the commercial usage of AlN in RF filters [11]. Recently, PMUTs based on scandium-doped AlN (ScAlN) have been developed with superior electromechanical coupling to PZT while maintaining the process compatibility offered by AlN [35]. In most cases, material innovations can be combined with design improvements to further enhance performance.

In summary, while PMUTs offer important advantages over their capacitive counterparts, various aspects of their performance has prevented their widespread adoption and commercial viability. Examining the methods of characterization and operation of PMUTs elucidates a few of the most prominent bottlenecks, namely the fractional bandwidth, peak velocity, and electromechanical transduction efficiency. To this end, research endeavors focused on alleviating the drawbacks exhibited by more traditional PMUTs have been undertaken, as summarized here. Despite substantial successes, innovations are still required to continue improving PMUT performance to the level necessitated by commercial applications.

1.3   Dissertation Contributions and Organization

This dissertation research is focused on improving the performance of PMUTs through design innovations, and using these advancements to develop PMUT-based systems for existing applications and those that expand the application space of ultrasound. The major contributions are depicted in Figure 1.4, and are described as follows.

The ring-shaped PMUT, schematically illustrated in Figure 1.4(a), is introduced as a high-performance PMUT architecture in Chapter 2. The overall structure, layout geometry, and operation are first described, before discussing fabrication and characterization. Ring-shaped PMUTs operated in air are shown to provide benefits in pressure output and directivity as compared to the typical circular PMUT design, both of which stem from the ability to separately tune aperture size and resonance frequency that is unique to the ring-shaped architecture. Furthermore, any system based on the ring-shaped PMUT requires optimized performance with well-known characteristics, which merits an in-depth look at the dynamics of the transducer. To this end, Chapter

3 presents an equivalent circuit model for ring-shaped PMUTs, which is able to concisely model all the relevant physics in the electrical, mechanical, and acoustical domains, and can be used not only to predict and optimize performance, but also to help guide the design of interface circuitry or compare PMUT designs. The equivalent circuit model is derived entirely from Hamilton's Principle and energy-based arguments with an emphasis on the acoustic impedance, which proves to play a strong role in device performance, and is validated extensively by way of finite element simulations. In chapter 4, the broadband performance of ring-shaped PMUTs in liquid-coupled operation is reported. Depending on the aperture size and acoustic medium, the frequency response of ring-shaped PMUTs can show multiple resonance peaks resulting in either narrow or wide bandwidths, as shown in Figure 1.4(b). In conjunction with displacement and pressure measurements, the acoustic impedance derived in Chapter 3 is used to explain that this behavior is caused by an acoustically induced resonance, which has not been previously observed or utilized in MUT design.

Moving away from standalone devices, Chapter 5 presents the development of a single-chip ultrasonic flow sensor with differential readout, which leverages arrays of the dual-electrode bimorph (DEB) high-performance PMUT design developed previously in our lab [25]. The sensor concept and operating principle are depicted in Figure 1.4(c): using transmitter PMUTs that generate highly directional acoustic output, lateral flow carries the acoustic energy downstream, altering the pressure amplitude that is measured by the spatially separated receiver PMUTs. This sensor achieves high sensitivity while promising simple implementation so that, combined with the small size and low cost offered by MEMS systems, it could provide a means to make ultrasonic flow sensing more ubiquitous. In Chapter 6, the DEB design utilized in Chapter 5 is paired with the ring-shaped PMUT presented in Chapters 2 through 4 to propose concentric arrays of ring-shaped bimorph PMUTs with high acoustic power output. In order to guide the array design, which is illustrated in Figure 1.4(d), Chapter 6 focuses on developing the equivalent circuit network model shown in Figure 1.4(e) by building upon the equivalent circle model for standalone PMUTs presented in Chapter 3 and accounting for the PMUT-to-PMUT coupling that occurs through the acoustic medium. Using this model, simplified design equations are determined that reveal surprising trends and lead to an approach for maximizing the acoustic power output from concentric arrays that differs fundamentally from comparable works on CMUTs. In Chapter 7, concentric arrays of ring-shaped PMUTs are fabricated and experimentally characterized in order to evaluate their ability to generate sufficient acoustic output for high-intensity applications. While the arrays show an impressive acoustic output when driven under standard conditions, the use of phased array focusing is also used to boost the acoustic intensity in specific regions as showed by the pressure field measurements in Figure 1.4(f). As such, well-designed concentric ring-shaped PMUT arrays show promise for a host of ultrasound-based medical operations. Finally, concluding remarks are offered in Chapter 8.
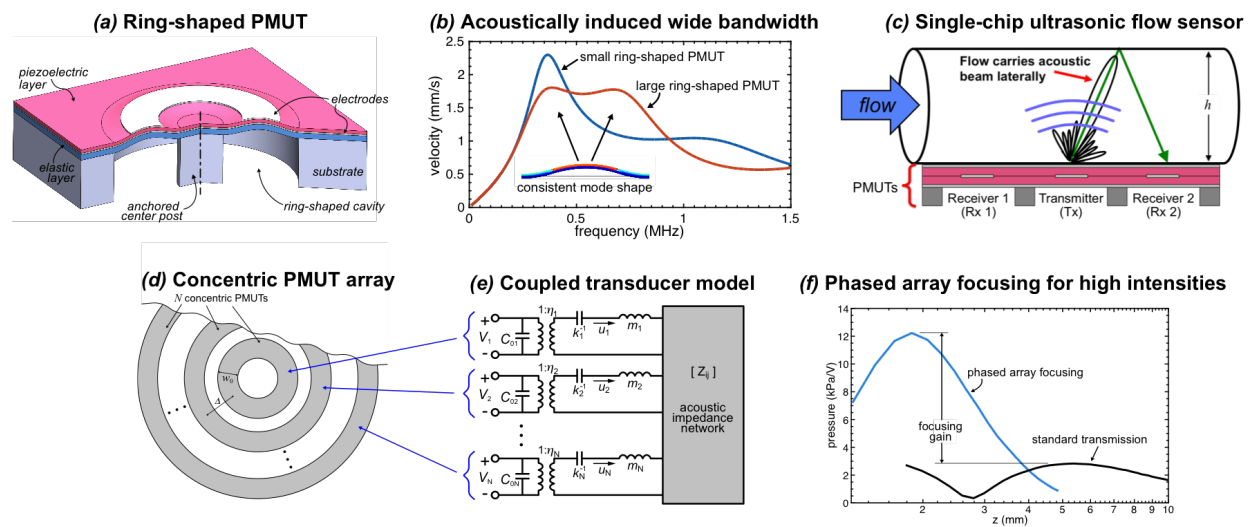
Figure 1.4: Illustrative summary of key dissertation contributions. (a) Structure of the ring-shaped PMUT; (b) frequency response of ring-shaped PMUTs with small and large apertures operated in liquid; (c) operating principle of the single-chip ultrasonic flow sensor proposed in Chapter 5; (d) layout of a concentric array of ring-shaped PMUTs; (e) the equivalent circuit network model presented in Chapter 6 for concentric PMUT arrays; (f) acoustic pressure versus distance from a PMUT array with a standard drive scheme and with phased array focusing.

Chapter 2

Ring-shaped PMUTs

In this chapter, the ring-shaped PMUT will be introduced as a novel PMUT architecture and its performance will be evaluated both experimentally and with finite element analysis (FEA). Beginning with a description of the design in comparison with conventional PMUTs, we will subsequently present an overview of the fabrication process and resulting devices, along with baseline testing and intuitive explanations for some unique observed behaviors with notable performance implications. Furthermore, by comparing prototype designs of circular and ring-shaped PMUTs having the same film stacks and 1.5 MHz resonance frequencies, ring-shaped PMUTs are shown to be capable of generating $11.8\times$ the pressure and with over $9\times$ the directivity of their circular counterpart.

2.1 Device Architecture

A comparison between conventional (circular) and ring-shaped PMUTs is presented in Figure 2.1 with cross-section schematic drawings of the transducers as they deflect during flexural vibration. The film stack forming the transducer diaphragm is consistent between the two designs, insofar as an active piezoelectric layer is sandwiched by metal electrode layers and lies on top of an inactive structural layer, which can be any material. As shown in the actuation detail, electromechanical transduction in each design also occurs in the same manner, which is consistent with the vast majority of PMUTs: an applied voltage between the two electrodes generates an in-plane piezoelectric stress via the 31-mode converse piezoelectric effect [39], which in turn generates a bending moment due to the offset between the active piezoelectric layer and the neutral plane of the structure, and causes an axisymmetric out-of-plane deflection of the diaphragm.

In contrast, the main difference between the two is the rigid center post in the ring-shaped design which, as the name suggests, creates an annular diaphragm where the center is mechanically anchored. Due to this difference in geometry, while the circular PMUT is defined by its radius a,
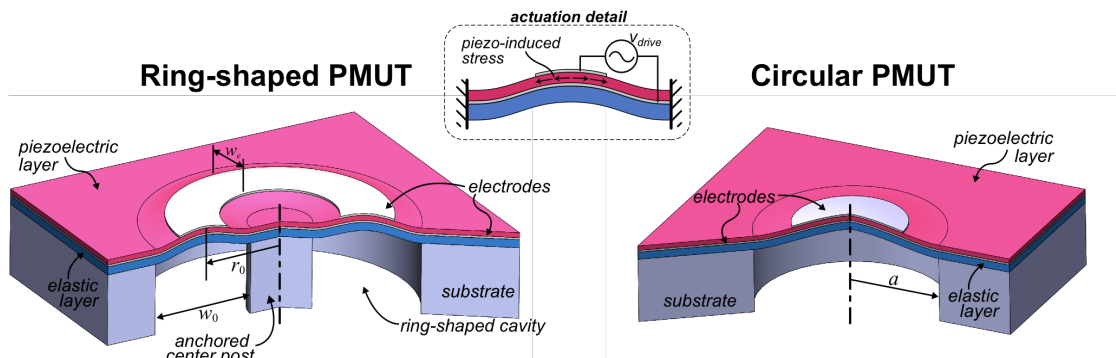
Figure 2.1: Comparison of ring-shaped and conventional (circular) PMUTs. As shown in the actuation detail, electromechanical transduction occurs due to the 31-mode piezoelectric effect.

the ring-shaped PMUT is characterized by both its width w_0 and mean radius r_0 such that the two clamped boundaries lie at $r = r_0 \pm w_0/2$. By nature of the new diaphragm geometry, the top electrode also takes on an annular shape with width w_e. As reference, it was found throughout this study that ring-shaped and circular PMUTs with the same film stack exhibit equal resonance frequencies so long as $w_0 \approx 1.48a$; as will be shown in subsequent sections, resonance frequency is independent of r_0.

2.2 Fabrication

One practical benefit of the ring-shaped PMUT is that it does not require any additional fabrication complexity in comparison with circular PMUTs, thus the process used here, shown as a flow diagram in Figure 2.2, closely mirrors the CMOS-compatible process developed previously in our lab [40].

In reference to Figure 2.2, the fabrication begins with (a) the deposition of the aluminum nitride (AlN) and molybdenum (Mo) film stack that will later make up the transducer diaphragm on a silicon wafer. Here, Mo is used as the electrode layers and AlN is not only used as the active piezoelectric layer, but also for the inactive structural layer for several reasons: (1) the entire film stack can be deposited without breaking vacuum and therefore promotes high-quality film growth; (2) the piezoelectric properties of the active AlN layer are highly dependent on its c-axis orientation, which can be diminished when depositing on top of a Mo layer if there is no AlN seed layer beneath; and (3) due to its inertness in SF_6-based etch chemistries, AlN is an excellent stop layer in the final release etch step and therefore helps reduce across-wafer variations and improve yield. The thickness of each layer in the film stack deposited in (a) are, starting from the silicon surface, AlN (h_B=1000 nm)/Mo (130 nm)/AlN (h_T=800 nm)/Mo (130 nm), where $h_T < h_B$ to ensure that the neutral axis of the diaphragm is not inside of the active layer, preventing
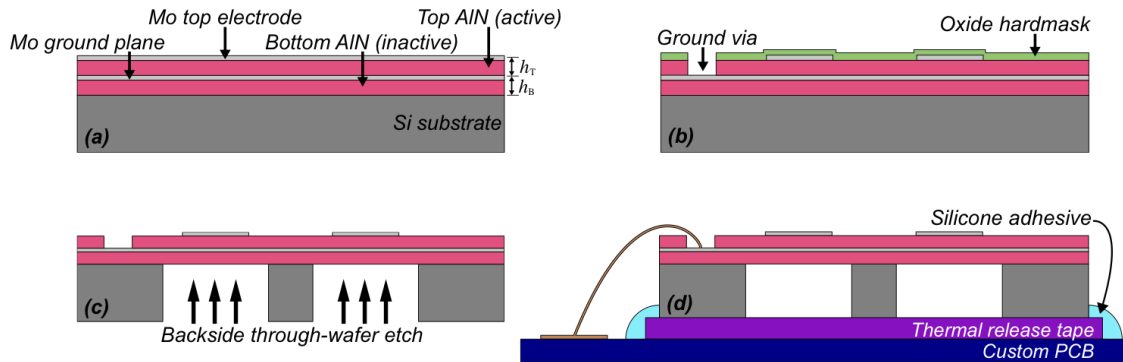
Figure 2.2: Fabrication process for the ring-shaped PMUT: (a) sputter deposition of film stack; (b) top electrode patterning, SiO$_2$ hardmask deposition, and via etching; (c) backside through-wafer DRIE to release diaphragm; (d) mounting and wirebonding to custom PCB for testing.

performance degradation [41].

In (b), the top Mo electrode is patterned by a SF$_6$ plasma etch, then the ground vias are patterned by first depositing a hard mask of 500 nm of PECVD SiO$_2$, followed by a two-step etch of AlN using first a Chlorine-based plasma and a subsequent wet etch in MF-319 photoresist developer. The top electrode is designed to have a 55% areal diaphragm coverage and the same mean radius r_0 as the PMUT (i.e., is centered on the released diaphragm) as simulations indicate that this results in good coupling to the fundamental vibration mode of the diaphragm. The diaphragms are then released (c) with a backside through-wafer DRIE stopping on the bottom AlN layer. This etch is a two-step process wherein about 70% of the wafer thickness is etched with a standard DRIE etch and the remainder is etched by applying low-frequency power (380 kHz, rather than 13.80 MHz used in the previous step) to bias the platen. By applying the platen bias with low-frequency power, ions in the etch chamber have sufficient time to react to the electric field and therefore charge build-up at the dielectric (AlN) surface is prevented, thereby eliminating footing effects at the silicon-AlN interface [42]. Finally, (d) the device chips are diced, mounted on a custom PCB using thermal release tape and silicone adhesive to ensure a full seal, then wirebonded to the PCB for testing.

Figure 2.3 shows fabrication results of released ring-shaped PMUTs (after completion of step (c) in Figure 2.2). The top-view optical micrograph in Figure 2.3(a) has an artificial dashed line to show the boundary of the etched cavity, with ground vias fully exposed and without any residual AlN or damage to the Mo ground plane. Figure 2.3(b) shows a cross-section SEM of a ring-shaped PMUT that broke while mounting for imaging. During the DRIE backside release process, the sidewalls show a slight under-cut resulting in larger fabricated diaphragm widths than the designed values. This effect is most pronounced along the center post, and was found to result in a 20-30 μm discrepancy between the designed and actual width by using confocal microscopy (LEXT OLS3000, Olympus) for sidewall profile measurements. For this reason the designed and
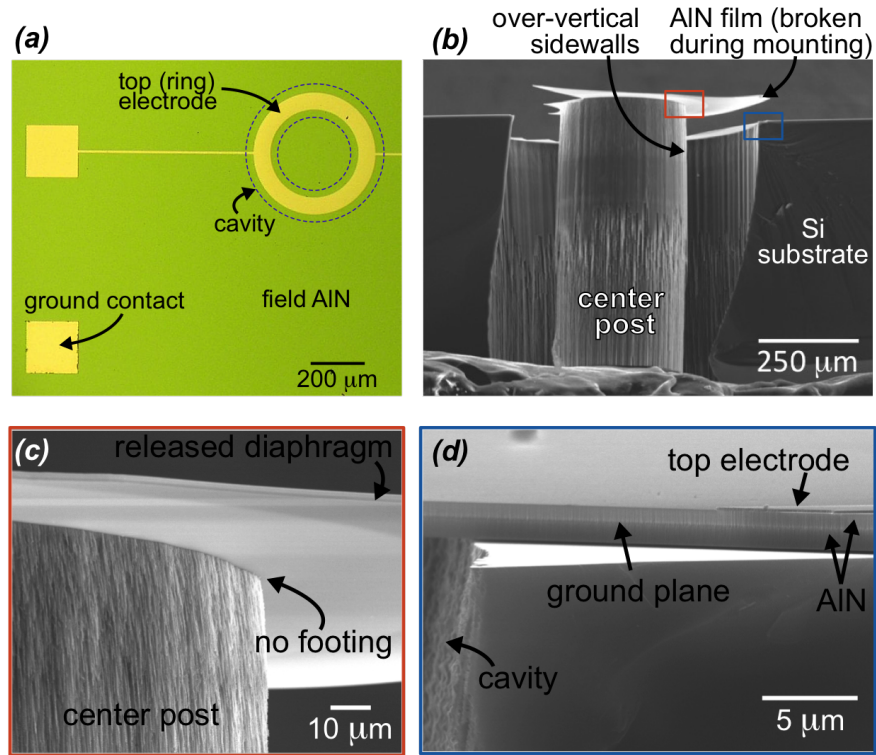
Figure 2.3: (a) Optical micrograph and (b)-(d) cross-section SEM images of a ring-shaped PMUT before mounting, showing uniform, high-quality films and well-defined diaphragm boundaries.
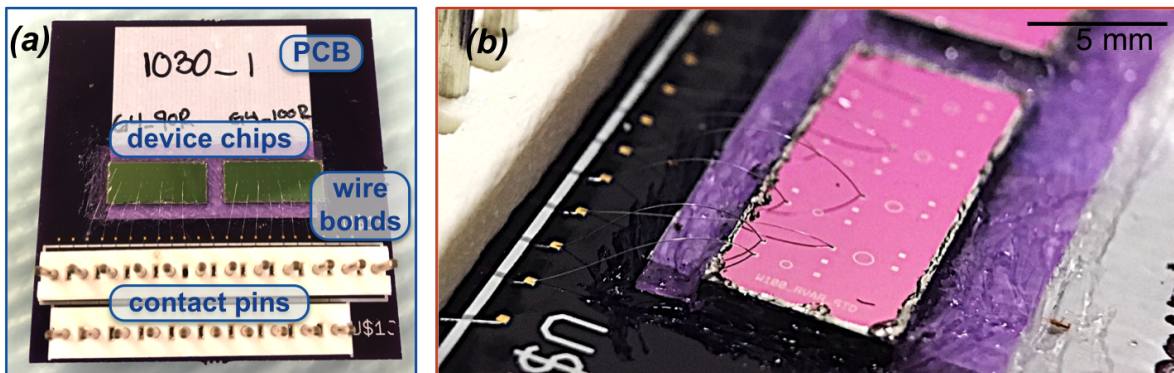
Figure 2.4: Fabricated ring-shaped PMUTs wirebonded and mounted on PCB for testing. Each device chip has 8 individual PMUTs with the same width w_0 and different values of r_0.

actual widths will henceforth be referred to using the variables w_{des} and w_{act}, respectively. This effect would be magnified by footing effects, which are successfully eliminated by using the low-frequency platen bias as shown in Figure 2.3(c). Furthermore, a thin Mo ground plane sandwiched between two AlN layers and a patterned top Mo electrode layer can be observed in Figure 2.3(d), where all films show high uniformity. The full-width half-maximum (FWHM) of the AlN films was measured using X-ray diffraction (XRD) (D5000, Siemens) as $1.3°$, ensuring highly oriented crystal grains and good piezoelectric properties. Optical images of a final device chip mounted and wirebonded to a PCB for testing are provided in Figure 2.4.

2.3   Device Characterization

In order to characterize the fabricated ring-shaped PMUTs, their dynamic performance was measured with a laser Doppler vibrometer (LDV, OFV-5000, Polytec Inc.) in air. Figure 2.5 displays the results of six typical frequency responses for ring-shaped PMUTs with width w_{des}=70 (thick lines) and w_{des}=90 μm (thin lines), and three different mean radii r_0 from 200 to 300 μm for each width. As expected, all devices show a main resonance peak with a fairly narrow 3 dB fractional bandwidth BW_f between $1-2\%$, where $BW_f = \Delta f_{3dB}/f_0$, f_0 is the resonance frequency, and Δf_{3dB} is the 3 dB displacement bandwidth. While high frequency spurious resonances are observed and are likely due to fabrication imperfections, the fundamental resonance frequencies f_0 for w_{des}=70 and 90 μm varied from 2.04-2.10 MHz and 1.42-1.45 MHz respectively, both of which represent a less than 3% variation as r_0 increases by $1.5\times$.

As there is only one possible geometry for a given film stack and operational frequency with conventional PMUTs, this insensitivity of resonance frequency to r_0 allows for an extra degree of design freedom in ring-shaped PMUTs. While a more rigorous and analytical explanation for this behavior will be covered in the next chapter, an intuitive argument can be made by examining the equation for resonance frequency:

$$f_0 = \frac{1}{2\pi}\sqrt{\frac{k}{m}}, \tag{2.1}$$

where k and m are the modal mass and stiffness of the structure. It is intuitive that mass is proportional to surface area A, and we can therefore say that $m \propto r_0$ after considering that $A = 2\pi r_0 w_0$, however, the relationship between k and r_0 is less straightforward. A first-order approximation can be found for the case of $r_0 \gg w_0$ by conceptually "unwrapping" the ring-shaped PMUT into a long rectangular strip with length $L = 2\pi r_0$ and width w_0, anchored along the two long boundaries and free along the two short boundaries. By definition $k = F/x$, where x is the static deflection, and it follows that

$$k = \frac{F}{x} = \frac{PA}{x} = \frac{PLw_0}{x} \tag{2.2}$$
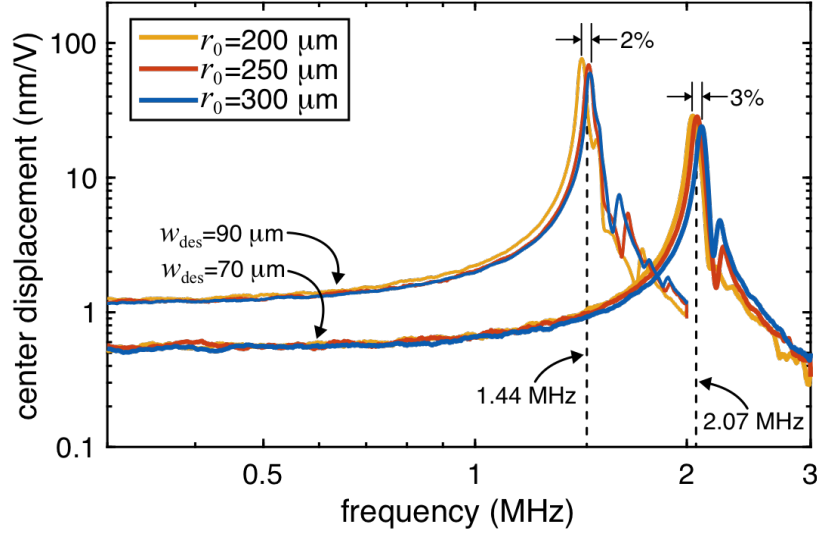
Figure 2.5: Measured displacement frequency responses of six ring-shaped PMUTs in air, showing minimal dependence of resonance frequency on r_0 and strong dependence of resonance frequency on w_0.

where P is a uniform pressure applied on the diaphragm. Since the static deflection of a rectangular diaphragm with these boundary conditions does not depend on the length of the diaphragm, the only variable in Eq. 2.2 that depends on r_0 is L, so it can be approximated that $k \propto r_0$. Therefore, r_0 cancels out of Eq. 2.1, and f_0 should show no dependency on the mean radius.

In order to ensure that the devices operate in the assumed mode, the vibration mode shape was additionally measured with a Digital Holographic Microscope (DHM, DHM-R1000, Lyncee Tec) by recording the vibration amplitude of the entire surface at the PMUT plane around the resonance frequency of the transducer. The results of such measurements taken along a diametrical line of the device at 1.4 MHz for a PMUT with w_{des}=90 μm and r_0=300 μm are displayed in Figure 2.6. In (a), the normalized vibration profile of the entire ring-shaped PMUT is shown, where there is negligible vibration occurring within the anchored center post region, the maximum deflection occurs at $r = \pm r_0$, and a gradual curved profile that is expected of flexural vibrations is apparent in the regions where the diaphragm is released. A magnified view of the right-hand peak in (a) is shown in (b), alongside comparisons with a FEA simulation carried out in Comsol Multiphysics, the setup of which is covered more thoroughly in Chapter 3.4.1, and an analytical approximation which is given by

$$\phi(r) = (1 - \bar{r}^2)^2, \tag{2.3}$$

where $\bar{r} = (r - r_0)/(w_{\text{act}}/2)$ is a normalized radial coordinate that varies from -1 to 1 at the inner and outer clamped boundaries, respectively. As will be explained further in Chapter 3, this approximation is motivated by the static deflection with a uniform pressure load applied to a clamped-free-clamped-free rectangular diaphragm, which is similar to a conceptually "unwrapped" ring-shaped

PMUT. All three methods show excellent agreement, and an actual width of w_{act}=120 μm is observed, which is consistent with the aforementioned fabrication variations.

In order to further validate the FEA model and confirm its ability to correctly predict device performance, frequency response simulations were also compared with LDV measurements. Figure 2.7 shows one such comparison for a ring-shaped PMUT with w_{des}=90 μm, w_{act}=120 μm, and r_0=225 μm, where an excellent agreement between model and experiment is displayed by a close match between measured and simulated values for both (1) low-frequency displacement (1.10 and 1.14 nm, respectively), and (2) resonance frequencies (1.45 and 1.46 MHz, respectively).

2.3.1   Simulated Acoustic Performance

To compare the acoustic performance of circular and ring-shaped PMUTs, FEA simulations of two prototype devices (ring: w_0=115 μm, r_0=225 μm, 55% electrode coverage, and circle: a=77.25 μm, 70% electrode coverage) designed for 1.5 MHz operation with 800/1000 nm thick AlN film stacks were performed. Figure 2.8(a) and (b) respectively show the mean displacement and far-field pressure at a distance of 1.4 mm for the prototype transducers. Despite having nearly equal maximum displacements, the ring-shaped PMUT outputs a peak pressure of 201 Pa, which is more than 7.7× greater than the 23 Pa displayed by its circular counterpart. The ring-shaped PMUT is able to output such high acoustic pressures because $P \propto V_v$, where $V_v = v_{\text{mean}}A$ is the volume velocity and v_{mean} is the mean diaphragm velocity, and the radiating area of a ring-shaped PMUT may be made much larger than that of the circular PMUT by choice of r_0. Indeed, as shown in Figure 2.8(c), the pressure generated by the ring-shaped PMUT shows a strong dependence on r_0, and reaches a value of 272 Pa when r_0=325 μm, which is over 11.8× that of the circular PMUT. This simulated 1080% increase in SPL represents the largest reported improvement resulting from a design change, and while the output pressure of circular PMUTs may be increased by creating multi-PMUT arrays with a similar footprint to that of the ring-shaped PMUT, previous research has shown that pressure output does not simply scale with the number of PMUTs (e.g., an array of 10 circular PMUTs will be less than 10 times the output of a single PMUT) and is further complicated by frequency-matching issues and inter-PMUT coupling causing array modes [43],[44]. At very large values of r_0 the pressure begins to decrease due to increased loading from the acoustic medium and the effects of sidelobes. Figure 2.8(d) shows the normalized far-field pressure beam pattern from the ring and circle prototypes. Owing to its larger acoustic aperture, the ring has a more directional acoustic output, displaying a directivity factor, which is the ratio of peak to average acoustic intensity, of 38 compared to 4 for the circle and thereby improving efficiency.
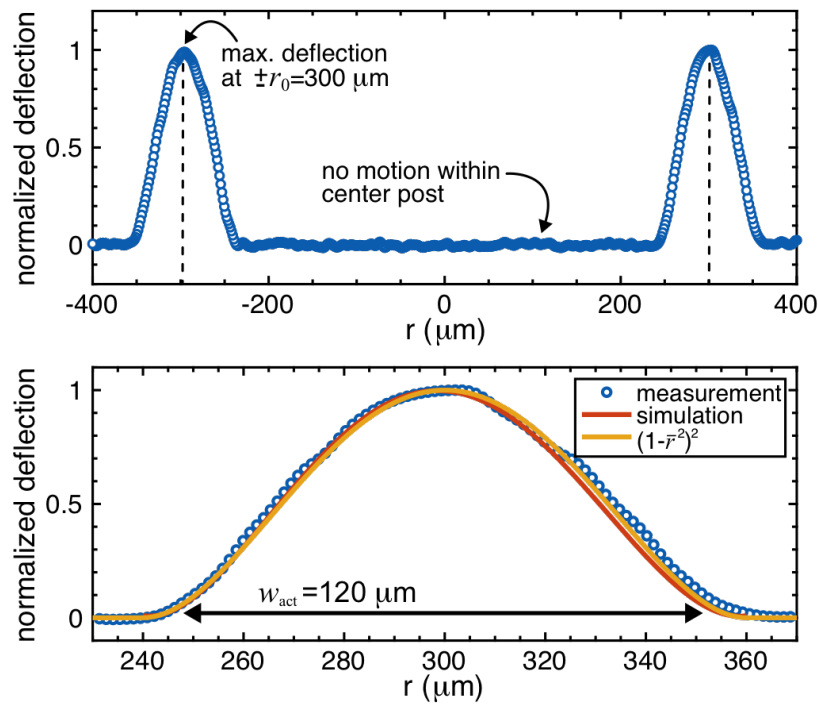
Figure 2.6: (a) Vibration displacement profile measured with DHM near resonance, showing no motion within the region defined by the center post and maximum deflection at $\pm r_0$; (b) magnified view of the right-hand peak from (a), along with simulated and approximated mode shapes. The three methods show strong agreement and indicate an actual width w_{act}=120 μm.
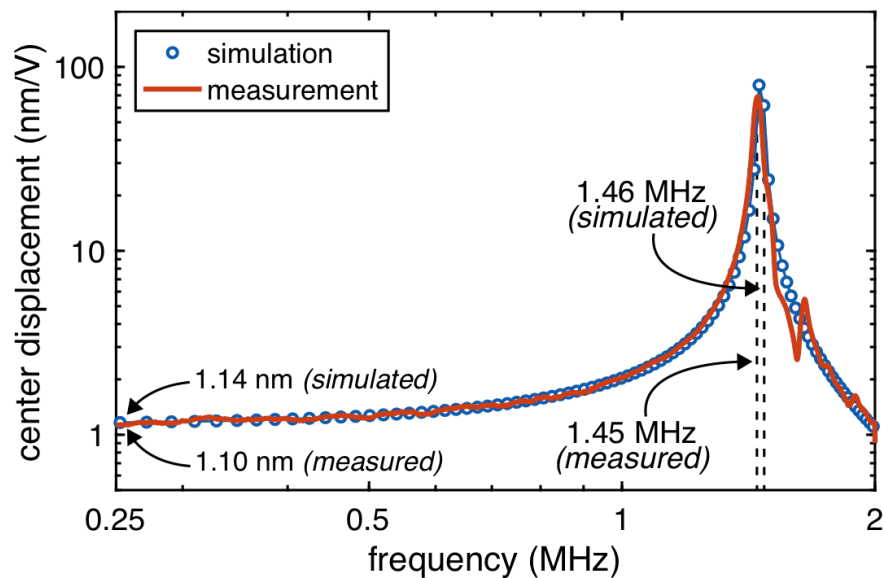
Figure 2.7: Comparison of simulated and measured center displacement of a ring-shaped PMUT with w_{des}=90 μm, w_{act}=120 μm, and r_0=225 μm, showing good agreement.
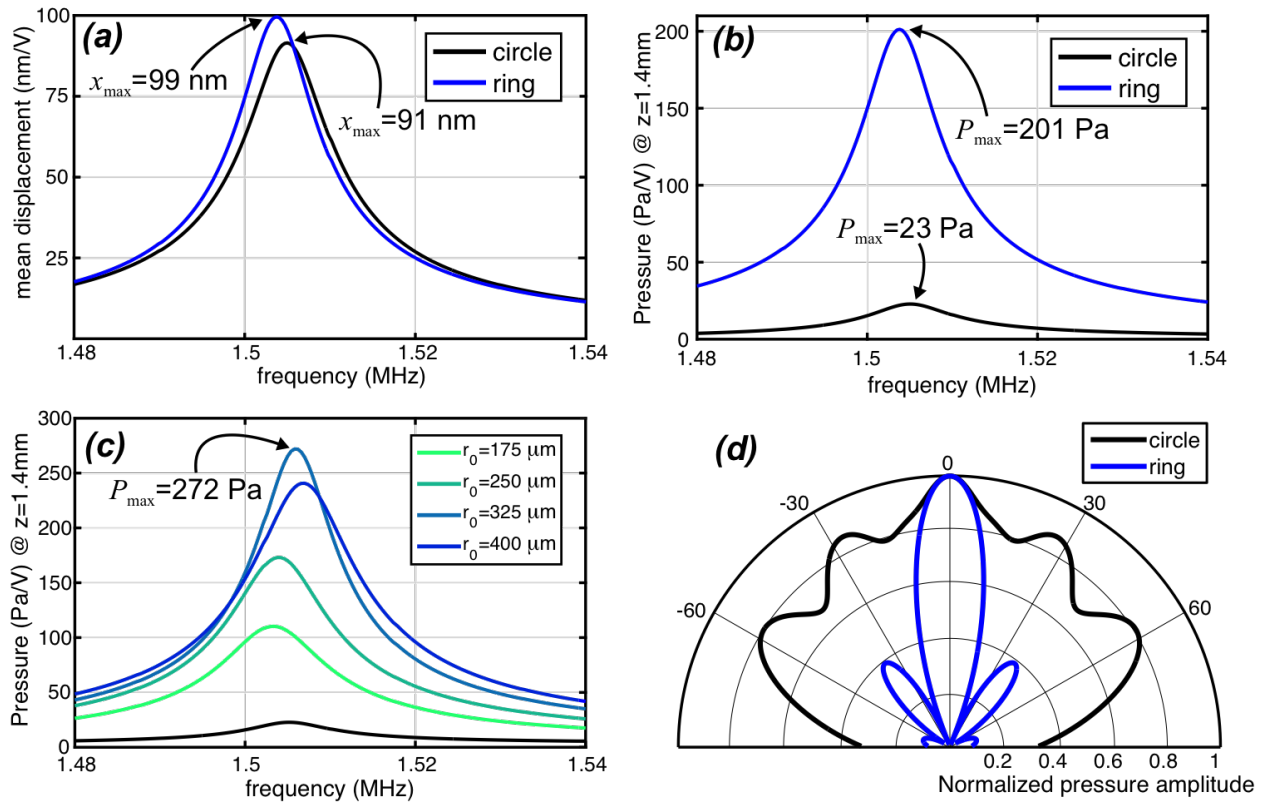
Figure 2.8: Simulated displacement (a) and far-field pressure (b) frequency responses near resonance of the prototype transducers; (c) far-field pressure for ring-shaped PMUTs with w_0=115 μm and various r_0; (d) normalized pressure beam patterns of prototype transducers.

2.4 Summary

Ring-shaped PMUTs have been introduced, fabricated, and characterized both experimentally and through FEA simulations. An insensitivity of the resonance frequency on the mean radius has been observed, allowing ring-shaped PMUTs an extra degree of design freedom compared to circular PMUTs, as the layout geometry is no longer constrained by the resonance frequency. Owing to this fact, ring-shaped PMUTs can be designed with a larger volume velocity than circular PMUTs, thereby increasing their pressure output. In fact, by comparing 1.5 MHz devices made of the same film stack, ring-shaped PMUTs show an estimated 1080% increase in SPL and 830% increase in directivity factor over circular PMUTs. These factors indicate that ring-shaped PMUTs may be ideal for forward-looking applications that require large acoustic pressures, such as rangefinding, fingerprint scanning, and therapeutics.

Chapter 3

Equivalent Circuit Model of Standalone Ring-shaped PMUTs

In this chapter, we will build upon the intuitive arguments presented previously and analytically derive an equivalent circuit model for ring-shaped PMUTs. While several benefits associated with the annular geometry including high output pressure and fill-factor, long natural focal depths, and facilitated beamforming have been suggested, the behavior of the structure must be analyzed and thoroughly explored before high-quality transducers can be designed.

3.1   Background and Introduction

In efforts to boost PMUT performance in recent years, the need for simplified analytical models has become obvious: while design changes have shown significant advancements (e.g., [27], [24], [45]), device optimization within any given design often merits an in-depth analysis. Some works have focused on using finite element analysis (FEA) to evaluate the dependency of performance on design parameters (e.g., [46], [47]). In order to fully understand the underlying physics and characteristics of new PMUT structures and streamline their optimization, however, it is beneficial to have a tractable analysis that also avoids prohibitive simulation times. In this aim, researchers have focused their efforts on electromechanical analysis and developing equivalent circuit models; while both are helpful, the latter is ideal due to its ability to encompass all relevant physics in the electrical, mechanical, and acoustical domains [48].

As the most common device architecture, the planar circular PMUT with a single piezoelectric layer has garnered the majority of attention in this realm. Muralt *et al.* reported an energy-based analysis that utilizes the first mode shape predicted by plate vibration theory [16], which has subsequently laid the framework for other works that have simplified the analysis using approximate

mode shapes (e.g., [49], [36]). In a comprehensive work on planar circular PMUT modeling, Smyth *et al.* derived and validated a full equivalent circuit [50] from a plate-theory-based Green's function deflection model [51] that can consider all axisymmetric vibration modes and is valid for any number of axisymmetric electrodes. Employing a similar Green's function approach, Sammoura *et al.* used analytical analysis [52] to define an equivalent circuit that accounted for and demonstrated the effects of residual stress [53]. Comparable modeling has also been performed for rectangular PMUTs, such as the 1D analysis Cho *et al.* employed to show similar residual stress effects [54] and the 2D analysis Choi *et al.* used to derive an equivalent electromechanical circuit [55] by omitting considerations of acoustic effects. As design innovations are devised, analogous efforts regarding other PMUT architectures have also been reported. A curved aluminum nitride (AlN) PMUT developed by Akhbari *et al.* [27], [28] was shown to have superior electromechanical coupling compared to its planar counterpart using an analytical equivalent circuit [56], [57]. Shelton *et al.* modeled a backing tube as an acoustic transmission line [49] that was appended to their previously developed PMUT equivalent circuit [58] and provided a substantial amplification in pressure that matched well with FEA simulations. The high efficiency and displacement sensitivity of the dual-electrode bimorph PMUT developed by Akhbari *et al.* [25], [31] were shown collectively between the modeling efforts on two-port [59] and bimorph [20] PMUTs.

In contrast to the aforementioned works, we herein report the derivation of an equivalent circuit model for ring-shaped PMUTs which can be used to greatly improve understanding of the device dynamics and evaluate the ring-shaped design as a high-performance PMUT architecture. In order to facilitate the development of this intuitive understanding, we aim for the equivalent circuit developed here to provide a tractable framework that is easily implemented for future researchers. We therefore choose a relatively simple method of modeling based entirely on energy-based principles and assumed mode shapes that is accurate around and below the first resonance of the device, as is typical in practice for most PMUTs. This approach is not restricted to PMUT analysis and is in fact easily adapted to obtaining simplified models for many piezoelectric devices. We begin with an overview of the ring-shaped PMUT concept and structure, and present its fundamental governing equations and a basic theoretical analysis of its dynamics. This is used periodically as validation throughout the remainder of the work and substantiates the assumed mode shape, which is in turn used to extract the lumped parameters for the equivalent circuit. Special care is taken to evaluate and describe the acoustic impedance, as this has not been reported with sufficient accuracy for modeling in the literature, and it has a significant impact on overall performance. Finally, the behavior is explored and the equivalent circuit is validated extensively with drive-mode FEA simulations for both air- and liquid-coupled devices with a wide range of dimensions.

3.2 Device Concept and Governing Equations

3.2.1 Overview of the ring-shaped PMUT

For clarity, a brief re-examination of the ring-shaped PMUT geometry will be provided before covering the mathematical problem formulation. Figure 3.1 presents a conceptual cross-sectional diagram of the ring-shaped PMUT, which is composed of an annular diaphragm anchored by a rigid center post and bulk substrate. The diaphragm is most conveniently characterized by its mean radius r_0 and width w_0; the layout geometry is defined by two clamped boundaries at inner and outer radii of $a = r_0 - w_0/2$ and $b = r_0 + w_0/2$, respectively, and the total vibrating area is $A_v = 2\pi r_0 w_0$. In the unimorph configuration shown, an elastic layer lies below the piezoelectric transduction layer, which is sandwiched between two electrodes. The bottom electrode fully covers the diaphragm while the top ring-shaped electrode has width w_e, and as is explained later, is centered on the diaphragm so that the electrode may also be characterized by its inner and outer boundaries at $a_e = r_0 - w_e/2$ and $b_e = r_0 + w_e/2$, respectively. As is labeled in the cross-section detail of Figure 3.1, the neutral plane of the diaphragm is at a distance z_N from the bottom [37]:

$$z_N = \frac{1}{2}\frac{\sum_i Y''_{0i}(z_i^2 - z_{i-1}^2)}{\sum_i Y''_{0i}h_i},$$ (3.1)

where $Y''_{0i} = Y_{0i}/(1 - \nu_i^2)$, Y_{0i} and ν_i are the Young's modulus and Poisson's ratio of the i-th layer, respectively, and h_i and z_i are the thickness and distance from the top of the i-th layer to the bottom of the diaphragm, respectively. For a homogeneous diaphragm, (3.1) simplifies so that the neutral axis is simply located at $z_N = h_{tot}/2$, however for a film stack with layers of different materials the full expression must be evaluated.

As an electromechanical transducer, the interrelationship between stress vector T, strain vector S, electric field vector E, and electrical displacement vector D is governed by the constitutive piezoelectric relations, which can be written in the strain-charge form as

$$\begin{aligned} S &= s^E T + d^t E \\ D &= dT + \varepsilon^T E, \end{aligned}$$ (3.2)

or in the stress-charge form as

$$\begin{aligned} T &= c^E S - e^t E \\ D &= eS + \varepsilon^S E, \end{aligned}$$ (3.3)

where superscript t denotes matrix transpose; superscript T, S, and E denote properties measured at constant stress, constant strain, and constant electric field respectively; c^E and s^E respectively are 6×6 stiffness and compliance matrices and related by $c^E = (s^E)^{-1}$; d and e are 3×6 piezoelectric coefficient matrices related by $e = c^E d$; and ε is a 3×3 dielectric permittivity matrix where the
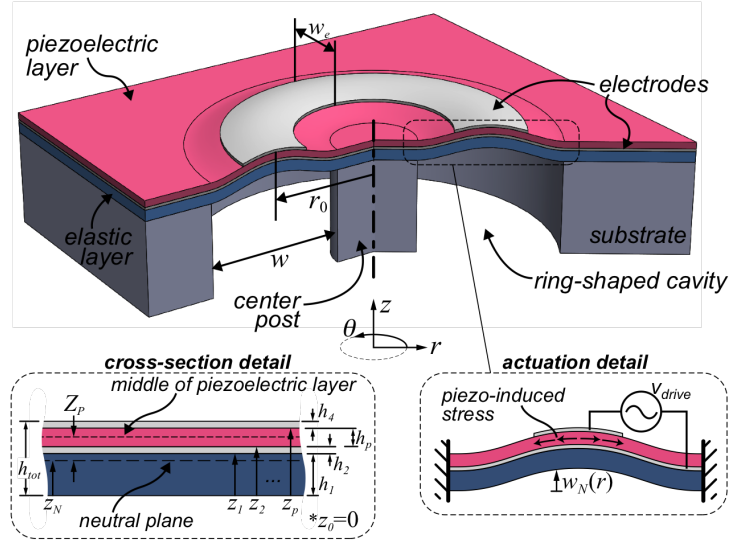
Figure 3.1: Conceptual cross-sectional diagram of the (deformed) ring-shaped PMUT, along with detail views showing the film composition and actuation mechanism.

constant-stress and constant-strain values are related by $\varepsilon^S = \varepsilon^T - d^t e$. While (3.2) and (3.3) are equivalent and related through the previously mentioned transformations, material properties are typically provided to the PMUT designer in strain-charge form, but analysis is often more convenient in the stress-charge form, so both will be utilized in this work.

In flexural piezoelectric transducers, transduction occurs due to the 31-mode piezoelectric effect. In thin-film systems, this is characterized by the effective piezoelectric constant $e_{31,\mathrm{f}}$, which is related to the material properties by

$$e_{31,\mathrm{f}} = e_{31} - \frac{c_{13}^E}{c_{33}^E} e_{33} = \frac{d_{31}}{s_{11}^E + s_{12}^E} = \frac{d_{31} Y_{0p}}{1 - \nu_p}, \tag{3.4}$$

where the subscript p denotes the piezoelectric layer, and the final equality reflects the assumption made in this work that all materials are transversely isotropic. As shown in the actuation detail in Figure 3.1, the structure is driven in an analogous manner to conventional PMUTs: an out-of-plane electric field $E_3 = V_e/h_p$ creates a transverse stress, which in turn generates a piezoelectric bending moment per unit transverse length [51]

$$M_p = \begin{cases} -e_{31,\mathrm{f}} Z_P V_e & \text{under electrode} \\ 0 & \text{no electrode,} \end{cases} \tag{3.5}$$

that in turn causes an out-of-plane deflection w_N. Here, Z_p is the distance from the mid-plane of the piezoelectric material to the neutral axis.

3.2.2 Free Vibration and Analytical Mode Shape

While it is not the basis for the equivalent circuit model, theoretical analysis identifies important parameters and provides foundation for the modeling approach, which is based on an assumed vibration mode shape. As thin structural members with transverse dimensions much larger than their thickness, PMUTs are modeled well as Kirchhoff-Love plates, which have been covered extensively in the literature (e.g., [51], [60]). Under the classical assumptions within Kirchhoff-Love plates, the general form of the governing equation for PMUT plate dynamics is given by

$$D_b \nabla^2 \nabla^2 w_N + \rho_s \frac{\partial^2 w_N}{\partial t^2} = P_{ext} + \nabla^2 M_P, \tag{3.6}$$

where P_{ext} is the external pressure, $\rho_s = \sum_i \rho_i h_i$ is the surface density, ρ_i is the density of the i-th layer, and D_b is the bending rigidity of the diaphragm [16]:

$$D_b = \sum_i \frac{Y_{0i}''}{3} [(z_i - z_N)^3 - (z_{i-1} - z_N)^3]. \tag{3.7}$$

Again using the illustrative case of a homogeneous diaphragm, the bending rigidity can be expressed as $D_b = Y_0'' h_{tot}^3 / 12$, however (3.7) must be evaluated for structures with more than one material.

Due to the natural symmetry of the system, we assume axisymmetric conditions (i.e. all quantities are constant in θ). Furthermore, it is well known that the deflection shape of plates is not appreciably changed by the presence of a fluid load [61], so we examine the mode shape by analyzing the steady-state harmonic motion of a free ($P_{ext} + \nabla^2 M_P = 0$) diaphragm. In this case, vibrations may only occur at set values of angular frequency $\omega = 2\pi f$ corresponding to specific modes, and the governing equation (3.6) simplifies to [62]

$$(\nabla^2 + \beta^2)(\nabla^2 - \beta^2)\hat{w}_N(r) = 0, \tag{3.8}$$

where $\hat{w}_N$ is the phasor representation of the modal displacement

$$w_N(r, t) = \hat{w}_N(r) \exp(j\omega t), \tag{3.9}$$

$j = \sqrt{-1}$ is the imaginary unit, and t is time. Furthermore, the frequency parameter β is related to the angular frequency and diaphragm properties by

$$\beta^4 = \frac{\omega^2 \rho_s}{D_b}, \tag{3.10}$$

and is constant for a given mode. The general solution to (3.8) is then given by [62]

$$\hat{w}_N = C_1 J_0(\beta r) + C_2 N_0(\beta r) + C_3 I_0(\beta r) + C_4 K_0(\beta r), \tag{3.11}$$

where $J_0(x)$ and $N_0(x)$ are Bessel functions of the first and second kind, and $I_0(x)$ and $K_0(x)$ are modified Bessel functions of the first and second kind. The constants β and C_i are determined by applying boundary conditions at the inner and outer diaphragm edges in a process that has been covered extensively in the literature (e.g., [63]). There are in general an infinite number of possible β which correspond to different vibration modes of the diaphragm, each having different C_i associated with it. Denoting the first axisymmetric mode (depicted in Figure 3.1) with subscript 00, this results in a transcendental frequency equation with eigenvalue $\lambda_{00} = \beta_{00}b$. Using this, the resonance frequency of the 00 mode may be related to the eigenvalue by

$$f_{00} = \frac{2\lambda_{00}^2}{\pi w_0^2 (AR+1)^2} \sqrt{\frac{D_b}{\rho_s}}, \tag{3.12}$$

where the aspect ratio $AR = 2r_0/w_0$ of the diaphragm has been defined as the ratio of the mean radius to the half-width, and it is worth noting that geometric restrictions limit the minimum value of AR to 1. The eigenvalue λ_{00} must be calculated numerically, and is generally regarded as dependent on a/b but with no approximations suggested. Parameterizing the problem with the aspect ratio AR, on the other hand, allows for a simple quadratic approximation of the eigenvalue

$$\lambda_{00}^2 \approx 5.564(AR+1)^2, \tag{3.13}$$

which, as shown in Figure 3.2, is accurate to within 0.8% error for $AR > 1.05$. Combining with (3.12), the excellent agreement between the numerical analysis and (3.13) suggests that resonance frequency $f_{00} \propto w_0^{-2}$ and is almost entirely unaffected by r_0, which supports the experimental findings from Chapter 2.

After determining the eigenvalue, the vibration mode shape $\phi(r)$ may be determined by using the boundary conditions to find C_{2-4} in (3.11), and choosing C_1 according to a normalization procedure of choice [63]. In this work, the mode shape is defined to take an average value of 1 over the vibrating area so that the mean displacement $w_m = \int_a^b r\hat{w}_N(r)dr/r_0w_0$ is related to $\hat{w}_N$ by

$$\hat{w}_N(r) = w_m\phi(r). \tag{3.14}$$

3.2.3 Assumed mode shape

The complex formulation and heavily involved process of determining the exact analytical mode shape can detract from the utility and widespread usage of a model based on it. In order to facilitate the development of an intuitive model that is easily implemented, we first approximate the deflection profile using an assumed mode shape:

$$\phi(r) = \frac{15}{8}\left(1 - \left(\frac{r-r_0}{w_0/2}\right)^2\right)^2 = \frac{15}{8}\left(1 - \bar{r}^2\right)^2, \tag{3.15}$$
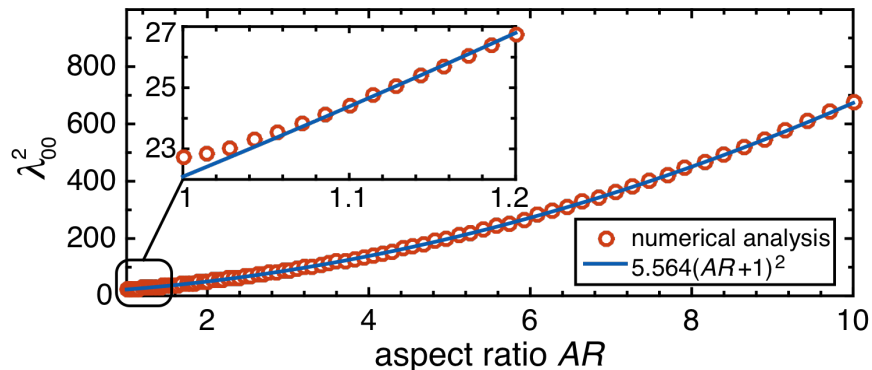
Figure 3.2: Results of numerical evaluation of the eigenvalue associated with the intended vibration mode, along with a quadratic fit.
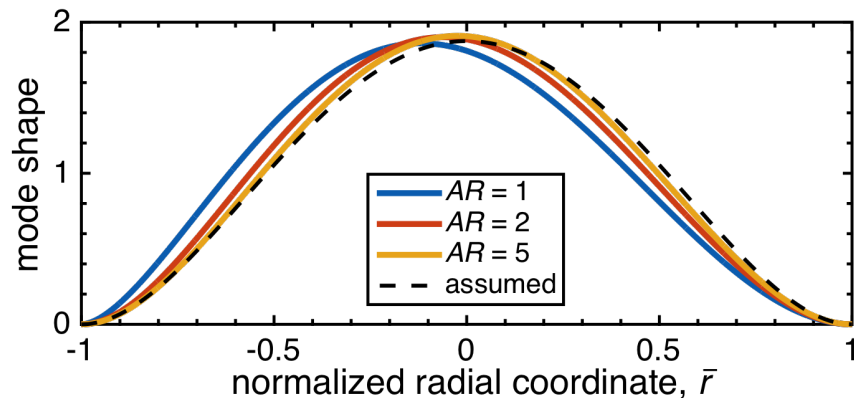
Figure 3.3: Comparison of analytical (solid) and assumed (dashed) mode shapes. In general, the analytical mode shapes for ring-shaped diaphragms with higher aspect ratios more closely correlate with the assumed value.

where the factor of 15/8 is to ensure that the average value over the vibrating area is 1, and $\bar{r} = 2(r - r_0)/w_0$ is the normalized radial coordinate. This mode shape was chosen by noting the similarities between a conceptually "unwrapped" ring-shaped diaphragm and a rectangular diaphragm that is clamped along its edges with length $2\pi r_0$ and free along its edges with length w_0; (3.15) is simply the static deflection shape of a clamped-free-clamped-free rectangular diaphragm subject to an evenly distributed pressure load [64] and parameterized to match the design and coordinate system of the ring-shaped structure. The validity of this approach is shown in Figure 3.3, which provides a comparison of the exact and assumed mode shapes. The assumed mode shape shows symmetry about the mean radius $\bar{r} = 0$, where the maximum deflection occurs. In contrast, the analytical mode shape is not exactly symmetrical and reaches its maximum at a radius $\bar{r} < 0$, however, this maximum occurs at $\bar{r} > -0.12$ for all AR, and at $\bar{r} > -0.06$ for $AR > 2$, where the two methods are in very good agreement. This suggests that a model based on (3.15) should be viable in most cases.

3.3 Equivalent Circuit Model

The electro-mechano-acoustical equivalent circuit, shown in Figure 3.4(a), is a common tool for concisely modeling PMUT dynamics. Not only does this circuit allow for direct evaluation of the frequency response and input impedance of the transducer, but it can also be extended to, for example, determine output acoustic powers, time-domain responses, transmit and receive sensitivities, and requirements for both down and upstream interface electronics [48], [50]. The left portion of the circuit in Figure 3.4(a) represents the electrical domain, the right represents the combined effects in the mechanical and acoustical domains, and the transformer represents the electromechanical transduction. Following the so-called impedance analogy, the mechanical flow variable is taken to be the mean velocity $u_m = dw_m/dt$ so that the assumed mode shape also describes the velocity profile as $u_N(r) = u_m\phi(r)$. Solving the system of equations defined by the equivalent circuit yields

$$i = \eta u_m + sC_0 V_e \tag{3.16}$$

$$\eta V_e = Z_{ma}u_m - F_{eq} = \left(sm_m + \frac{k_m}{s} + Z_a \right)u_m - F_{eq}, \tag{3.17}$$

where s is the complex frequency variable; V_e is the voltage across the electrodes; η is the transformer turns ratio; F_t (labeled in Figure 3.4(a)) is an equivalent transformer force due to the electrode voltage; F_{eq} is an equivalent applied force (e.g., an acoustic pressure from an external source); C_0 is the electrical clamped capacitance; and k_m, m_m, and Z_a are the mechanical stiffness, mechanical mass, and acoustic impedance, respectively. The sign convention utilized in defining the forces is such that a positive transformer or applied force results in a positive displacement. In the remainder of this section, expressions for each circuit element will be derived, and the resulting expressions are compiled at the conclusion of the section in Table I for convenience.

To be implemented in practice, several non-idealities that are not typically modeled may need to be introduced to this circuit, including a parasitic capacitance associated with traces and connections, and an electrical feedthrough resistance to represent dielectric loss [50]. Furthermore, the dominant damping source is assumed to be the acoustic medium, which is in contact with the topside of the PMUT only; while this is in general a valid assumption for liquid-coupled PMUT, in some cases it may be necessary to introduce a mechanical series resistance that models internal losses [50].

Figures 3.4(b) and (c) are the simplified drive-mode (F_{eq}=0) circuits used to calculate the electrical input impedance and the mean diaphragm velocity, respectively, as:

$$Z_{in} = \frac{V_{in}}{i} = \left(sC_0 + \frac{\eta^2 s}{s^2 m_m + sZ_a + k_m} \right)^{-1} \tag{3.18}$$

$$\frac{u_m}{V_{in}} = \frac{\eta s}{s^2 m_m + sZ_a + k_m}. \tag{3.19}$$
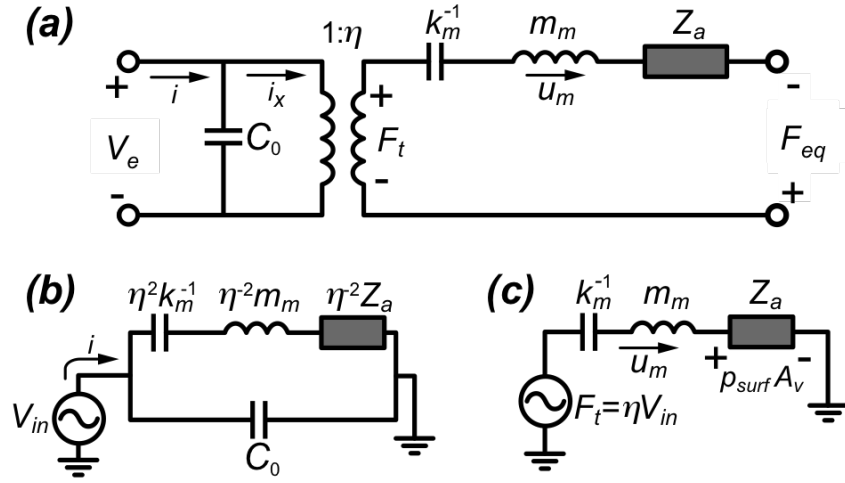
Figure 3.4: Diagram of the equivalent circuit used in this work; (a) most general form of the circuit, (b) and (c) simplified drive-mode circuits used to calculate input impedance and velocity, respectively.

Physically, the potential drop across the acoustic element Z_a in Figure 3.4(c) is related to the pressure generated at the PMUT surface p_{surf}, and the time-averaged acoustic power output is given as $P_{ac} = |u_m|^2 \text{Re}[Z_a]/2$ [48].

One common case that is useful for analysis is that of steady state harmonic vibration. In this case, $s = j\omega$ may be substituted in (3.16)-(3.19), and the mean velocity and displacement are related as $u_m = j\omega w_m$.

3.3.1 Hamilton's Principle and Piezoelectric Enthalpy Functional

In order to derive a model for a PMUT from energy arguments, it is convenient to utilize Hamilton's principle, which is a variational principle that in generalized form states [65]

$$\delta \int_{t_0}^{t_1} L \ dt + \int_{t_0}^{t_1} \delta W \ dt = 0, \tag{3.20}$$

where L is the Lagrangian and contains the energy content of the system related to conservative forces, and δW is the variational work done by all non-conservative forces. In our case, this principle is particularly useful in that it can lead to the governing equations for a system in terms of generalized coordinates which may, for instance, be modal displacements, and can include both electrical and mechanical variables. In purely mechanical systems the Lagrangian is the difference between kinetic and elastic energies, however for piezoelectric systems the relevant internal energy

functional is instead the electrical enthalpy $\tilde{H}$, which contains the elastic energy information, so that [66]

$$L = \int_V \left[\frac{1}{2}\rho u^2 - \tilde{H}(S, E) \right] dV = T - H \tag{3.21}$$

where the dependency of the electrical enthalpy on the strain and electric field is explicitly shown, T is the kinetic energy, and V refers to the volume of the system. As we will see in the following section, H can be expressed in terms of only material properties, w_m, and V_e, allowing the variations in T and H to respectively be expressed as

$$\delta T = \frac{\partial T}{\partial \dot{w}_m} \delta \dot{w}_m \tag{3.22}$$

$$\delta H = \frac{\partial H}{\partial w_m} \delta w_m + \frac{\partial H}{\partial V_e} \delta V_e, \tag{3.23}$$

where $(\dot{\ })$ denotes a derivative with respect to time. Furthermore, the variational work in (3.20) can be separated into mechanical and electrical terms as

$$\delta W = F_{eq} \delta w_m - Q \delta V_e, \tag{3.24}$$

where Q is the charge on the electrodes and the minus sign arises due to the fact that the effective electrical energy content of $\tilde{H}$ is opposite in sign to that of the dielectric energy density. Combining terms from (3.20)-(3.24) and using integration by parts yields [67]

$$\int_{t_0}^{t_1} \left\{ \left[F_{eq} - \frac{\partial H}{\partial w_m} - \frac{d}{dt}\left(\frac{\partial T}{\partial \dot{w}_m} \right) \right] \delta w_m - \left[Q + \frac{\partial H}{\partial V_e} \right] \delta V_e \right\} dt = 0, \tag{3.25}$$

from which the governing equations for the PMUT can be determined as

$$F_{eq} - \frac{\partial H}{\partial w_m} - \frac{d}{dt}\left(\frac{\partial T}{\partial \dot{w}_m} \right) = 0 \tag{3.26}$$

$$Q + \frac{\partial H}{\partial V_e} = 0. \tag{3.27}$$

3.3.2 Derivation of Lumped Parameters

At this point we will look to use our energy expressions in order to simplify the governing equations (3.26) and (3.27) into a form matching the circuit equations (3.16) and (3.17). We will do so first in the case of an unloaded (Z_a=0) transducer, and then incorporate acoustic effects in later sections. To begin, we note that if T and H can be expressed in terms of our previously defined variables as

$$T = \frac{1}{2}m_m u_m^2 \tag{3.28}$$

$$H = \frac{1}{2}k_m w_m^2 - \eta V_e w_m - \frac{1}{2}C_0 V_e^2, \tag{3.29}$$

then combined with (3.26) and (3.27) we obtain exactly (3.16) and (3.17). Therefore, in order to extract the lumped parameters for the circuit model, we equivalently seek to simplify our energy expressions into the form of (3.28) and (3.29).

The kinetic energy is straightforward to evaluate, and will be the first step in our lumped parameter derivation. From (3.21), we have

$$T = \int_V \frac{1}{2}\rho u^2 \, dV = \frac{1}{2}\rho_s u_m^2 \int_{A_v} \phi^2(r) \, dA_v, \tag{3.30}$$

where A_v is again the vibrating area. Comparing to (3.28), the mechanical mass may then be expressed as

$$m_m = 2\pi\rho_s \int_a^b \phi^2(r) r \, dr = \frac{20\pi}{7}\rho_s r_0 w_0. \tag{3.31}$$

A more in-depth analysis is required for the derivation of the terms involved in the electrical enthalpy, which is in general expressed as a function of S and E in matrix form as [66]

$$\tilde{H} = \underbrace{\frac{1}{2}S^t c^E S}_{\tilde{H}_1} \underbrace{-S^t e E}_{\tilde{H}_2} \underbrace{-\frac{1}{2}E^t \varepsilon^S E}_{\tilde{H}_3}. \tag{3.32}$$

In order to break (3.32) into terms that are more manageable, we define the three terms as $\tilde{H}_{1-3}$ as shown. To evaluate $\tilde{H}_1$, we note that Kirchoff-Love plate analysis implicitly assumes that all shear strains are negligible, in which case

$$\tilde{H}_1 = \frac{1}{2}\left[c_{11}^E S_{rr}^2 + 2c_{12}^E S_{rr}S_{\theta\theta} + c_{11}^E S_{\theta\theta}^2 + 2c_{13}^E \big(S_{rr} + S_{\theta\theta}\big)S_{zz} + c_{33}^E S_{zz}^2 \right], \tag{3.33}$$

where S_{rr}, $S_{\theta\theta}$, and S_{zz} are the normal strains in the $r-$, $\theta-$ and $z-$direction, respectively, and transverse isotropy has been assumed. Kirchhoff-Love plates further assume plane-stress conditions, so that (3.3) can be used, with $E = [0\ 0\ E_3]^t$ to show

$$S_{zz} = \frac{e_{33}}{c_{33}^E}E_3 - \frac{c_{13}^E}{c_{33}^E}\big(S_{rr} + S_{\theta\theta}\big). \tag{3.34}$$

Combining with (3.33), this yields

$$\tilde{H}_1 = \frac{1}{2}\left[\left(c_{11}^E - \frac{c_{13}^{E\,2}}{c_{33}^E}\right)S_{rr}^2 + 2\left(c_{12}^E - \frac{c_{13}^{E\,2}}{c_{33}^E}\right)S_{rr}S_{\theta\theta} + \left(c_{11}^E - \frac{c_{13}^{E\,2}}{c_{33}^E}\right)S_{\theta\theta}^2 + \frac{e_{33}^2}{c_{33}^E}E_3^2 \right]. \tag{3.35}$$

We may simplify further by using the relations

$$c_{11}^E - \frac{c_{13}^{E\,2}}{c_{33}^E} = \left[s_{11}^E\left(1 - \left(\frac{s_{12}^E}{s_{11}^E}\right)^2\right) \right]^{-1} = \frac{Y_0}{1 - \nu^2} \tag{3.36}$$

$$c_{12}^E - \frac{c_{13}^{E\,2}}{c_{33}^E} = \nu\left(c_{11}^E - \frac{c_{13}^{E\,2}}{c_{33}^E} \right) \tag{3.37}$$

to arrive at our final expression for $\tilde{H}_1$:

$$\tilde{H}_1 = \frac{1}{2}Y_0''\left(S_{rr}^2 + 2\nu S_{rr}S_{\theta\theta} + S_{\theta\theta}^2\right) + \frac{1}{2}\frac{e_{33}^2}{c_{33}^E}E_3^2. \tag{3.38}$$

In a similar process, we may express the second electrical enthalpy term as

$$\tilde{H}_2 = -\left[e_{31}\left(S_{rr} + S_{\theta\theta}\right)E_3 + e_{33}S_{zz}E_3\right]. \tag{3.39}$$

By utilizing (3.34) and the first equality of (3.4), this simplifies to

$$\tilde{H}_2 = -e_{31,\mathrm{f}}\left(S_{rr} + S_{\theta\theta}\right)E_3 - \frac{e_{33}^2}{c_{33}^E}E_3^2. \tag{3.40}$$

Finally, we evaluate the third electrical enthalpy term in an analogous manner to obtain

$$\tilde{H}_3 = -\frac{1}{2}\left(\varepsilon_{33}^T - 2d_{31}e_{31} - d_{33}e_{33}\right)E_3^2. \tag{3.41}$$

With all three terms from the electrical enthalpy simplified, we are now positioned to extract the lumped parameters for the model. As can be seen in (3.38), (3.40), and (3.41), the electrical enthalpy contains three types of terms: the terms that depend only on strains correspond to strain energy density, those that depend only on the electric field correspond to electrical energy density, and those that depend on both strain and electrical field correspond to piezoelectric coupling energy density. After integrating throughout the volume of the PMUT diaphragm, we therefore regroup the terms according to their physical meaning as:

$$H = \int_V \tilde{H}dV = H_{\mathrm{strain}} + H_{\mathrm{coupl}} + H_{\mathrm{elec}} \tag{3.42}$$

$$H_{\mathrm{strain}} = \frac{1}{2}\int_V Y_0''\left(S_{rr}^2 + 2\nu S_{rr}S_{\theta\theta} + S_{\theta\theta}^2\right)dV \tag{3.43}$$

$$H_{\mathrm{coupl}} = -\int_V e_{31,\mathrm{f}}\left(S_{rr} + S_{\theta\theta}\right)E_3\,dV \tag{3.44}$$

$$H_{\mathrm{elec}} = -\frac{1}{2}\int_V \left(\varepsilon_{33}^T - 2d_{31}e_{31} - d_{33}e_{33} + \frac{e_{33}^2}{c_{33}^E}\right)E_3^2\,dV. \tag{3.45}$$

Noting the similarity between (3.29) and (3.42), we will find that H_{strain}, H_{coupl}, and H_{elec} yield k_m, η, and C_0, respectively.

Mechanical Stiffness

Moving forward with the evaluation of the strain term, we utilize the relationship between transverse strains and local curvature in axisymmetric thin diaphragms [51]

$$S_{rr} = -z\frac{\partial^2 w_N}{\partial r^2} \tag{3.46}$$

$$S_{\theta\theta} = -\frac{z}{r}\frac{\partial w_N}{\partial r}, \tag{3.47}$$

where z is measured from the neutral plane as defined in (3.1). It has been assumed that deflections are small relative to the thickness and that the transverse stress along the neutral axis is negligible. These assumptions are analogous to claiming that bending is the dominant energy storage mechanism and that membrane (stretching) action may be neglected; while this is typically a good approximation, several factors such as large deflections or high residual film stresses may introduce errors. Combining with (3.14), (3.46), and (3.47) allows (3.43) to be expressed as

$$H_{\text{strain}} = 2\pi w_m^2 \int_{\text{bot}}^{\text{top}} Y_0'' z^2 \, dz \int_a^b \left[\left(\frac{\partial^2 \phi}{\partial r^2} \right)^2 + \frac{2\nu}{r}\frac{\partial^2 \phi}{\partial r^2}\frac{\partial \phi}{\partial r} + \left(\frac{1}{r}\frac{\partial \phi}{\partial r} \right)^2 \right] r \, dr. \tag{3.48}$$

Here, the first integral is the bending rigidity D_b and is equivalent to (3.7), and the second integral has been used commonly in the literature and is often referred to simply as an elastic or mechanical integral (e.g., [16], [58], [32]), however its derivation has thus far remained elusive and the exact expression changes slightly in each work, making it difficult to adapt to new models. Furthermore, H_{strain} is now revealed to be proportional to w_m^2 and independent of electric field so that it may be equated to the first term in (3.29), at which point mean displacement terms cancel and k_m can be expressed as

$$k_m = \frac{480\pi D_b r_0}{w_0^3}\left[\frac{15}{4}AR(1-AR^2)^2\text{acoth}(AR) + 1 + \frac{25}{4}AR^2 - \frac{15}{4}AR^4 \right]. \tag{3.49}$$

The bracketed term in (3.49) is approximately (to within 2.6% error) constant and equal to 3 for $AR > 2$. We therefore use this value to simplify (3.49) in order to promote an intuitive understanding of the system and arrive at the mechanical stiffness expression used in the remainder of this dissertation:

$$k_m = \frac{1440\pi D_b r_0}{w_0^3}. \tag{3.50}$$

Transformer Turns Ratio

Next, we evaluate the coupling term in (3.42) in order to derive the transformer turns ratio η. Noting that the electric field is zero outside of the active piezoelectric that is covered by top electrode, and
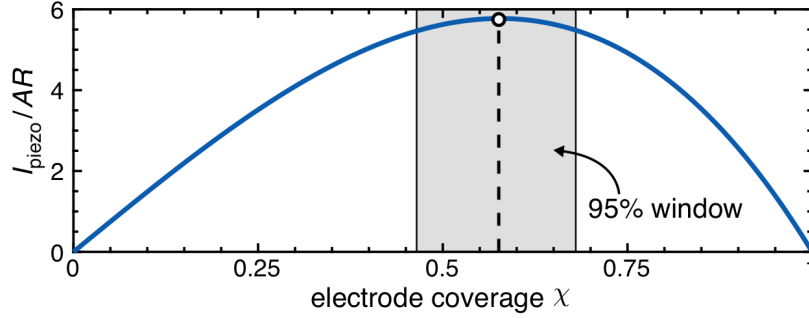
Figure 3.5: Piezoelectric coupling integral, which is proportional to the transformer turns ratio, normalized by the aspect ratio. The optimal electrode coverage is 0.57 as labeled, however, electrode coverage between 0.47 and 0.68 results in coupling that is within 95% of the optimal value.

again utilizing the strain-displacement relations in (3.46) and (3.47), (3.44) becomes

$$H_{\mathrm{coupl}} = -e_{31,\mathrm{f}}E_3 \int_{z_p-h_p-z_N}^{z_p-z_N} z\, dz \int_{A_e} \frac{\partial^2 w_N}{\partial r^2} + \frac{1}{r}\frac{\partial w_N}{\partial r}\, dA_e, \tag{3.51}$$

where $A_e = \pi(b_e^2 - a_e^2)$ is the area covered by top electrode. Simplifying, we find

$$H_{\mathrm{coupl}} = 2\pi e_{31,\mathrm{f}} Z_p I_{\mathrm{piezo}} w_m V_e, \tag{3.52}$$

where Z_p is the distance from the mid-plane of the active piezoelectric to the neutral axis, and I_{piezo} is an integral of the strains within the electroded region that represents how well-coupled a certain electrode configuration is to a specific mode:

$$I_{\mathrm{piezo}} = -\int_{a_e}^{b_e} \left(\frac{\partial^2 \phi}{\partial r^2} + \frac{1}{r}\frac{\partial \phi}{\partial r} \right) r\, dr. \tag{3.53}$$

Comparing (3.52) to the posited form of H in (3.29) yields the general equation for the transformer turns ratio

$$\eta = 2\pi e_{31,\mathrm{f}} Z_p I_{\mathrm{piezo}}. \tag{3.54}$$

In general, the optimal electrode layout will maximize I_{piezo} and will only cover a portion of the diaphragm that has bending strains in the piezoelectric layer of the same sign; otherwise parts of the diaphragm will be working against each other. Due to the symmetry of the assumed mode shape about $r = r_0$, the optimal electrode will be centered on the released diaphragm so that (3.53) can be expressed in terms of the electrode coverage ratio $\chi = w_e/w_0$ as

$$I_{\mathrm{piezo}} = 15\left(\frac{2r_0}{w_0}\right)\chi\left(1 - \chi^2\right). \tag{3.55}$$

As shown in Figure 3.5, I_{piezo} reaches a maximum at $\chi = \sqrt{2}/2 \approx 0.57$, and is within 95% of the maximum for $0.47 < \chi < 0.68$. For simplification, we use $\chi = 1/2$ in the remainder of this work

as a nearly optimized value, allowing the turns ratio to be expressed in its final form as

$$\eta = \frac{45\pi}{4}\left(\frac{2r_0}{w_0}\right)e_{31,\text{f}}Z_p. \tag{3.56}$$

Clamped Capacitance

The final lumped parameter that must be derived for our unloaded PMUT is the electrical clamped capacitance. Beginning with the H_{elec} term expressed in (3.45) we may use the first equality of (3.4) along with the relation $e_{33} = 2d_{31}c_{13}^E + d_{33}c_{33}^E$ to obtain

$$H_{\text{elec}} = -\frac{1}{2}\left(\varepsilon_{33}^T - 2d_{31}e_{31,\text{f}}\right)h_p A_e E_3^2. \tag{3.57}$$

Equating this with the final term from (3.29) yields a relation between the clamped capacitance C_0 and the free capacitance C_f:

$$C_0 = (1 - k_{31}^2)C_f \tag{3.58}$$

$$C_f = \frac{\varepsilon_{33}^T A_e}{h_p}, \tag{3.59}$$

where the coupling coefficient k_{31}^2 is the typical value for 31-mode piezoelectric actuation in diaphragms:

$$k_{31}^2 = \frac{2d_{31}e_{31,\text{f}}}{\varepsilon_{33}^T}. \tag{3.60}$$

The coupling coefficient is a material-specific parameter representing an upper limit on the amount of input electrical energy that can be stored as mechanical energy during static actuation, and is in this way a measure of efficiency.

3.3.3 Resonance Frequency without Acoustic Load

In the case of undamped harmonic free vibration, energy conservation dictates that the maximum kinetic energy reached in one cycle is equal in magnitude to the maximum potential energy reached in one cycle, therefore

$$\omega_0^2 m_m |w_m|^2 = k_m |w_m|^2, \tag{3.61}$$

allowing the resonance frequency $f_0 = w_0/2\pi$ to be solved for explicitly:

$$f_0 = \frac{\sqrt{126}}{\pi w_0^2}\sqrt{\frac{D_b}{\rho_s}} \approx \frac{3.573}{w_0^2}\sqrt{\frac{D_b}{\rho_s}}. \tag{3.62}$$
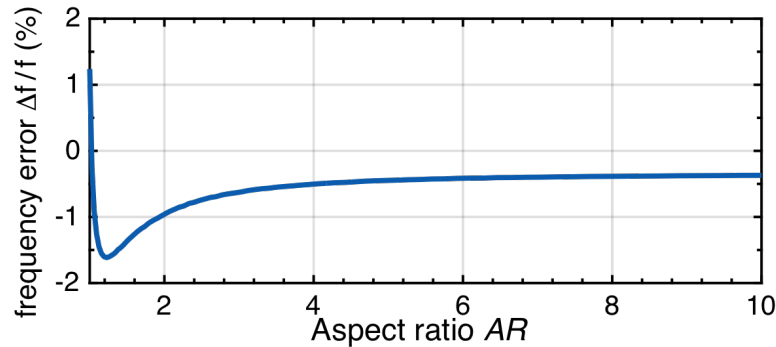
Figure 3.6: Fractional frequency error between analysis and model, showing a strong correlation between the two methods.

In corroboration with the experimental results in the preceding chapter and the theoretical analysis in the preceding section, (3.62) suggests that, because both k_m and m_m are proportional to r_0, resonance frequency is independent of r_0. As previously mentioned, this is significant in that it allows for an extra degree of design freedom and the ability to achieve a wider range of performances within manufacturing constraints, since the layout geometry of ring-shaped PMUTs is not fully constrained by the film stack and desired frequency as is the case for conventional PMUTs.

It is essential that the equivalent circuit model predict the resonance frequency with a high degree of accuracy. Combining (3.12) and (3.62), the fractional frequency error between the theoretical and modeled values, which is shown as a function of aspect ratio in Figure 3.6, may be expressed as:

$$\frac{\Delta f}{f} = \frac{f_{0,\text{theory}} - f_{0,\text{model}}}{f_{0,\text{theory}}} = 1 - (AR + 1)^2 \frac{\sqrt{126}}{2\lambda_{00}^2}. \tag{3.63}$$

The theory and model show excellent agreement, as the fractional frequency error does not exceed 1.7% for any aspect ratio, and is less than 1% for $AR > 2$, where it is expected that the assumed mode shape is a good approximation. These results also indicate that the circuit model should overestimate the resonance frequency by about 0.4% at large AR.

3.3.4 Acoustic Radiation Impedance

As a PMUT vibrates in the presence of an acoustic medium, it generates an acoustic pressure p_a at the transducer surface that imparts a force back on the diaphragm, thereby affecting the dynamics of the device. In keeping with the derivation approach used in the electromechanical equivalent circuit components, we begin with the expression for the virtual work δW_a performed by the

acoustic pressure

$$\delta W_a = \int_{A_v} p_a \delta w_N \, dA_v. \tag{3.64}$$

Under the assumption made here that the PMUT deflection is entirely characterized by the first vibration mode, we may express the virtual displacement δw_N as [67]

$$\delta w_N = \frac{\partial w_N}{\partial w_m} \delta w_m = \phi(r) \delta w_m, \tag{3.65}$$

so that (3.64) simplifies to

$$\delta W_a = \left[\int_{A_v} p_a(r) \phi(r) \, dA_v \right] \delta w_m = F_a \delta w_m, \tag{3.66}$$

where F_a is the equivalent force applied by the acoustic medium, and the final equality reflects the fact that equivalent forces are by definition the ratio between virtual work and virtual displacement. Furthermore, as impedances are defined as the ratio between force and velocity, the acoustic impedance can be expressed as

$$Z_a = \frac{1}{u_m} \int_{A_v} p_a(r) \phi(r) \, dA_v. \tag{3.67}$$

It should be noted that (3.67) is equivalent to the commonly used power-based definition of acoustic impedance [48], as should be expected.

In order to evaluate the acoustic impedance, the PMUT is assumed to be in a rigid baffle, allowing the frequency-dependent axisymmetric pressure profile to be found by integrating the pressures generated at radius r by each infinitesimal vibrating area dA'_v, with the coordinate system and geometry defined in Figure 3.7:

$$p_a(r) = j\frac{\rho_a c_a k}{2\pi} \int_{A_v} u_N(r', \theta') \frac{e^{-jkr'}}{r'} \, dA'_v, \tag{3.68}$$

where ρ_a and c_a are the mass density and sound speed of the acoustic medium, respectively, and $k = 2\pi/\lambda = 2\pi f/c_a$ is the wavenumber. Often termed the Rayleigh integral, (3.68) is one of the most commonly used integrals in acoustics [48]. Essentially, it shifts the origin to the labeled point at (r, θ) and then solves for the pressure at the origin, where the choice of origin is necessary to avoid a singularity at $r' = 0$ during evaluation. By relating the mean velocity to u_N, the acoustic impedance may be expressed in terms of the mode shape and acoustic medium properties only:

$$Z_a = j\rho_a c_a k \int_a^b \left[\iint_{A_v} \phi(r', \theta') e^{-jkr'} dr' d\theta' \right] \phi(r) r \, dr, \tag{3.69}$$

where trigonometry can be used to express the mode shape in terms of r' and θ' (see Appendix A). It is often convenient to simplify the acoustic impedance into its real and imaginary components as

$$Z_a = R_a + jX_a = \rho_a c_a A_v (r_a + jx_a), \tag{3.70}$$
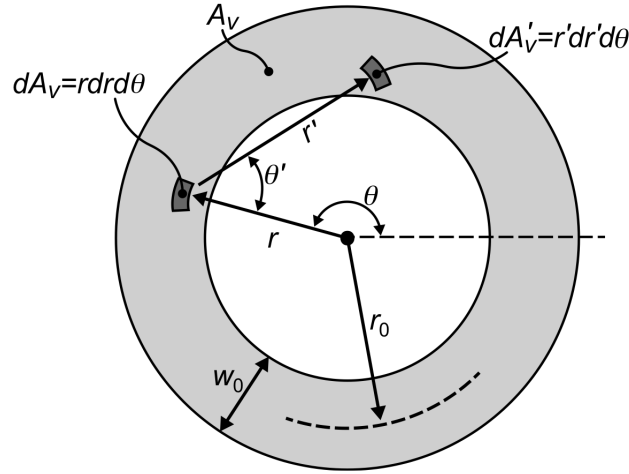
Figure 3.7: Geometry and coordinates used for calculating the acoustic impedance.

where r_a and x_a are the dimensionless acoustic radiation resistance and reactance, respectively. The resistive component of the impedance represents the transfer of energy from the PMUT to the acoustic medium (i.e. the generation of acoustic power), and for this reason it is typically desired that r_a is maximized. Conversely, the reactive component of the acoustic impedance has no similar contribution to the device performance, and instead is an inertial term that represents an additional acoustic mass given by

$$m_a = \rho_a c_a A_v \frac{x_a}{\omega}. \tag{3.71}$$

As is typical, the acoustic impedance scales with the specific acoustic impedance of the medium $\rho_a c_a$ meaning that a PMUT operating in a liquid experiences significantly higher damping and mass-loading than the same device in air.

Evaluation of the integrals in (3.69) is quite difficult, in part due to the interdependence of integration limits on r' and θ', and has therefore been addressed with a variety of mode shapes in the literature. For example, although not specifically provided, the acoustic impedance of a clamped-free annular disk vibrating in a flexural mode was used to estimate acoustic power output by Lee and Singh [68], and was evaluated by using polynomial approximations of the mode shape and discretizing the disk into concentric annuli, each with uniform velocity. Conversely, Rdzanek and Rdzanek [69] analytically derived an asymptotic formula for the acoustic impedance of an elastically supported annular plate that is valid for high frequencies where $k > \beta_{00}$, however the inaccuracy of the asymptotic formula at lower frequencies makes it unsuitable for the modeling in this work. In the field of MUTs, Ozergerluk *et al.* reported on the acoustic impedance of collapse-mode CMUTs, which have a similar annular symmetery to ring-shaped PMUTs. The acoustic impedance was noted to be functions of radial dimensions, however the nature of this relation was omitted as the trends were unclear and difficult to use as grounds for intuition. In aims of developing such a physical understanding and of elucidating trends in the acoustic impedance of a ring-shaped PMUT, results based on an easily implemented numerical method described in
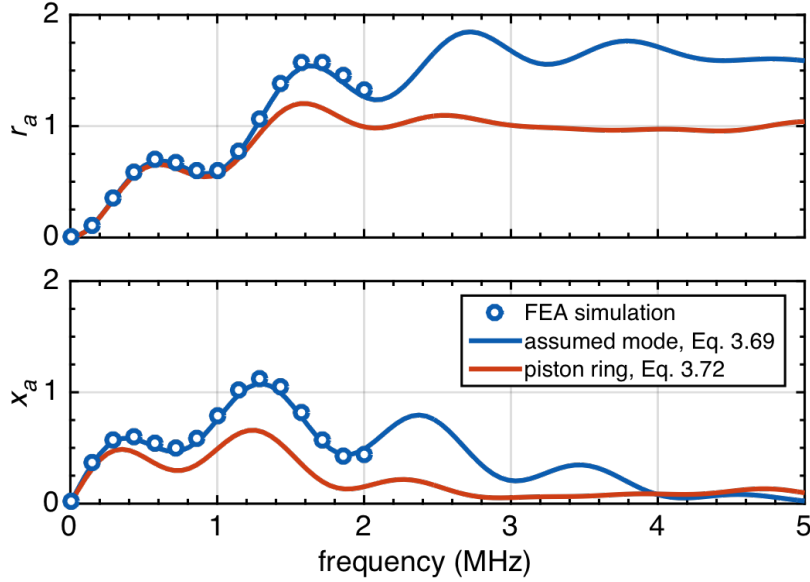
Figure 3.8: Nondimensional acoustic resistance and reactance, as calculated using FEA simulations, numeric integration of (3.69) with the assumed mode shape, and the analytical expression for a piston vibrator (3.72).

Appendix A and carried out in Matlab (R2015a, Mathworks Inc., Natick, MA, USA) are presented here.

On the other hand, one method of simplification that is commonly used to estimate the acoustic impedance of typical PMUT is to approximate the device as a piston vibrator, where $\phi(r) = 1$, with the same volumetric velocity. While even in this simplified case the acoustic impedance has no closed-form solution, the complicated triple integral in (3.69) may be simplified to a combination of closed-form impedances of circular piston vibrators and a single integral that is readily evaluated numerically [70]. In one formulation [71], Bouwkamp expressed the acoustic impedance of a ring-shaped piston vibrator as

$$Z_a = \rho_a c_a \lambda^2 \left(Z_{cp}(\alpha) + Z_{cp}(\beta) + \frac{j\alpha\beta}{\pi} \int_0^\infty \frac{J_1(\alpha s) J_1(\beta s)}{s\sqrt{s^2 - 1}} \, ds \right), \tag{3.72}$$

where $\alpha = ka$, $\beta = kb$, and $Z_{cp}(x)$ is a normalized acoustic impedance of a circular piston:

$$Z_{cp}(x) = \frac{x^2}{4\pi} \left(1 - \frac{J_1(2x)}{x} + j\frac{H_1(2x)}{x} \right), \tag{3.73}$$

where $J_1(x)$ and $H_1(x)$ are the first order Bessel and Struve functions, respectively.

Figure 3.8 presents a comparison of the three different methods of calculating the acoustic impedance of a ring-shaped PMUT: the numeric integration of (3.69) used in this work, the piston

vibrator approximation of (3.72), and FEA simulations. All data is for ring-shaped PMUT with mean radius $r_0 = 150\,\mu$m, width $w_0 = 100\,\mu$m, and air as the acoustic medium. The FEA setup follows the discussion in Section IV-A, with the exception of a total AlN thickness of $10\,\mu$m; the large thickness is chosen in order to reduce the contribution of higher order vibration modes that occur at high frequencies.

As should be expected due to their similarities, the three evaluation methods exhibit similar magnitude, periodicity, and overall behavior. The FEA and numerical method predict nearly identical impedances at all simulated frequencies, with the minor differences being caused by discrepancies between the simulated and assumed vibration shape. Conversely, the piston approximation is valid only at sufficiently low frequencies that $ka < kb \ll 1$, where both the piston and flexural vibrator act as quasi-point sources. However, when the transducer size becomes comparable to the acoustic wavelength, the solutions begin to diverge and the flexural vibrator exhibits acoustic impedance that is greater than that of its piston counterpart. This trend continues into the high frequency regime where $kb > ka \gg 1$. Despite correctly predicting the acoustic impedance as mostly resistive, the piston approximation severely underestimates the value of the acoustic resistance, and for a range of frequencies, the acoustic reactance.

The lack of a closed-form solution makes an intuitive understanding of the acoustic impedance of a ring difficult to obtain and, as is discussed in the subsequent section and more notably in Chapter 4, the nature of the dimensionless acoustic impedance $z_a = r_a + jx_a$ may have substantial impacts on device performance; for this reason, numerical evaluation of (3.69) is performed and provided in Figure 3.9 to allow the reader insight on the dependence of $|z_a|$ on the mean radius, width, and acoustic medium. As the sound speed of the acoustic medium is increased, the dimensionless impedance curves become more gradual with respect to frequency as shown in Figure 3.9(a), but changes in density have no effect. In Figure 3.9(b) it is shown that as r_0 is increased at fixed w_0, the periodicity of z_a changes and local maxima and minima shift to lower frequencies. In fact, if Figures 3.9(a) and (b) were parameterized with respect to $kr_0 = 2\pi r_0 f/c_a$ rather than frequency, all curves would show the same periodicity, with slight changes in magnitude due to changes in r_0, suggesting that the periodic behavior of the acoustic impedance is determined by c_a and r_0. In other words, the local maxima and minima occur at the same values of kr_0 for all curves. This interesting behavior is in part due to these geometries typically being in a regime where $2r_0 > \lambda$ but $w_0 < \lambda$, so that some dimensions are acoustically large and some are not. These behaviors are further confirmed in Figure 3.9(c), where it is shown that increasing w_0 while maintaining $r_0 = 250\,\mu$m solely impacts the magnitude of z_a, and not its periodic behavior.
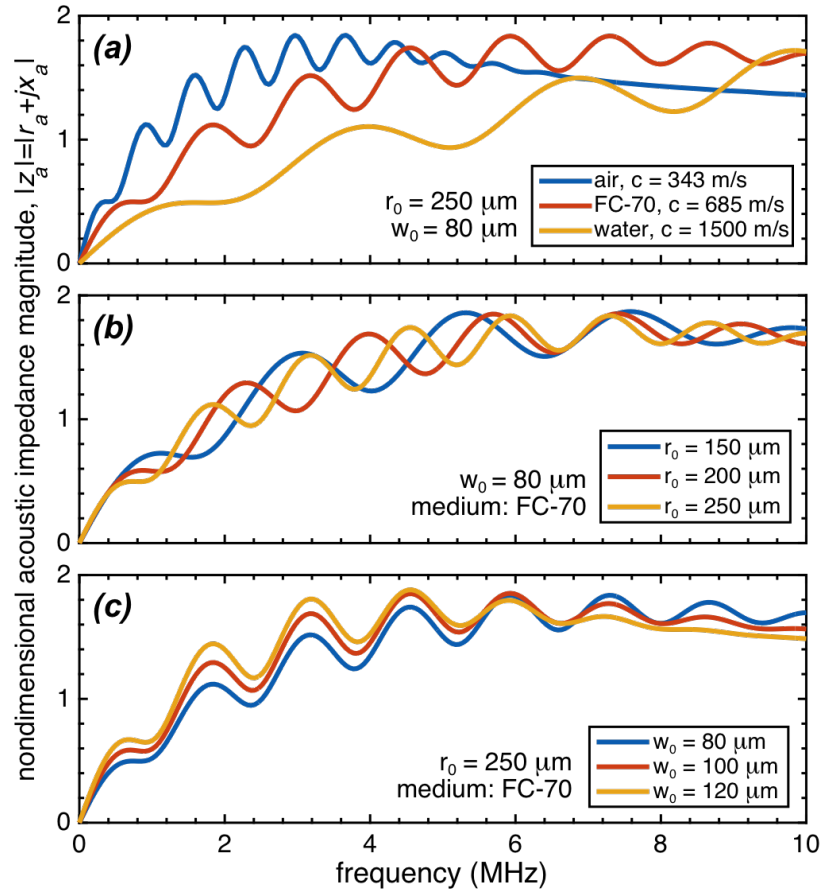
Figure 3.9: Trends in the nondimensional acoustic impedance with changes in (a) acoustic media, (b) mean radius, and (c) width. All curves use the assumed mode shape and are calculated via numeric integration of (3.69).

3.4 Model Validation and PMUT Performance

Throughout the circuit model development, minor validation exercises were performed. However, in order to ensure the model captures all of the relevant phenomena with sufficient accuracy, a more rigorous validation is provided in this section through the use of FEA. This section is separated into three subsections: (1) finite element model setup, (2) air-coupled performance, and (3) liquid-coupled performance; the latter two sections focus on the validation of the circuit model through parameter sweeps and comparisons of the frequency responses calculated with the developed circuit model and FEA, along with typical performance metrics used to characterize PMUTs.

Table 3.1: Equivalent Circuit Parameters

Parameter		Expression
Clamped capacitance	C_0	$(1 - k_{31}^2)C_f$
Free capacitance	C_f	$\dfrac{\varepsilon_{33}^T \pi (b_e^2 - a_e^2)}{h_p}$
Coupling coefficient	k_{31}^2	$\dfrac{2d_{31}e_{31,\text{f}}}{\varepsilon_{33}^T}$
Transformer turns ratio	η	$\dfrac{45\pi}{4}\left(\dfrac{2r_0}{w_0}\right)e_{31,\text{f}}Z_p$
Mechanical mass	m_m	$\dfrac{20\pi}{7}\rho_s r_0 w_0$
Mechanical stiffness	k_m	$\dfrac{1440\pi D_b r_0}{w_0^3}$
Acoustic radiation impedance	Z_a	numeric integration of (3.69)

3.4.1 Finite Element Analysis Setup

An illustration of the FEA setup, which is performed in Comsol Multiphysics v5.0 (Comsol Inc., Burlington, MA, USA), is provided in Figure 3.10. The PMUT is modeled as a vibrating diaphragm in an infinite rigid baffle, the system is solved with the acoustic-piezoelectric interaction interface, and the geometry is defined as 2D-axisymmetric, which inherently enforces the assumption that all quantities are constant in θ. The acoustic-piezoelectric interaction interface includes three coupled physics modules: acoustics, solid mechanics, and electrostatics. The former two are coupled through enforcement of continuity of pressure and velocity at the acoustic-structure boundary, and the latter two are coupled through the standard piezoelectric relations. In order to avoid excessive meshing, the thin electrodes are omitted as solid domains and are modeled instead as constant-voltage boundaries with a 1 V_{ac} signal applied across them. The materials of both the transduction ($h_{top} = 0.5\,\mu\text{m}$) and elastic ($h_{bot} = 1\,\mu\text{m}$) PMUT layers are AlN, which we define in Comsol as a transversely isotropic material by manually defining the c^E and d matrices. The constants used to define AlN in both FEA simulations and the equivalent circuit model, including the value of $e_{31,\text{f}}$ calculated using the final equality in (3.54), are compiled in Table II for reference. This simulation setup is equivalent to the one used in Chapter 2, with the only changes being the values of h_{bot} and h_{top}, and was shown to have a strong correlation with experimentally observed behavior of fabricated ring-shaped PMUTs.

In the acoustic domain, special care must be taken to properly simulate acoustic radiation into free space and to avoid reflections, which are often problematic with wave physics. Perfectly
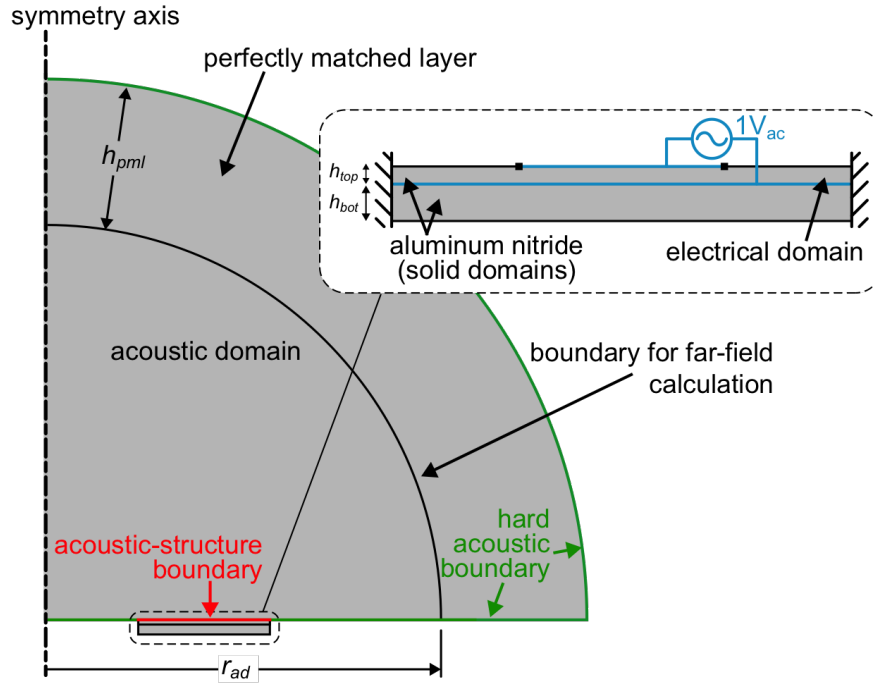
Figure 3.10: Diagram of geometry used in FEA. The boundaries of the diaphragm are clamped, infinite impedance acoustic boundaries are shown in green, blue denotes constant-voltage boundaries where an ac signal is applied, red indicates boundaries where the structural and acoustical physics are coupled, and the perfectly matched layer simulates a semi-infinite domain.

Table 3.2: Aluminum nitride material properties and dimensions used in FEA and Equivalent Circuit

Parameter		Value
AlN density	ρ	$3300\,\mathrm{kg/m^3}$
AlN Young's modulus	Y_0	$349.8\,\mathrm{GPa}$
AlN Poisson's ratio	ν	0.3
AlN constant-stress dielectric constant	ε_{33}^T	$10.26\varepsilon_0$
Permittivity of free space	ε_0	$8.854\,\mathrm{pF/m}$
AlN transverse piezoelectric charge constant	d_{31}, d_{32}	$-2.2\,\mathrm{pm/V}$
AlN c-axis piezoelectric charge constant	d_{33}	$5\,\mathrm{pm/V}$
AlN effective transverse piezoelectric constant	$e_{31,f}$	$-1.1\,\mathrm{C/m^2}$
Thickness of top AlN layer	h_{top}	$0.5\,\mathrm{\mu m}$
Thickness of bottom AlN layer	h_{bot}	$1\,\mathrm{\mu m}$

matched layers (PMLs) eliminate these issues by using coordinate stretching to effectively apply an exponential decay to waves traveling through them, so that waves entering the PML will return to the standard acoustic domain with sufficiently low amplitude that they do not impact the results. In this way, PMLs mimic semi-infinite domains while keeping the standard acoustic domain, here defined by a quarter-circle with radius, $r_{ad} = r_0 + 5w_0/2$, sufficiently small that simulation efforts are manageable. The PML thickness h_{pml} is typically $200\,\mu\text{m}$, but is ensured to be sufficient that the sound pressure level along the outer boundary is at least 100 dB below the maximum. This approach was verified by comparing to results with a spherical wave radiation condition on an acoustic domain that extends well into the far-field. If desired, the acoustic pressure outside of the simulation domain can also be calculated by utilizing the far-field calculation interface on the boundary labeled in Figure 3.10.

3.4.2 Air-coupled Performance

As a first validation of the circuit model, parameter sweep simulations over different values of r_0 and w_0 were performed with air ($c_a = 343.2\,\text{m/s}$, $\rho_a = 1.2\,\text{kg/m}^3$) as the acoustic medium. The effect of changing w_0 with a fixed value of $r_0 = 250\,\mu\text{m}$ is first examined in Figures 3.11(a)-(c). As should be expected due to the relatively small acoustic loading in air-coupled operation, the displacement frequency response is similar to conventional PMUTs and many other MEMS systems: a single, sharp peak near the first resonance is observed, and an increase in distance between anchors corresponds to both an increase in low-frequency displacement and a decrease in resonance frequency due to a decrease in stiffness k_m. Furthermore, strong correlations between the standard metrics of low-frequency displacement, quality factor, displacement at resonance, and resonance frequency indicate an excellent agreement between the modeled and simulated performances. The resonance frequency scales with w_0^{-2} as predicted by the equivalent circuit in (3.62), which also consistently overestimates the resonance frequency by the expected amount of about 0.4% due to the mismatch between assumed and exact mode shapes. In terms of the utility of the model, however, this is likely insignificant because: (a) it is typically unnecessary for PMUTs to resonate precisely at a predetermined frequency, and (b) fabrication intolerances and film stresses are expected to cause larger than 0.4% errors in frequency in practice.

The agreement between model and simulation is further supported in Figure 3.11(b), where the DC mean displacement w_{DC} and quality factor Q versus w_0 are explicitly shown. The simulated values for Q and w_{DC} are respectively defined as $Q = f_0/\Delta f_{3dB}$, where Δf_{3dB} is the 3 dB displacement bandwidth, and as the mean displacement at the lowest simulated frequency (about $0.1f_0$). It should be noted that 3 dB bandwidths are used here for analytic tractability, although 6 dB bandwidths are more commonly reported in the literature. While the numerical evaluation and frequency-dependent nature of the acoustic impedance make it difficult to extract an exact formula for Q from the circuit model, simplifications can typically be made for air-coupled PMUT, where the acoustic impedance is sufficiently small that $m_m \gg m_a$ so the acoustic mass-loading effects
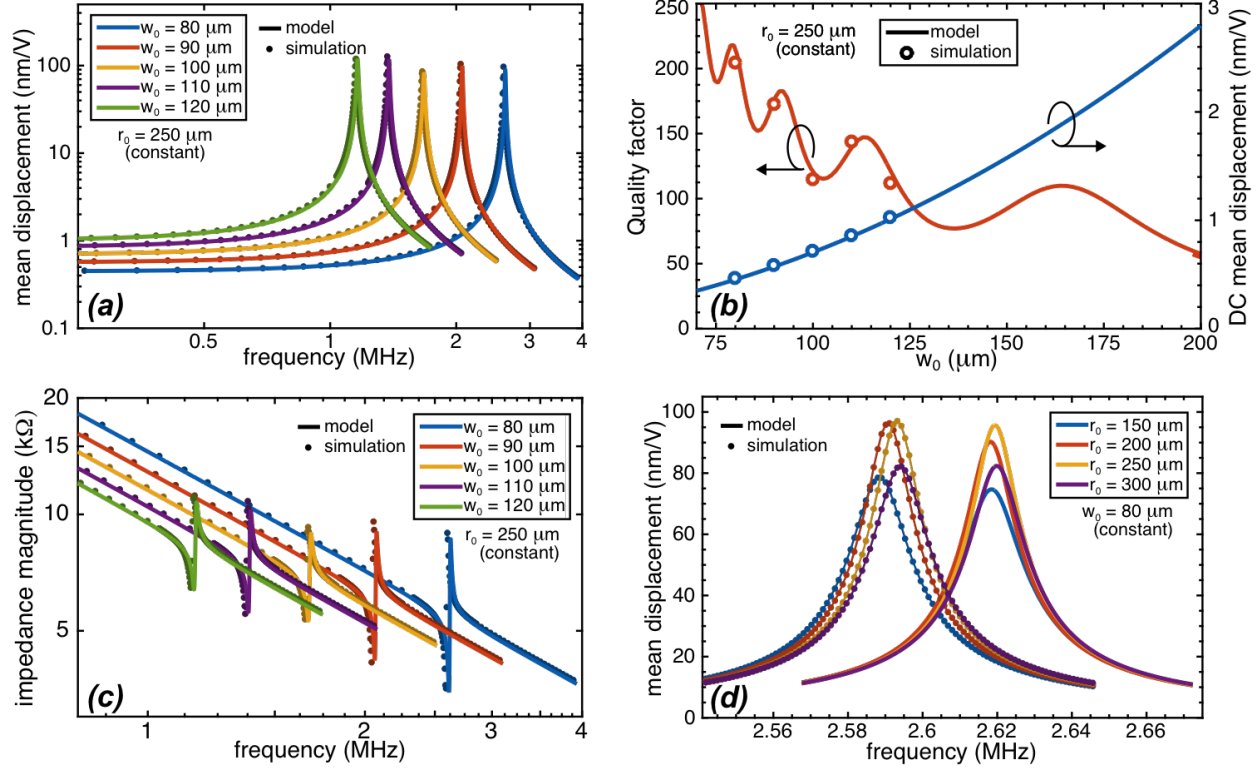
Figure 3.11: Comparison of air-coupled performance predicted by the equivalent circuit and FEA. (a) displacement frequency response for structures with fixed mean radius and various width, (b) quality factor and DC displacement versus width, with simulated values extracted from (a), (c) electrical input impedance magnitude for designs with fixed mean radius and various width, (d) displacement near resonance for PMUT with fixed width and various mean radii.

can be neglected. In this case, f_0 may be approximated as the undamped value according to (3.62), and the quality factor may be approximated as shown in Figure 3.11(b) as

$$Q = \sqrt{m_m k_m}/R_a, \tag{3.74}$$

where R_a is evaluated at f_0.

In actual air-coupled devices, the acoustic resistance may not represent the largest energy loss mechanism, so if it is desired to predict performance in practice, the denominator of (3.74) should be replaced with an equivalent total resistance, which is typically found empirically (e.g., [50]). Combined with the previously mentioned fact that we typically desire a large acoustic resistance, (3.74) highlights the important and perhaps non-intuitive idea that PMUTs benefit from a low Q, as long as it is for the right reasons. Since acoustic radiation is actually an energy loss mechanism from the point of view of the PMUT (energy is transferred from the diaphragm to the acoustic medium), if the Q is low because R_a is high, it indicates that the PMUT is an efficient acoustic radiator. This is however not the case if the Q is low because another damping mechanism is

strong, which would not indicate an acoustically efficient design, but might still be appealing due to the decreasing ringing in the PMUT.

In regards to the displacement, the acoustic impedance decays to zero at low frequencies, allowing w_{DC} to be calculated as

$$w_{DC} = \eta V / k_m. \tag{3.75}$$

w_{DC}, which is proportional to w_0^2 and is insensitive to r_0, is a simple yet powerful optimization metric for PMUTs as it is the product of the displacement at resonance w_{res} and the fractional bandwidth $BW_f = 1/Q$ (i.e., $w_{DC} = w_{res}BW_f$), which are typically both desired to be maximized. As shown in Figure 3.11(b), the simulated and modeled values of w_{DC} agree to within 1.2% for all simulated w_0, confirming the accuracy of the equivalent circuit. Furthermore, it is interesting to note that the resonant displacement is not a strong function of w_0 due to the roughly opposing trends in Q and w_{DC} with respect to w_0.

To validate the circuit model as an electrical network, the simulated input impedance is found by integrating the current density over the top electrode to find the total current, and is compared with (3.18) in Figure 3.11(c). The displacement frequency responses of Figure 3.11(a) exhibit low and high-frequency values that match nearly identically between simulation and circuit modeling, with a roughly 0.4% overestimate in both resonance and antiresonance frequencies is observed.

Figure 3.11(d) displays the impact of r_0 on the frequency response by comparing devices with constant $w_0 = 80\,\mu\text{m}$. While the minor discrepancy in resonance frequency is again apparent, both the circuit model and simulation predict that the resonance frequency changes by less than 0.5% as r_0 is doubled from 150 to $300\,\mu\text{m}$, while the resonance displacement changes by less than 25%.

Together, the preceding results have interesting implications for the design methods and versatility of ring-shaped PMUTs. While tuning of the film stack is often constrained by manufacturing, w_0 may be chosen to set f_0 at the frequency dictated by the application. Due to its lack of influence on f_0, r_0 may then be freely selected to tailor other properties, such as volume velocity, bandwidth, or aperture size. The independence of f_0 and r_0 also suggests that concentric ring-shaped PMUTs with equal widths may be arranged in high fill-factor arrays that generate large pressures with all devices resonating at the same frequency.

3.4.3 Liquid-coupled Performance

Many applications of PMUTs call for liquid-coupled operation, in which case the acoustic impedance plays a larger role in the device performance and therefore merits further examination. To this end, similar parameter sweeps to those in the previous section are performed with Fluorinert FC-70
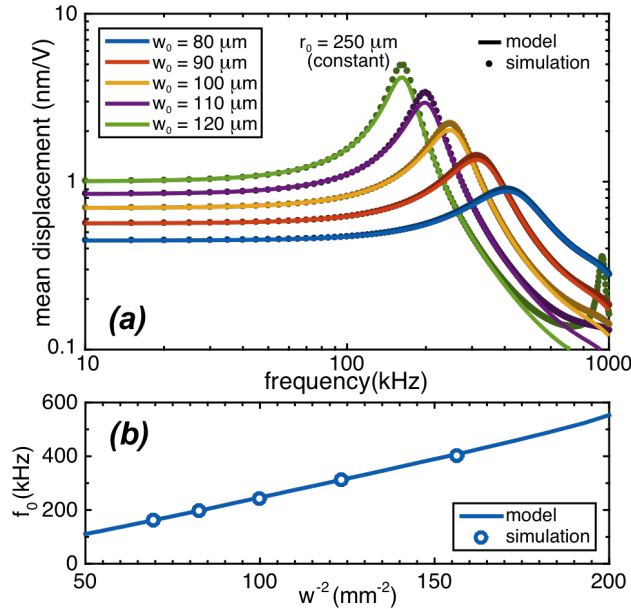
Figure 3.12: Comparison of simulated and modeled (a) displacement frequency responses and (b) resonance frequencies of ring-shaped PMUTs in FC-70 with equal mean radius and various widths.

($c_a = 685 \, \text{m/s}$, $\rho_a = 1930 \, \text{kg/m}^3$) as the acoustic medium, which is commonly used in PMUT testing because it is electrically insulating and has an acoustic impedance close to that of water.

Analogous to Figure 3.11(a), Figure 3.12(a) presents the effect of changing w_0 at constant $r_0 = 250 \, \mu\text{m}$. The liquid-coupled and air-coupled performances are almost identical at low frequencies because the mechano-acoustic impedance Z_{ma} is dominated by k_m which does not depend on the acoustic medium, however, at higher frequencies several changes are notable: (1) the resonance frequency of the device in liquid is about 6-7 times lower than that in air due to the increased acoustic mass loading, however, as shown in Figure 3.12(b), the relation $f_0 \propto w^{-2}$ still holds; (2) the resonant displacement increases with the ring width, and is reduced by more than $10\times$ compared to air operation due to the increased acoustic radiation resistance; (3) an increase in BW_f, again caused by increased R_a; and (4) a divergence between the modeled and simulated displacements at higher frequencies due to the onset of higher order vibration modes. These higher order vibration modes would be present in the air-coupled results as well if the simulations had extended to sufficiently high frequencies, and are of little concern because the developed model is focused on PMUTs operating near their primary resonance. The wider bandwidth of liquid-coupled ring-shaped PMUTs dictates that the acoustic impedance be treated as a frequency-dependent circuit element, and combined with the lack of a closed-form expression of Z_a, precludes accurate approximations for most performance metrics.

3.5 Extensions of the Equivalent Circuit Model

While the derivation presented here is lengthy for the sake of thoroughness, the method provides an easy framework for new PMUT designs to be modeled. For instance, bimorph PMUTs could be modeled by simply changing the integration limits in (3.44) and (3.45) to reflect that the electric field is nonzero in both layers of the diaphragm and resulting in changes to η and C_0; additional top electrodes could be modeled as an additional transformer connected in series with the same mechanical and acoustical elements; and new PMUT geometries could be modeled by assuming their modeshape and using it to re-evaluate (3.43)-(3.45) and the acoustic impedance. To display the utility of the model and compare PMUT designs, we will briefly cover two didactic cases here: (1) the on-axis pressure output from a ring-shaped PMUT, (2) the equivalent circuit model of circular PMUTs.

3.5.1 On-axis Pressure Output

Due to the annular structure of the ring-shaped PMUT, the maximum acoustic pressure generated in the surrounding medium lies along the axis of symmetry. This so-called on-axis pressure is useful for characterizing ultrasonic transducers, and can determined once the velocity distribution is known through the Rayleigh integral. By generalizing (3.68) to include any z-coordinate, we find

$$p_a(r, z) = j\frac{\rho_a c_a k}{2\pi} \int_0^{2\pi} \int_a^b u_N(r')\frac{e^{-jkR}}{R}r'\,dr'\,d\phi', \tag{3.76}$$

where all coordinates are labeled in Figure 3.13(a), and $R^2 = r^2 + z^2 + r'^2 - 2rr'\cos\phi'$ is the distance from the differential area on the transducer to the field point. We may then simplify by only considering points along the symmetry axis $r = 0$ to express the axial pressure p_{ax} as

$$p_{ax}(z) = j\rho_a c_a k u_m \int_{R_1}^{R_2} \phi(R)e^{-jkR}\,dR, \tag{3.77}$$

where the integration limits are given by $R_1 = \sqrt{a^2 + z^2}$ and $R_2 = \sqrt{b^2 + z^2}$. While there is no general closed-form solution to (3.77), we may either use numerical evaluation or simplify by treating the transducer as a piston vibrator, wherein $\phi(R)$=1. In this case, the axial pressure simplifies to

$$p_{ax}(z) = \rho c u_m\left[e^{-jk\sqrt{a^2+z^2}} - e^{-jk\sqrt{b^2+z^2}}\right]. \tag{3.78}$$

A comparison of the two methods, i.e. (3.78) and numerical integration of (3.77) with our assumed modeshape, is provided in Figure 3.13(b) for a device with r_0=250 μm and w_0=100 μm in water ($c_a = 1500\,\text{m/s}$, $\rho_a = 1000\,\text{kg/m}^3$). At frequencies below 5 MHz, the two methods agree
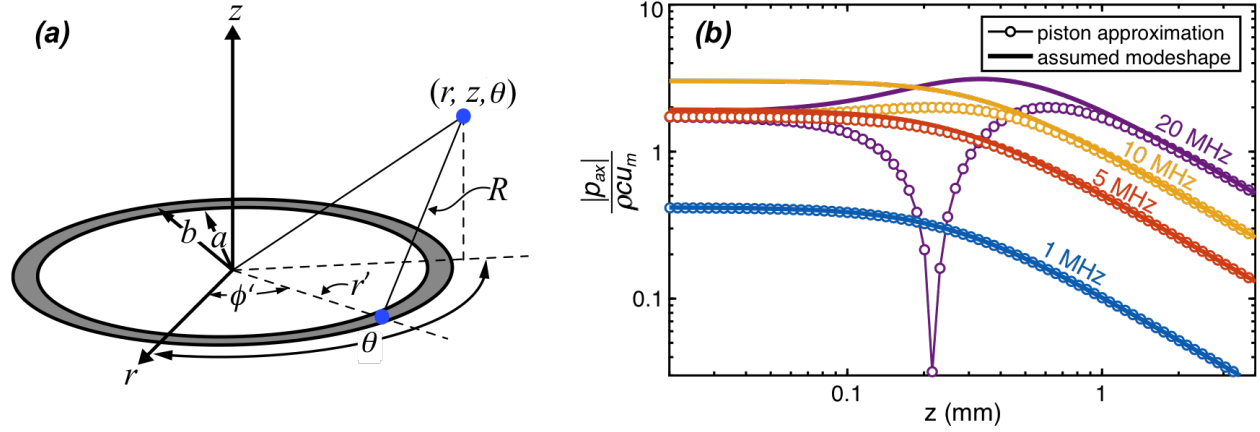
Figure 3.13: (a) Geometry and coordinates used in (3.76); (b) comparison between the piston approximation of (3.78) and numerical integration of (3.77) using the assumed modeshape, showing strong agreement below 5 MHz and in the far-field at all frequencies.

for all z. On the other hand, as shown at 20 MHz, the piston approximation does not model the pressure well within the near-field where $z < A_v/\pi\lambda$. Nonetheless, the piston approximation is valid within the far-field and provides sufficiently accurate results while having additional appeal due to its simplicity.

3.5.2 Circular PMUT Model

In order to compare the ring-shaped PMUT to the standard circular PMUT, the modeling approach presented in this chapter can easily be adapted to derive an equivalent circuit model for the latter. In doing so, we utilize the commonly reported approximate modeshape of a circular plate ϕ_c [25]:

$$\phi_c(r) = 3(1 - (r/a)^2)^2, \tag{3.79}$$

where a is the radius of the circular PMUT, and the factor of 3 is introduced to reflect that the average value of ϕ_c over the vibrating area should be 1. The mechanical mass can be evaluated by simply changing the integration limits on (3.31), resulting in $m_m = 1.8\rho_s\pi a^2$. By similarly changing the integration limits and modeshape in (3.48), the mechanical stiffness is found as $k_m = 192\pi D_b/a^2$. With the mass and stiffness defined, the unloaded resonance frequency can be solved for as

$$f_0 = \frac{1}{2\pi}\sqrt{\frac{k_m}{m_m}} = \frac{1.644}{a^2}\sqrt{\frac{D_b}{\rho_s}}. \tag{3.80}$$

By comparing to (3.62), we find that frequency-matching between circular and ring-shaped PMUTs with the same film stack is achieved when $w_0 = 1.48a$, which is aligned with the findings of Chapter 2. Interestingly, this also reveals that ring-shaped PMUTs necessarily have a larger vibrating

area than their circular counterparts when the two designs are frequency-matched. It is similarly only required to change the integration limits in (3.53), and the area in (3.59), to determine the turns ratio and clamped capacitance as $\eta = 6\pi e_{31,\text{f}} Z_p$ and $C_0 = (1 - k_{31}^2)\varepsilon_{33}^T \pi a^2/2h_p$, respectively, where an areal electrode coverage of 50% has been assumed. It is worth noting that the equivalent circuit defined by these parameters is equivalent to that of previous reports (e.g., [36],[50]). Furthermore, one of the most common ways of comparing PMUTs with different designs is by examining the effective electromechanical coupling coefficient k_e^2, which can be expressed in terms of the turns ratio, mechanical stiffness, and electrical capacitance as [58]

$$k_e^2 = \frac{\eta^2 k_m^{-1}}{\eta^2 k_m^{-1} + C_0} \approx \frac{\eta^2 k_m^{-1}}{C_0}, \qquad (3.81)$$

where the final approximation reflects the assumption that the coupling coefficient is small. Invoking this assumption and plugging in for the lumped parameters allows us to relate the coupling coefficient for the ring $k_{e,ring}^2$ to that of the circle $k_{e,circ}^2$ by

$$k_{e,ring}^2 = 1.33\ k_{e,circ}^2, \qquad (3.82)$$

which reveals that the ring-shaped architecture enhances effective electromechanical coupling by 33% when compared to the standard PMUT design.

3.6 Conclusion

In this chapter, an equivalent circuit model is presented for ring-shaped PMUTs. As a new PMUT architecture, one of the main goals of the equivalent circuit model is to gain understanding and intuition on the device performance and its dependencies on the design parameters. Results indicate that optimal device performance is achieved with a ring-shaped top electrode that is centered on the diaphragm with a 57% areal coverage, and that regardless of device dimensions or acoustic media, ring-shaped PMUTs exhibit a resonance with $f_0 \propto w_0^{-2}$ and a DC displacement $w_{DC} \propto w_0^2$, neither of which are affected appreciably by the mean radius r_0. On the other hand, overall device performance may differ significantly when a device is operated in air versus in liquid. For example, air-coupled ring-shaped PMUTs exhibit a single, relatively high-Q peak near resonance, f_0 may be accurately determined using the undamped natural frequency, and Q may be well-approximated with a standard formula and evaluating R_a at f_0. Conversely, the acoustic resistance and reactance play more significant roles in the overall dynamics of liquid-coupled devices because they are comparable in magnitude to the mechanical impedance. The increased damping and mass-loading significantly lowers the resonance frequency, decreases the amplitude of motion at resonance, and increases the bandwidth.

The equivalent circuit is obtained based on an assumed-mode modeling approach that is simple to implement and shown to correlate well with simulations for single-electrode unimorph devices

with a wide range of dimensions and at frequencies below or near that of the first resonance, which is the case in practice for most PMUTs. It is, nonetheless, envisioned that this model can be applied to more complex realizations of ring-shaped PMUTs such as bimorph or multiple-electrode designs with only minor adaptations. Furthermore, the model developed here should facilitate comparisons with other MUTs, and elucidate the benefits of the ring-shaped device. For example, ring-shaped PMUTs are predicted to exhibit 33% stronger electromechanical coupling than typical circular PMUTs, and the insensitivity of f_0 to r_0 is of critical importance for the design of concentric arrays of ring-shaped PMUTs for pulse-echo operation or high pressure output.

Chapter 4

Broadband Ring-shaped PMUTs Based on an Acoustically Induced Resonance

In this chapter, the principle and broadband operation of ring-shaped piezoelectric micromachined ultrasonic transducers (PMUTs) in liquid-coupled operation is reported on. Specifically, fabricated devices are measured to have a velocity bandwidth of up to 160%, which is more than 60% greater than the highest bandwidth of any reported standalone PMUT and is tunable by altering device dimensions. This broadband performance is due to a resonance peak that is induced by acoustic interactions with the surrounding medium and occurs due to the ring-shaped geometry. Such an increased and tunable bandwidth should improve the axial resolution and efficiency of PMUTs, and possibly enable new applications such as harmonic imaging.

4.1 Background

Due to the success of numerous recent research efforts, micromachined ultrasonic transducers (MUTs) continue to gain traction as a replacement for conventional ultrasound systems and as a platform technology in new fields, such as fingerprint scanning and photoacoustic imaging [72], [25], [14]. Within the field of MUTs, capacitive transducers (CMUT) are able to achieve remarkably high bandwidths, even exceeding 100%, due to the ability to fabricate CMUTs with extremely thin diaphragms such that the mechanical impedance is considerably lower than that of liquid acoustic media [21]. In contrast, while offering critical advantages over their capacitive counterparts, PMUTs remain limited by their low bandwidth; values of 26% and 43% were reported in [73] and [74], respectively, which are typical for liquid-coupled devices. It would be strongly favorable to achieve wider bandwidths, however, as the axial resolution of MUTs operating in pulse-echo mode (e.g., for imaging applications) is dictated by the bandwidth, and MUTs with narrow bandwidths have inherently inefficient mechanoacoustic transduction. Low-bandwidth devices also

preclude many applications, such as those involving chirp waveforms or harmonic responses.

As such, the topic of increasing the bandwidth of PMUTs has garnered much attention in recent years. For example, a pressure bandwidth of 55% was achieved with an array of individual PMUTs with different sizes and resonance frequencies, which behaved similarly to mechanically coupled resonators [24]. Such behavior has also been observed in arrays of PMUTs with equal sizes, as a 167% pressure bandwidth was reported in [25], but array implementations with burdensome wafer footprints are required nonetheless. Conversely, a rectangular PMUT with multiple overlapping resonance modes showed a 97% pressure bandwidth, which is the highest reported value for a standalone device [22]. This increased bandwidth was based on acoustically inefficient higher-order vibration modes that have low volume velocities, however, and also requires very long PMUTs in order to achieve sufficiently overlapping modes [23].

In contrast to the aforementioned works, we herein report on the ring-shaped PMUT as a broadband device. Through Finite Element Analysis (FEA) simulations in Comsol Multiphysics, the PMUT is shown to have two distinct resonances: the primary resonance, which has been covered in Chapters 2 and 3, and a newfound acoustically induced resonance. The acoustic impedance is used to show that the latter of the resonances is caused by the acoustic load reaching a minimum at a specific frequency, which is defined by the device size and surrounding medium. This is substantiated by the testing of aluminum nitride (AlN) ring-shaped PMUTs in different liquid mediums, showing a bandwidth of up to 160%, which is more than 60% greater than the highest bandwidth of any reported PMUT and is tunable by altering device dimensions or liquids. Furthermore, this unprecedented bandwidth is achieved by utilizing only the acoustically efficient fundamental vibration mode and without the need for large arrays.

4.2 Concept and Operating Principle

4.2.1 PMUT Response in Air and Liquid

In the previous two chapters, we have reported on the performance of ring-shaped PMUTs operated in air, however the corresponding liquid-coupled performance has only been briefly investigated. To this end, FEA simulations, which were previously shown to correlate well with observed device performance, were performed with both air and liquid environments for comparison purposes. The device structure is again the same as in Chapters 2 and 3, wherein both the active and structural layers are AlN with thicknesses h_T and h_B, respectively. Figure 4.1 shows the results of these simulations in terms of the velocity frequency response for devices with h_T=0.8 μm, h_B=1 μm, w_0=100 μm, and various r_0 with (a) air (ρ_a=1.2 kg/m^3, c_a=343 m/s) and (b) Fluorinert FC-84 (ρ_a=1730 kg/m^3, c_a=543 m/s) as the acoustic medium, where ρ_a and c_a are the respective density
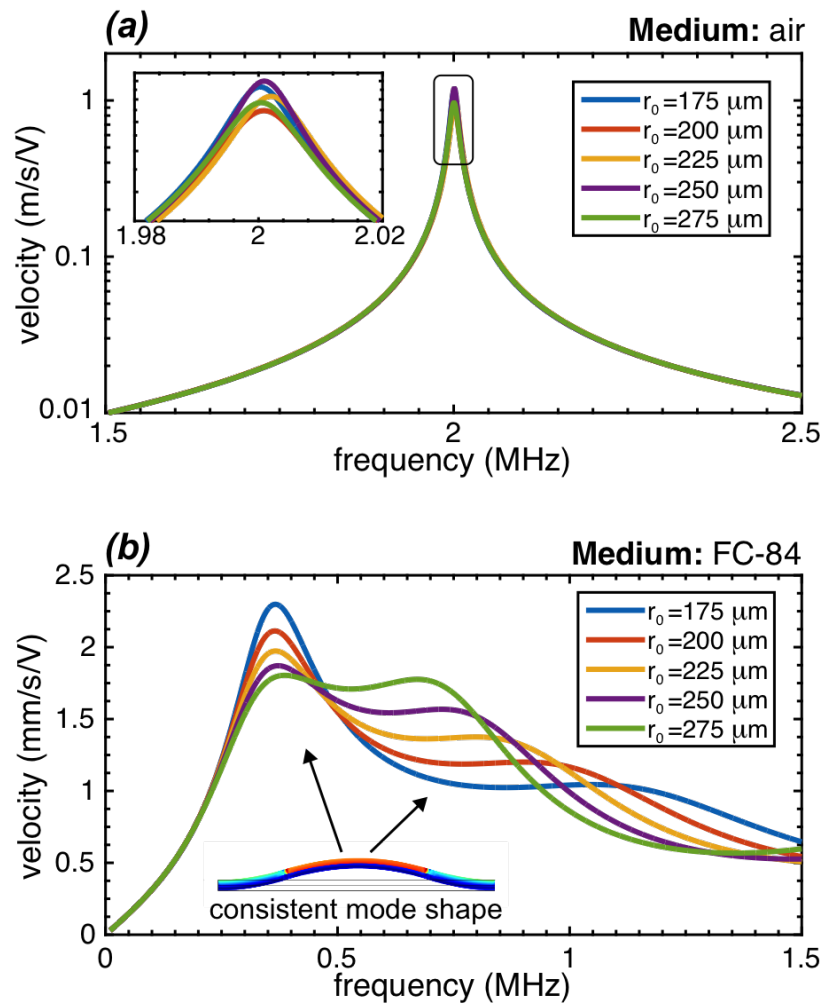
Figure 4.1: Simulated velocity frequency response of ring-shaped PMUTs with w_0=100 μm and varying r_0 in (a) air and (b) liquid (FC-84). Liquid-coupled devices show two distinct resonances; both have the same mode shape, and the second is more pronounced when frequency-matched with the first.

and sound speed.

Air-coupled ring-shaped PMUTs (Figure 4.1(a)) typically exhibit resonance frequencies and vibration amplitudes that do not significantly change as r_0 is varied at fixed w_0, and the devices exhibit a fairly narrow bandwidth ($\sim$1%). This behavior has been observed and discussed thoroughly in Chapters 2 and 3. As shown in Figure 4.1(b), however, the behavior of ring-shaped PMUTs can differ significantly when operated in liquid as compared to in air. Paralleling the effects observed in standard MUT architectures, the additional mass and resistive loading provided by the liquid acoustic medium result in a downshift in resonance frequency and decrease in resonance amplitude,

respectively. In contrast to typical PMUTs, however, appropriately designed ring-shaped PMUTs can exhibit two distinct resonance peaks; the frequency of the first (primary) resonance is largely insensitive to r_0 and is analogous to the resonance seen in air-coupled ring-shaped PMUTs, while the second resonance decreases in frequency with r_0 and is more pronounced when frequency-matched with the first. Furthermore, simulations indicate that the mode shapes of both resonances are nearly identical as shown in the inset of Figure 4.1(b), implying that the second resonance is not caused by the onset of a higher-order vibration mode, as is often the case for transducers that exhibit multiple resonances. This is further substantiated by the fact that the equivalent circuit model developed in Chapter 3, which only models the effects of the fundamental vibration mode, predicts nearly identical velocity frequency responses that show the same phenomenon. Instead, the second resonance is in fact caused by interactions with the acoustic medium.

4.2.2 Explanation of the Acoustic Resonance

As a PMUT vibrates in the presence of an acoustic medium, it generates a pressure that imparts a force back on the diaphragm that affects the dynamics of the device. This effect can be modeled using the acoustic impedance Z_a, which we derived as the ratio between the equivalent force applied on the PMUT by the acoustic medium F_a and the average PMUT velocity u_m (i.e., $Z_a = F_a/u_m$) in Chapter 3.3.4. In order to demonstrate that acoustic interactions are the cause of the second resonance observed in ring-shaped PMUTs, we begin by presenting numerical calculations of the dimensionless acoustic impedance magnitude $|z_a| = |Z_a|/\rho_a c_a A_v$, where $A_v = 2\pi r_0 w_0$ is the vibrating diaphragm area, in Figure 4.2(a). Here, it is apparent that there are distinct frequencies at which the impedance, and therefore the acoustic loading, is minimized; the first local minimum in z_a occurs at about f=1.06 MHz for r_0=175 μm, and decreases in frequency with increasing r_0. Such pronounced trends in the acoustic impedance are unique to the ring-shaped design and play a significant role in the behavior of ring-shaped PMUTs. As shown in Figure 4.2(b), the frequency of the first local minimum in the acoustic impedance occurs at about $kr_0 = 2.1$, where $k = 2\pi f/c_a$ is the acoustic wavenumber, and shows the same trend and is highly correlated with the frequency of the second resonance from Figure 4.1(b). Indeed, at frequencies in which the acoustic loading is significantly reduced, the PMUT is able to achieve higher velocities, which is manifested in the frequency response as an additional resonance peak. With this understanding, the two resonances can be conceptualized using lumped parameter modeling concepts from Chapter 3: the second resonance is caused my a minimum in $|z_a|$, and the first resonance occurs roughly at frequencies where the imaginary component of the mechano-acoustic impedance is 0 (i.e., where the mechanical stiffness is cancelled by the acoustic and mechanical masses).

Understanding the cause of the second resonance has powerful implications for the design and utility of ring-shaped PMUTs. Firstly, it allows for recognition of the independent effects of the device geometry parameters: the film stack and w_0 determine the primary resonance frequency, and r_0 sets the frequency of the second resonance. This facilitates tailored designs and enables
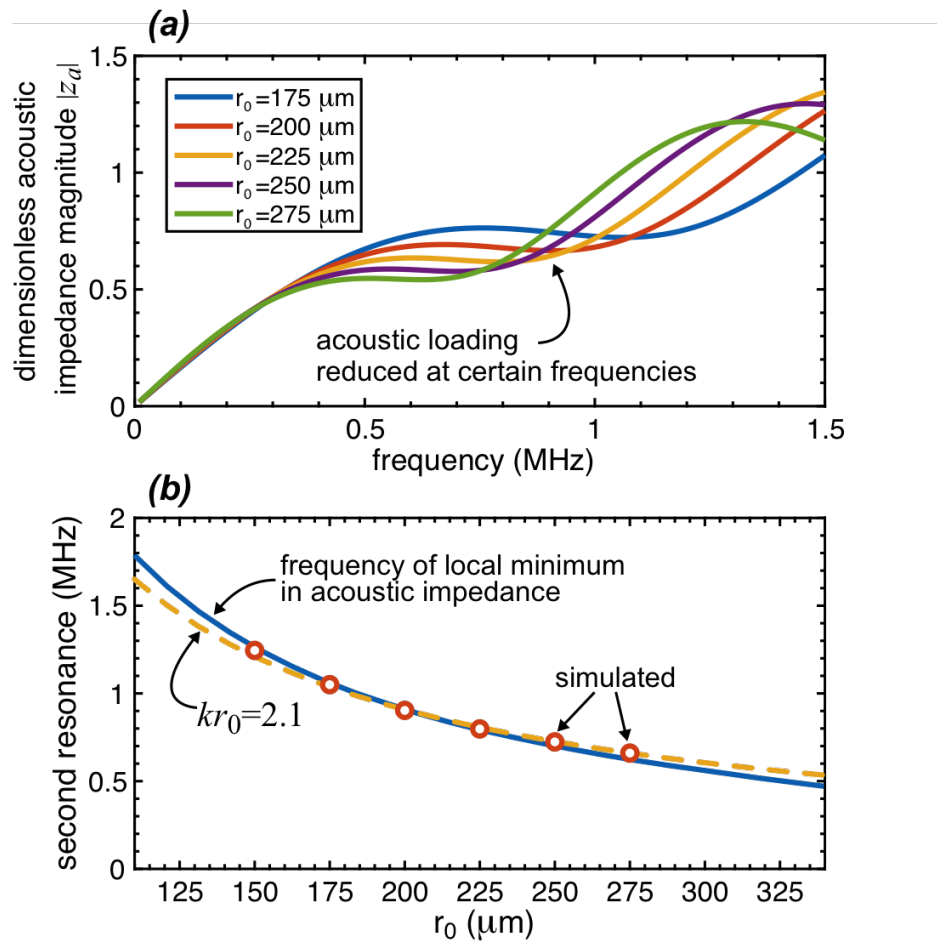
Figure 4.2: (a) normalized acoustic impedance of a ring-shaped PMUT in FC-84, showing reduced loading at specific frequencies; (b) comparison of simulated and predicted second resonance frequencies, evidencing acoustic interactions as the cause of the second resonance.

the targeting of a range of bandwidths and/or amplitudes. On a different note, because the second resonance is induced by interactions with the acoustic medium, it is also an indicator of strong coupling and efficient mechanoacoustic transduction, which is a desirable property of PMUTs.

4.3   Velocity Measurements

In order to verify that ring-shaped PMUTs can exhibit broadband and multi-resonance behavior, devices that were fabricated in the same process covered in Chapter 2.2 were experimentally tested, with an optical image of the ring-shaped PMUTs used in testing is provided in Figure 4.3(a). The

PMUT diaphragm is again composed of an AlN (1000 nm)/Mo (130 nm)/AlN (800 nm)/Mo (130 nm) film stack; the device chip contains 8 ring-shaped PMUTs with a designed width of w_0=90 µm and various r_0 between 150 and 300 µm, and is mounted on a custom PCB for electrical connections. For performance characterization, the frequency response of the devices is measured using a laser Doppler vibrometer (LDV, OFV-5000, Polytec Inc.) as shown in Figure 4.3(b), where the velocity is measured at the center of the vibrating diaphragm (i.e., at r_0). In order to examine the effect of the acoustic medium on the frequency response, the test fixture is filled with various liquid acoustic media.

Figure 4.4 displays the results of the LDV measurements of the same devices in both Fluorinert (a) FC-40 (ρ_a=1190 kg/m^3, c_a=684 m/s) and (b) FC-84. The frequency response curves have been smoothed by convolving the raw data with a Gaussian (std. dev. = 20 kHz) in order to reduce the effects of the $\lambda/4$ spurious resonances that occur due to acoustic echoes from the surface liquid/air interface, then normalized to a maximum value of 1 (0 dB). As expected, the ring-shaped PMUTs exhibit a primary resonance that is independent of mean radius in both acoustic media. In contrast, the fractional bandwidth, defined as the -6 dB frequency range divided by the resonance (maximum velocity) frequency (i.e., $BW_\text{f} = \Delta f / f_0$), varies significantly according to the acoustic medium and device size. When the acoustic medium is FC-40, BW_f varies between 57% and 68% for the smallest and largest ring-shaped PMUT, respectively, as shown in Figure 4.4(a). While the normalized center velocity at frequencies above the first resonance does increase with r_0, the BW_f does not drastically change because the acoustic resonance occurs at $f >$780 kHz for all r_0, thus the two resonances are not sufficiently matched to have a pronounced effect.

Conversely, the reduced sound speed in FC-84 lowers the acoustic resonance frequency, such that it is expected to occur at at f=620 kHz for r_0=300 µm. This matches well with measurements in Figure 4.4(b), where a broad secondary peak near 600 kHz is present for r_0=300 µm. Indeed, with FC-84 as the acoustic medium, the ring-shaped PMUTs displayed a bandwidth that is tunable from 65% to as high as 160%, which is a marked improvement over the previously reported maximum bandwidth for standalone PMUTs of 97% [22].

4.4 Pressure Measurements

To further show the ability of the acoustic impedance to impact the performance of ring-shaped PMUTs, the pressure output from the transducer was also measured. For this task, since the pressure from a single PMUT is relatively small, ring-shaped PMUTs with higher efficiency were used to achieve sufficient signal-to-noise ratio (SNR) in the measurements. To this end, ring-shaped PMUTs with a dual-electrode bimorph (DEB) architecture were fabricated; this design is covered more thoroughly in Chapter 5.2 along with its fabrication, however it can be described concisely as having the same overall structure and only slightly different film stack from the unimorph design
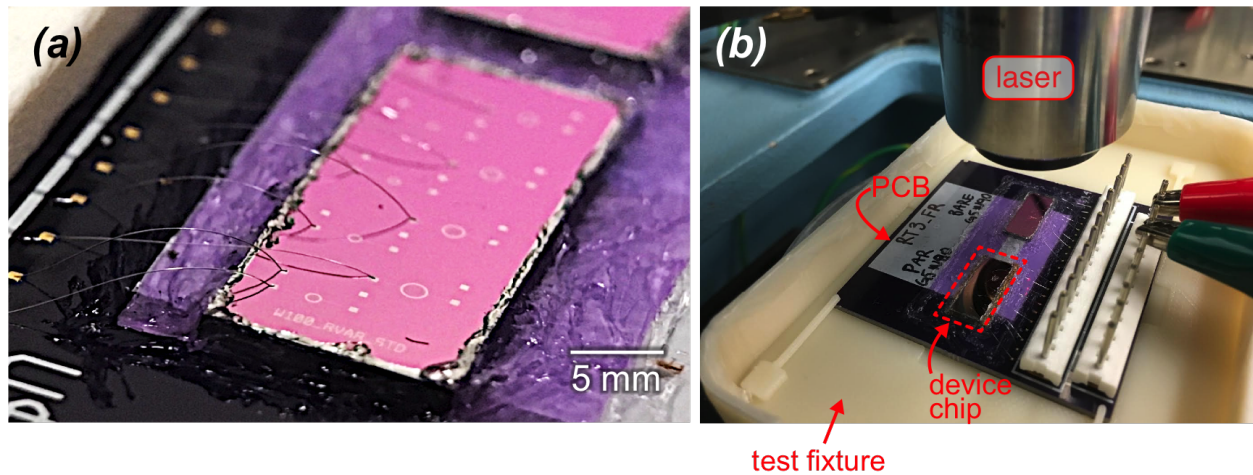
Figure 4.3: (a) optical image of the ring-shaped PMUT chip with the devices used for testing mounted on a PCB, and (b) test setup used to measure the frequency response with LDV. The test fixture is filled with different liquids in order to examine their effect on the frequency response.
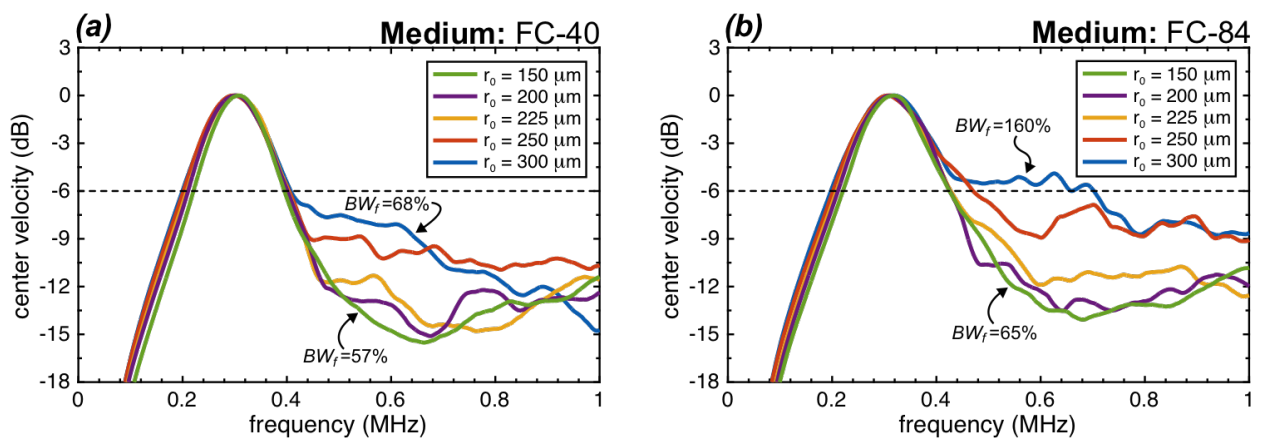
Figure 4.4: Measured frequency response of ring-shaped PMUTs in (a) FC-40 and (b) FC-84. FC-40 has a higher sound speed, so the acoustic resonance is at higher frequency and not matched to the first resonance, and we see only minor changes as r_0 is increased. In FC-84, however, the acoustic resonance is at 620 kHz for r_0=300 μm, and therefore has a strong effect. In this case, a bandwidth of 160% is achieved
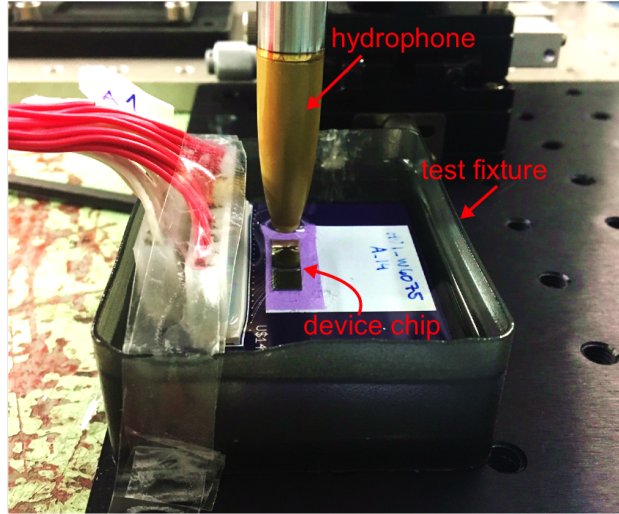
Figure 4.5: Test setup used to measure the pressure-based transmit sensitivity of the fabricated ring-shaped PMUTs. The test fixture both holds the PMUTs in place and acts as a miniature acoustic tank, which is filled with mineral oil allowing the output pressure to be measured by hydrophone.

used up to this point, however it achieves $4\times$ the displacement per volt by increasing the amount of active piezoelectric in the diaphragm. In this case, the fabricated devices have a film stack with two 830 nm active layers of AlN, three 130 nm layers of Mo as electrodes, and a 175 nm seed layer of AlN, with a designed width w_0=60 μm, and r_0 varying between 150 and 450 μm.

For testing, the PMUTs are placed in a text fixture and immersed in mineral oil (ρ_a=882 kg/m^3, c_a=1483 m/s) as shown in Figure 4.5. The PMUTs are driven by an arbitrary waveform generator (AWG, ArbStudio 1104, Teledyne LeCroy, USA) and the acoustic pressure is measured with a hydrophone (HGL-0200, Onda Corp., USA) connected to a preamplifier (AH-2010, Onda Corp., USA) that is mounted on an x-y-z stage with manual micrometer control. The hydrophone is verified by the manufacturer to not disturb acoustic fields and is aligned at a distance of z=7 mm by changing x and y in order to maximize the amplitude of the hydrophone reading and using the time of flight to determine z-distance.

In order to determine the frequency-dependent transmit (Tx) sensitivity of the PMUT S_{Tx}, which we define as the output pressure per input volt, each transducer is driven with a 4 MHz, 12 V$_{pp}$, 1 cycle square wave, such that the hydrophone receives a short pressure pulse with all echoes from nearby surfaces sufficiently separated in time that they do not impact measurements. To evaluate S_{Tx}, we can take the fast Fourier transform (FFT) of this echo signal, however, we must also take the effect of the driving waveform into account; for instance, a PMUT with an infinite Tx bandwidth will exactly reproduce a 4 MHz square wave pulse, which does not have a flat frequency spectrum. Furthermore, the hydrophone has a frequency-dependent receive (Rx)

sensitivity H_{Rx}, such that the frequency spectrum of the pulse as measured with the hydrophone is a convolution of the three relevant impulse responses:

$$RX(j\omega) = S_{Tx}(j\omega) \, H_{Rx}(j\omega) \, TX(j\omega) \tag{4.1}$$

where RX and TX are the frequency spectra of the received and driving waveforms, respectively. Therefore, in order to get the transmit sensitivity of each PMUT, we divide the hydrophone sensitivity and transmit waveform spectrum out from the FFT of the received pulse.

The results of this process are shown in Figure 4.6. The normalized time-domain signal of the pressure pulses measured from three ring-shaped PMUTs with r_0 from 150 to 300 µm are shown in Figure 4.6(a), where significantly more ringing is observed for r_0=225 µm than for either 150 or 300 µm. This increase in ringing is typically a sign of a lower bandwidth, and is the fundamental reason that wide bandwidths are important for many applications. Furthermore, the Tx sensitivity as calculated using the process outlined above for the three waveforms in (a) along with two others are displayed as black curves in Figures 4.6(b)-(f). The corresponding red curves are the Tx sensitivities as determined using the equivalent circuit model developed in Chapter 3 in conjunction with the piston pressure approximation of (3.78) at z=7 mm, and show a strong agreement with the measured values. Interestingly, other than for the smallest ring-shaped PMUT with r_0=150 µm, all devices show multiple peaks in their measured S_{Tx}, which occur at frequencies that are well-predicted by the equivalent circuit and are due to the acoustic impedance that fluctuates with frequency and is again unique to the ring-shaped geometry. Furthermore, the ringing observed in Figure 4.6(a) is directly tied to the relatively sharp 3 MHz peak in Figure 4.6(c), which has the narrowest of the measured fractional bandwidths at 65%. For this reason, it is important that PMUT designers looking to utilize ring-shaped geometries fully understand and account for the complex behavior incited by the acoustic medium; there is no obvious trend wherein increasing r_0 will result in an increase or decrease in bandwidth, as is the case for conventional MUTs where larger and thinner devices tend to produce wider bandwidths. In contrast, BW_f for r_0=150, 375, and 450 µm all exceed 100%, and r_0=450 µm displays the largest reported pressure bandwidth to date of 130%.

4.5 Conclusion

We have explored the ring-shaped PMUT as a broadband device with tunable performance. Two distinct resonances have been observed: the first is the well-understood resonance of the fundamental vibration mode, and the second is due to frequency-dependent acoustic loading. Owing to the fact that each resonance is affected by different geometric device parameters, one can readily select the proper device size to achieve the desired bandwidth for a given application. In fact, with an accordingly designed ring-shaped PMUT, testing shows that a velocity bandwidth as high as 160% is achievable, and analysis indicates that still wider bandwidths are feasible. As further shown by
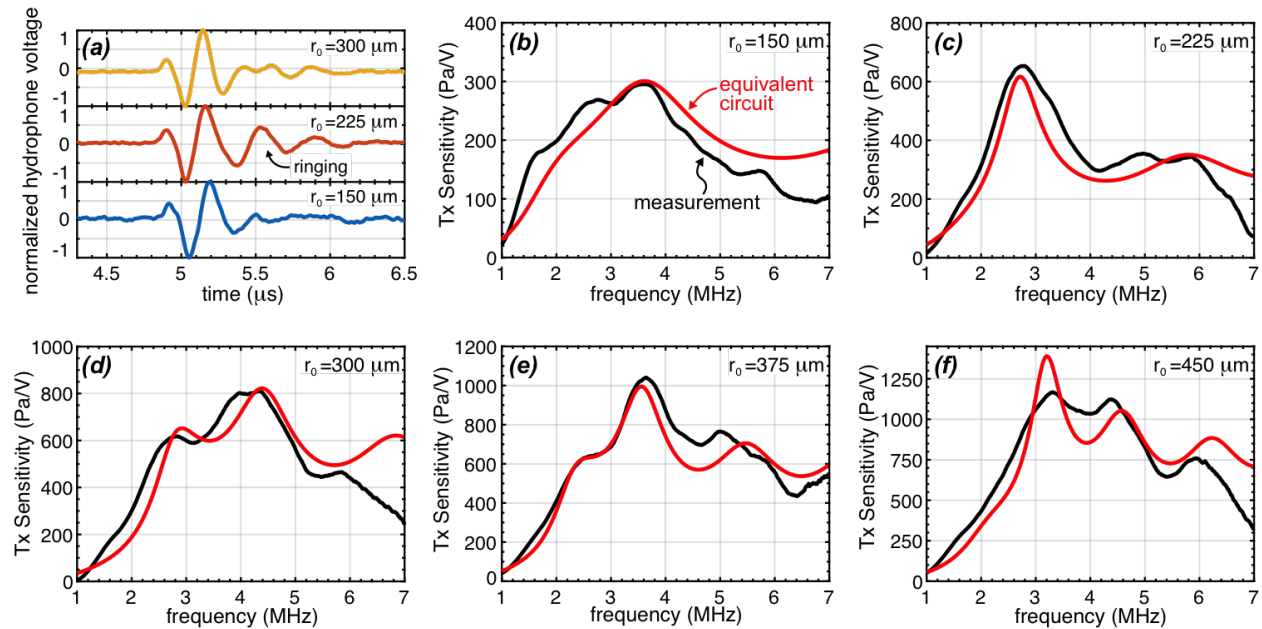
Figure 4.6: (a) Time-domain pressure pulses from ring-shaped PMUTs by hydrohpone, and (b)-(f) resulting frequency-domain transmit sensitivities (black curves) for five PMUTs with w_0=60 µm and varying r_0 with their corresponding predictions using the previously developed equivalent circuit model (red curves).

pressure measurements, this previously unobserved acoustic loading effect can produce substantial and complex changes in time-domain signals by affecting ringing and therefore the resolution of systems based on ring-shaped PMUTs, and it can do so in a way that might be unpredictable without an in-depth investigation.

Together, these findings indicate that ring-shaped PMUTs are a candidate to improve the efficiency and resolution of MUT-based systems in many fields. Furthermore, as high-performance MUT design is typically limited to material or mechanical-domain improvements, this work opens up a new direction to include acoustic considerations.

Chapter 5

A Single-chip Flow Sensor Based on Circular Bimorph PMUTs with Differential Readout Capabilities

In this chapter, we report the measurements of air flows for both magnitude and direction based on piezoelectric micromachined ultrasonic transducers (PMUTs) for the first time. The sensor operates in the pulse-echo mode to detect changes in flow with a measured sensitivity that is 286% of that for previously reported MUT-based flow meters, all while using less than 5V. The enhancement is a result of four unique sensor features: (1) the high-sensitivity bimorph structure of the fabricated PMUTs; (2) the spatial separation between the transmitter (Tx) and receiver (Rx) transducer elements; (3) the high directivity of the transmitted acoustic pulse; and (4) the differential readout. Owing to the single-chip design, our flow sensor is the first of its kind capable of measuring both flow direction and speed with high sensitivity. We will begin the chapter by covering the design of bimorph and dual-electrode bimorph (DEB) PMUTs and explain the cause of their respective 2 and $4\times$ performance increase comparing to standard designs. We will then move on to describe the architecture and operating principle of the flow sensor developed here through theoretical and finite element analysis. After presenting experimental verification of the sensor performance, the chapter will conclude with a discussion of the outlook and implications of this work.

5.1 Flow Sensing Background

In the past few decades, ultrasonic flow meters have seen a vastly expanding application space, including extensive use in manufacturing process monitoring, environmental monitoring, and feedback control of HVAC systems [75],[76]. In terms of sensing technology, ultrasound presents an appealing alternative to more conventional mechanical or pressure-based flow meters due to its

ease of use, fast measurement response, and reliability over a wide range of temperatures and flow speeds. Perhaps the most convincing case for ultrasonic flow sensing, however, is the low total-life cost, which is derived from the low sensor cost, along with easy installation, and minimal maintenance [75].

Ultrasonic flow sensors have traditionally employed bulk piezoelectric transduction elements that vibrate in the thickness mode in order to transmit or receive ultrasound signals. Such transducers tend not only to be acoustically inefficient, which necessitates the use of matching layers that increase system complexity and introduce burdensome production costs [77], but can also be difficult to manufacture with small form-factors in order to measure flow in tight spaces. In contrast, micromachined ultrasonic transducers (MUTs) are an emerging alternative technology that, due to numerous recent research efforts, now offer benefits over bulk piezoelectrics including enhanced acoustic coupling with air or other gases, cost-effective batch fabrication, easy integration with CMOS circuitry, miniature size, and design flexibility [78],[79].

Despite the prospect of these apparent advantages, MUT-based flow sensing has not yet been thoroughly explored. In [80], two different capacitive MUT (CMUT) wind speed sensors were proposed. Operating in pulse-echo mode, wherein a transmitter (Tx) CMUT element launches an ultrasonic pulse into the air that is then reflected back to a receiver (Rx) CMUT, the time of flight (ToF) or amplitude of the reflected ultrasound is collected to measure the wind speed. While achieving a high level of accuracy, the system requires impractical high voltages (over 100 V DC and AC), suffers from a low ToF sensitivity of about 0.6 $\text{ns}/(\text{ms}^{-1})^2$ that would require complex circuitry to acquire reliable measurements in real-time, and has interwoven Tx and Rx elements, resulting in a low amplitude sensitivity of 5.9%/ms^{-1} and precluding any differentiation of flow direction. Here, the sensitivity is presented in units of percentage change in signal strength per flow velocity in order to facilitate comparisons between systems with different amplifier gains.

In contrast, we herein report on the first MUT-based, single-chip flow sensor capable of measuring both direction and speed of air flow. Using simplified analytical models and experimental testing, the novel sensor architecture is shown to derive its sensitivity most strongly from a highly directional acoustic beam pattern and spatially distinct transmitting and receiving elements. The sensor concept is tested using high-performance aluminum nitride bimorph PMUTs fabricated in a previous process [40] to achieve a high sensitivity of 16.9%/ms^{-1}, which is more than 180% higher than that of previously reported MUT-based air flow sensors.

5.2 Dual-electrode Bimorph (DEB) PMUTs

The dual-electrode bimorph (DEB) PMUT is a high-performance design first developed and demonstrated by Akhbari *et al.* ([25], [40]) that is able to achieve up to 4× the sensitivity of typical

PMUTs in either transmit mode in terms of displacement per volt, or in receive mode as volts or amperes per pascal. While this structure has been the topic of previous works, we present here an intuitive explanation of its performance as its design is utilized in the proposed flow sensor and in subsequent chapters.

To begin the physical explanation of DEB PMUTs, we first examine the stress field in a circular vibrating plate with radius a, as shown in in Figure 5.1(a) through FEA results of a homogeneous plate vibrating in a vacuum. In this stress field six distinct regions are clear, with alternating stresses between tensile and compressive occurring at $\sim$70% of the outer radius. In general, the better we can recreate this natural stress field using piezoelectrics, the better we will "couple into" this vibration mode and thereby improve electromechanical transduction. With this stress field in mind, the reasoning for the electrode choice in conventional single-electrode unimorph PMUTs, shown in Figure 5.1(b), is apparent; an applied voltage will generate a piezoelectric stress with a specific sign, and therefore it is only desirable to cover the central 70% of the diaphragm with a top electrode, despite resulting in the majority of the diaphragm material being inactive. In contrast, the DEB design in Figure 5.1(c) eliminates inactive material and still efficiently recreates the stress field of (a). This is achieved by adding a third metal layer, grounding the top and bottom metal layers, and patterning the middle metal layer so that there are separate inner (circular) and outer (annular) electrodes which are driven differentially as shown. In this case, the bottom and top layers will have opposing electric fields and therefore the piezoelectrically-induced stress will have six regions which exactly match the pattern from (a). Each separate addition of (1) a second active piezoelectric layer, and (2) a second outer electrode, double the amount of active material in the PMUT diaphragm and correspondingly increase the sensitivity by a factor of two, explaining the observed 4× sensitivity increase. In the case of the flow sensor presented in this chapter, while DEB PMUTs are tested, only their bimorph feature is utilized (i.e., only the inner electrode is used) in order to be compatible with the electronics used.

5.3   Sensor Concept and Operating Principle

5.3.1   Overview of Sensing Mechanism

Figure 5.2 shows a conceptual schematic of the proposed PMUT-based, single-chip flow sensor. Operating in pulse-echo mode, the Tx PMUT element is driven electrically to launch ultrasound into the medium (air in this case), with a directional beam pattern so as to concentrate the acoustic energy into a narrow main lobe. The transverse flow carries the acoustic beam laterally, thereby affecting the pressure that is reflected back to the Rx PMUT elements from the surface at distance h. For rightwards flow in the figure, the pressure, which is proportional to the voltage, on Rx 2 will increase and the pressure on Rx 1 will decrease, and vice-versa for leftwards flow. In this way, the
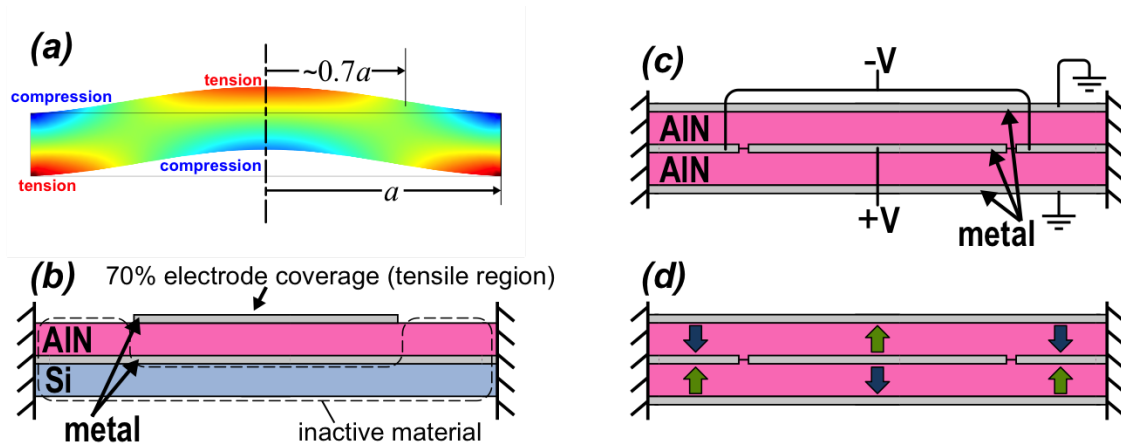
Figure 5.1: (a) Simulated stress field within a freely vibrating homogeneous diaphragm, showing alternating regions of tension and compression; schematic cross-section illustrations of standard unimorph (b) and dual-electrode bimorph (c) PMUTs; (d) electric field illustration in dual-electrode bimorph PMUT with voltages applied as in (c).
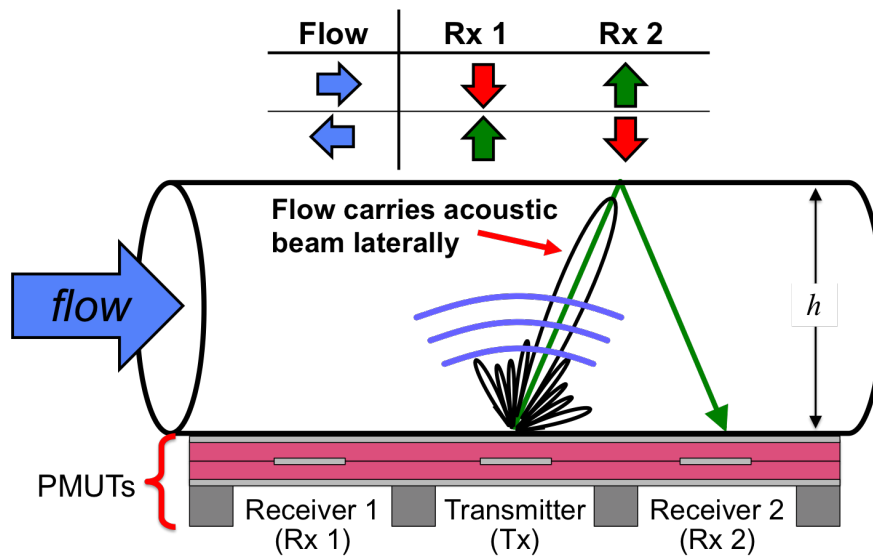
Figure 5.2: Schematic and operating principle of the proposed flow sensor.

sensor is capable of differential readouts and detecting the direction of flow.

5.3.2 Layout and Theoretical Acoustic Performance

As shown in Figure 5.3(a), each PMUT element, regardless of Tx or Rx designation, is comprised of a 6×28 rectilinear array of circular bimorph PMUTs. The individual PMUTs have a radius of a=105 μm for operation at a resonance frequency of 730 kHz, a pitch of p=460 μm, and the full element size is 2.8 mm×1.3 cm.

As previously mentioned, it is critical to the function of the sensor that the ultrasonic output is highly directional; since the element is situated such that the air flow is in the y-direction, the directivity pattern of interest is in the y-z plane. According to the acoustic product theorem [48], the directivity pattern $D_{el}(\theta)$ of the full element can be represented as:

$$D_{el}(\theta) = \frac{\sin\left(\frac{kw}{2}\sin\theta\right)}{N\sin\left(\frac{kp}{2}\sin\theta\right)} \frac{48J_3(ka\sin\theta)}{(ka\sin\theta)^3} \tag{5.1}$$

where the first and second terms are the directivity patterns of a $w \times L$ rectangular aperture (with $L \gg \lambda$) and of a circular PMUT [33], respectively, $k = 2\pi/\lambda$ is the acoustic wavenumber, N=6 is the number of PMUTs in the y-direction, and θ is the angle from the z-axis. Using FEA in Comsol Multiphysics, (5.1) has been validated by approximating each row of circular PMUTs as a long rectangular PMUT to simulate the acoustic field in the y-z plane. As shown in Figure 5.3(b), the two methods show strong agreement and predict a narrow 3 dB beamwidth of 9 degrees due to a large kw of about 36, and sidelobes at or below -12 dB within $\pm45°$.

In order to characterize the effect of flow on the system, the simplified model of Figure 5.4 is proposed. In the real system, the separation between Tx and Rx PMUTs are much smaller than the reflector height h and the lateral flow speed v is much less than the sound speed c=343 m/s, so that to first order the time of flight is constant and given by $ToF = 2h/c$. Under these conditions the problem can be simplified by using the method of images [48], which states that the echo of a wave from a source and off a reflective surface is equivalent to the source having been symmetrically placed on the opposite side of the reflector and removing the reflector. This analogy holds with the presence of lateral flow, however the "image" of the Tx PMUT is carried downstream by a distance $v \times ToF$ as shown. The translation of the image entirely accounts for the effect of the lateral flow so that the acoustic field can be described in terms of the angle $\theta = \tan^{-1}\left(\frac{y'}{2h}\right)$, where $y' = y_0 - v \times ToF$ and y_0 is the center-to-center spacing between the Tx and Rx PMUTs. With acoustic reciprocity dictating that the transmit and receive directivities are equivalent, the average pressure at the Rx PMUT will have been shaped twice by D_{el}, so that the relative change in pressure
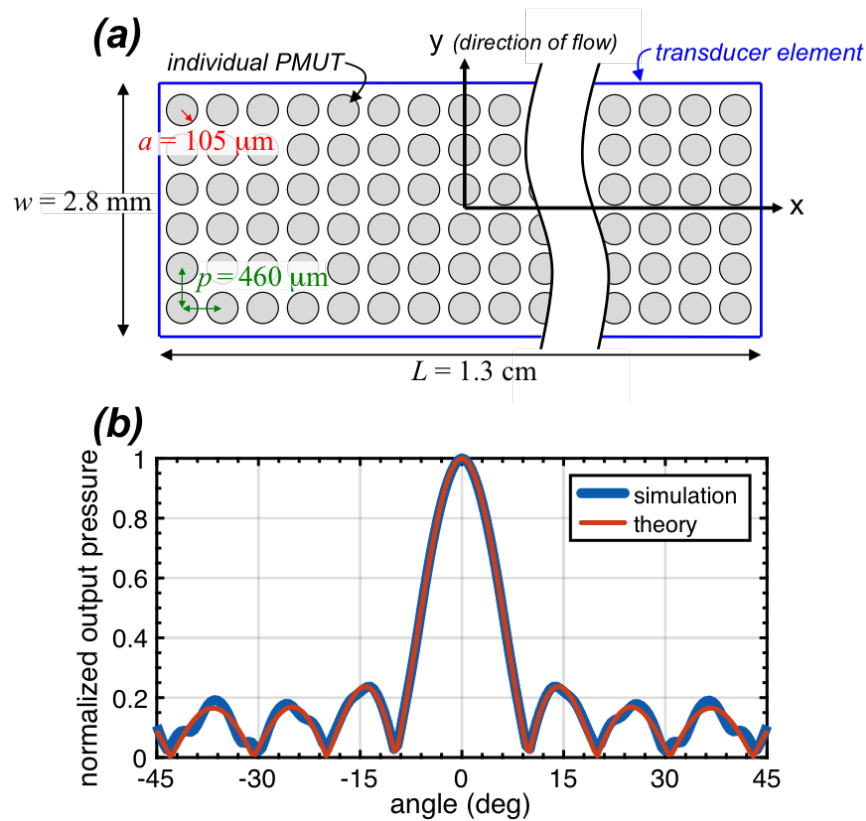
Figure 5.3: The (a) layout geometry and (b) far-field directivity pattern of a transducer element, comprised of 6×28 PMUTs.
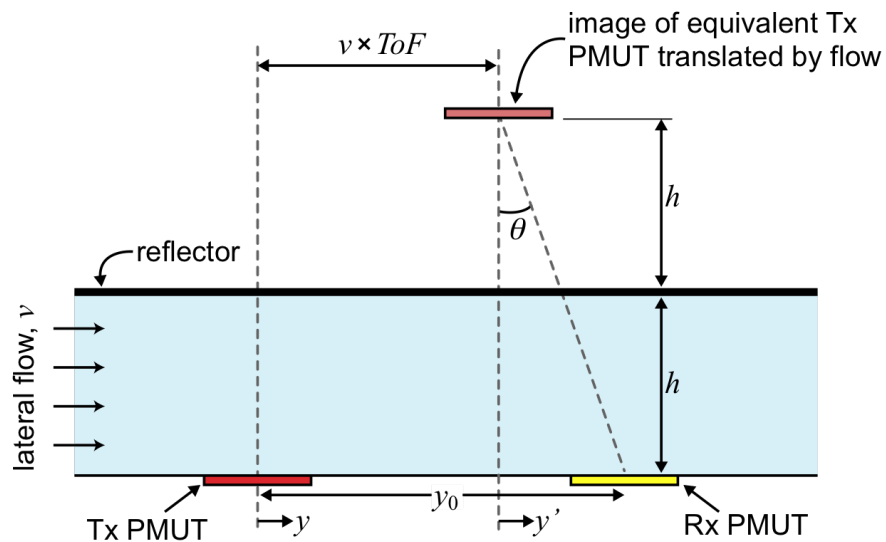
Figure 5.4: Schematic of geometry and approach used in simplified acoustic model of the proposed single-chip flow sensor.

as the flow speed is changed can be approximated as

$$\bar{p}(y_0, v) = \frac{D_{el}^2\left(\frac{y_0 - v \times ToF}{2h}\right)}{D_{el}^2\left(\frac{y_0}{2h}\right)}. \tag{5.2}$$

Intuitively speaking, $\bar{p}$ is the flow-dependent average pressure on the Rx element normalized by the no-flow (v=0 m/s) pressure, where near-field effects have been neglected for simplicity and analytic tractability.

In order to validate the proposed simplified analytical model, time-dependent FEA simulations were performed with OnScale (OnScale, UK) which allows modeling of background flow fields. Simulation results are provided in Figure 5.5(a)-(f) through snapshots at different times and with h=4 cm. As shown in Figure5.5(a), the simulation domain has a hard acoustic boundary at the top to serve as a reflector, and the bottom boundary is discretized such that there are three regions; along each of the two Rx domains the average pressure is calculated in order to be related to (5.2), and the Tx region is prescribed as a 15-cycle, 730 kHz, 1 m/s sinusoidal velocity boundary. The velocity field for v=5 m/s is shown in Figure 5.5(f), displaying the zero-flow border that was used to prevent simulation instabilities. As shown for the simulations with v=0 m/s in (a)-(c), the transmitted acoustic beam is highly directional and reaches the reflector at $t \approx$115 μs. In (d) and (e), the reflected pressure distribution on the PMUT plane is displayed for v=0 and 5 m/s respectively, showing that the acoustic energy has been deflected downstream by the lateral flow.

A comparison between FEA results and (5.2) for downstream and upstream Rx PMUTs respectively located at y_0=5.6 and -5.6 mm is provided in Figure 5.5(g). As evidenced by the strong correlation between the two methods, the approximate analytical model yields accurate results and can therefore be a powerful tool to help set layout designs for specific flow sensing applications. Furthermore, at low positive flow velocities, as the main lobe steadily approaches the downstream and recedes from the upstream element (vice-versa for negative wind velocities), the sensor shows a nearly linear response with opposite trends for the downstream and upstream elements, thereby enabling differential measurements and evaluation of flow direction. This analysis indicates that the Rx pressure changes by about 4 and 5%/ms^{-1} for h=5 and 4 cm, respectively. A slightly higher sensitivity is expected for the reflector at h=4 cm due to a smaller no-flow Rx pressure, and the shallow reflector slightly widens the linear range because a higher flow velocity is required for the main lobe to reach the Rx element. The main lobe is centered on the Rx elements at v=±24 and ±19 m/s for the 4 and 5 cm reflectors, respectively, at which speed the image of the Tx PMUT from the analytical model is directly above the Rx PMUT and therefore the maximum Rx pressure is achieved.
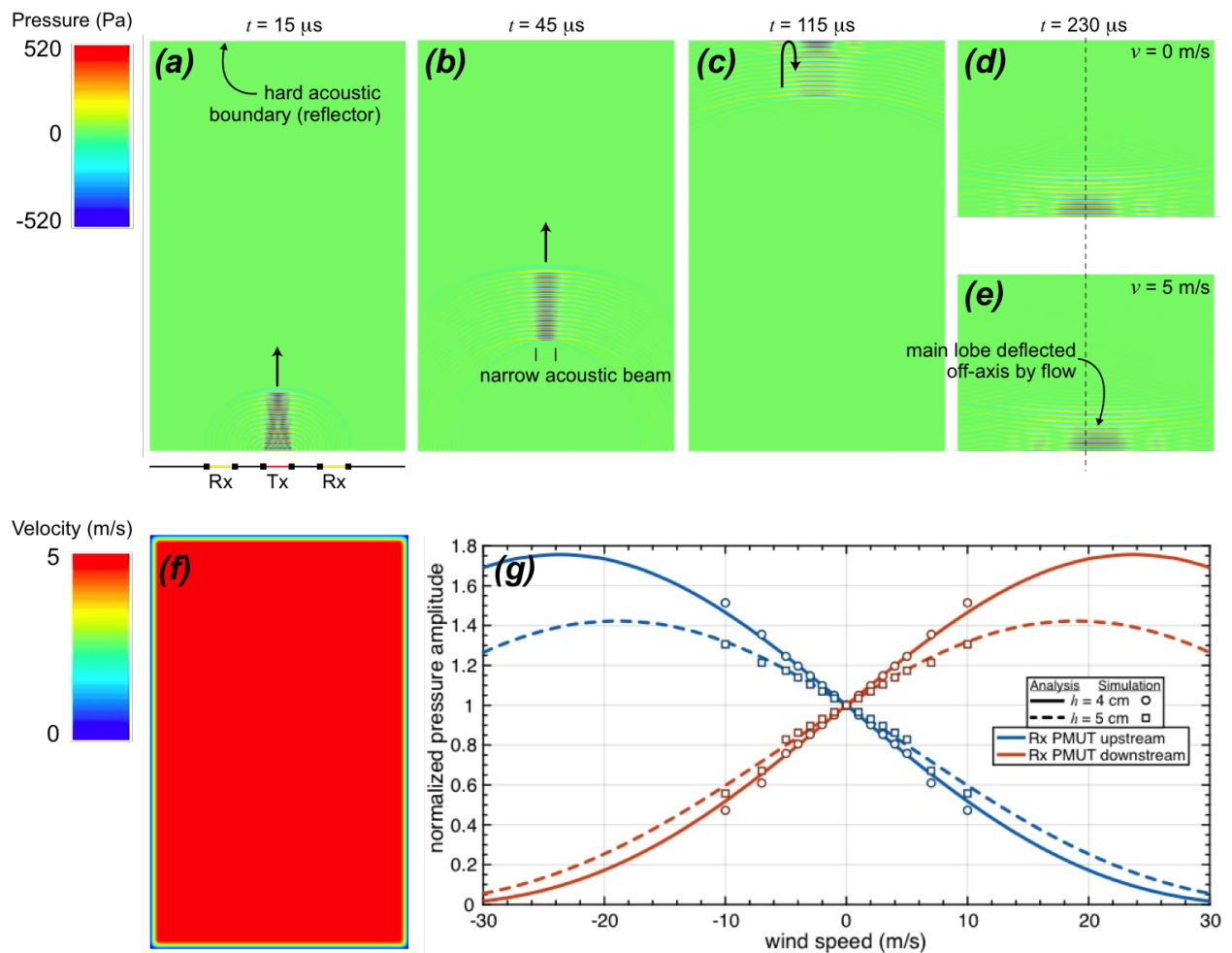
Figure 5.5: (a)-(d) Snapshots of the simulated acoustic field in the absence of flow at various times after launching the ultrasound pulse, and (e) simulated acoustic field when the echo reaches the PMUT plane with a flow of 5 m/s, showing that the main lobe of has been deflected off-axis. (f) The velocity distribution used in OnScale simulations. (g) Comparison of the dependence of the pressure amplitude on surrounding flow as predicted by theoretical analysis and FEA simulations, showing good agreement.

5.4 Experimental Evaluation

5.4.1 Methods

Figure 5.6(a) shows the experimental setup used to evaluate the proposed single-chip flow sensor. The transducers are fixed in place with an aluminum reflector placed 5 cm away from their surface, and a Sunon PF92381BX DC brushless fan (not shown) connected to an adjustable PWM control module generates lateral flow across the transducers. As previously mentioned, the transducers used in this work are bimorph PMUTs based on aluminum nitride that were previously reported on and fabricated by our lab [25] and are leveraged to provide a SNR boost that allows high-fidelity pulse-echo measurements to be acquired in air without integrated interface electronics. The geometry and frequency of all devices are the same as those used in previous sections of this work, and an optical image of the device chip can be found in the detail of Figure 5.6(a) with two individual PMUT elements outlined. In the configuration shown, the Tx and Rx elements are spaced in the direction of flow with the Rx element downstream of the Tx element; in the Rx PMUT upstream configuration, the same elements are used but the Tx and Rx designations are switched. The off-chip readout circuit is shown in Figure 5.6(b) which leverages a charge amplifying architecture to achieve high SNR with a simple off-the-shelf op-amp that requires only ± 5 V power supply rails.

5.4.2 Results and Discussion

Two sample pulse-echo waveforms taken with different reflector heights are displayed in Figure 5.7, where the Tx element is driven with a 10 V_{pp}, 10-cycle 730 kHz square wave burst and each Rx signal is post-processed with a 3rd-order 300 kHz-1 MHz Butterworth bandpass filter in MATLAB. Early on, the Rx signals show notable undesired signals due to a combined effect of cross-talk, reflections from other nearby non-ideal acoustic boundaries, and ring-down due to the narrow PMUT bandwidth. These effects die down within about 120 µs, however, such that the echo from the reflector surface is received during a "quiet period" i.e., it is clear and without interference. The ToF for the first reflection is 235 µs with a reflector height of h=4 cm, which, with a sound speed of 343 m/s, corresponds to a round-trip distance of 8 cm as expected. Furthermore, the received echo for h=5 cm is delayed by 55 µs, which indicates an added round-trip distance of 1.9 cm that is very close to the expected value of 2 cm. Somewhat counterintuitively, however, the signal from the closer reflector is significantly weaker than from the further reflector. Despite having the same Tx pressure output and a shorter acoustic travel length, thereby resulting in lower spreading losses, the lower Rx voltage for the h=4 cm case is due to the directivity of the transducer; for the 4 and 5 cm cases, respectively, the Rx element lies at a launch angle of $5.3°$ and $3.9°$ from the Tx element,
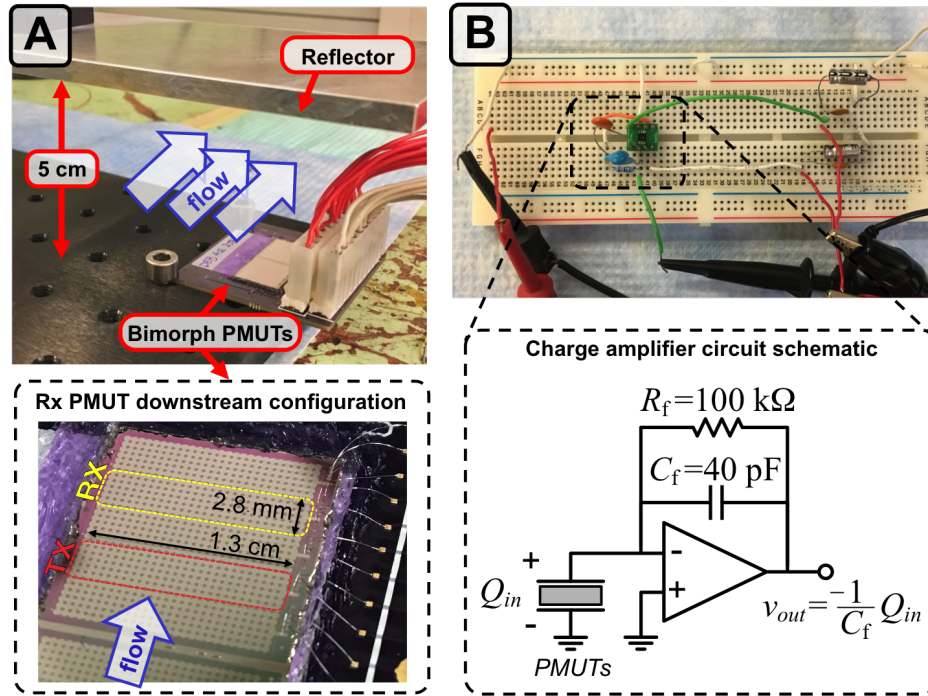
Figure 5.6: (a) The test setup used to validate the operation of the flow sensor. The detail shows the bimorph PMUT device chip in the Rx PMUT downstream configuration; (b) image and schematic of the off-chip charge amplifier readout circuit.

corresponding to directivity values of $D_{el}(\theta)$=0.75 and 0.84. In simple terms, when the reflector is closer, the Rx element lies farther from the main lobe.

In order to minimize the sensitivity to noise, rather than looking at pulse amplitude (a single-time quantity), the output of the sensor M is taken as:

$$M = \sqrt{\int_{t_1}^{t_2} V^2 \, dt} \tag{5.3}$$

where V is the Rx voltage, and the integral is evaluated within a 100 μs window that contains the full reflection. The physical significance of M is that it is proportional to the square root of the energy contained within the pulse.

The sensor output with h=5 cm and at different flow speeds is collected in both the Rx PMUT upstream and downstream configurations, normalized by the no-flow output, and plotted in Figure 5.8(a), where the absolute flow speed is measured with a HoldPeak-866B digital anemometer. With the upstream and downstream configuration showing opposite linear trends, as predicted by analysis, the sensor is shown to be capable of determining the direction of flow and of differential readout. While determining flow direction is useful in itself, the differential readout is not only
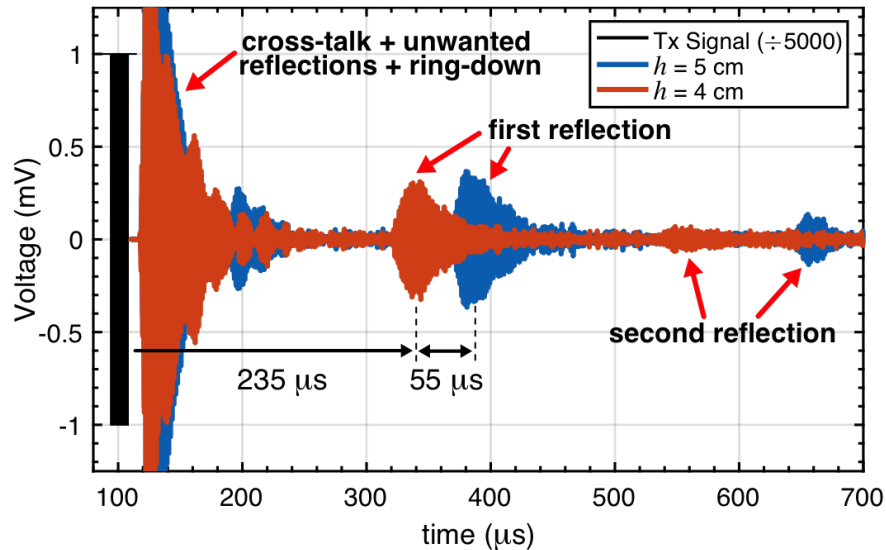
Figure 5.7: Sample pulse-echo waveforms taken with two different reflector heights. As the reflector moves from 4 to 5 cm away, the first reflection grows in amplitude and is delayed in time.

beneficial in its intrinsic sensitivity boost, but also in the robustness it adds to the system; for instance, differential measurement should negate the impact of factors that change the output of both upstream and downstream PMUTs in the same way - e.g., changes in ambient pressure and temperature. With a slope of -7%/ms^{-1}, the Rx PMUT upstream configuration is more sensitive than the downstream configuration, which has a slope of 2.9%/ms^{-1}. While a difference in sensitivity is predicted by the simple model previously introduced, the overall sensitivities are higher than the model predicts. Possible sources for this discrepancy are the non-uniform flow profile including boundary layers, a slightly different directivity pattern than predicted, and frequency-dependent acoustic absorption in air, which could result in an effective frequency reduction in the Rx pressure wave thereby exciting the PMUT off-resonance.

The measurement process is repeated for a reflector height of h=4 cm, and the differential measurements, defined here as the difference between the downstream and upstream readings, for both cases are provided in Figure 5.8(b). The differential readings exhibit linear trends with high sensitivities of 9.6%/ms^{-1} and 16.9%/ms^{-1} for reflector heights of 5 and 4 cm, respectively. In either case, the sensitivity of our reported sensor represents a stark improvement over the 5.9%/ms^{-1} sensitivity reported by previous MUT-based air flow meters. Furthermore, as previously noted, the sensitivity boost from utilizing a closer reflector is due to the lower no-flow signal amplitude, in effect decreasing the denominator of (5.2). While posing this clear benefit, the reflector cannot be moved arbitrarily close to the PMUT surface, as the first reflection will become merged with the interfering signals, rendering the measurement inaccurate.
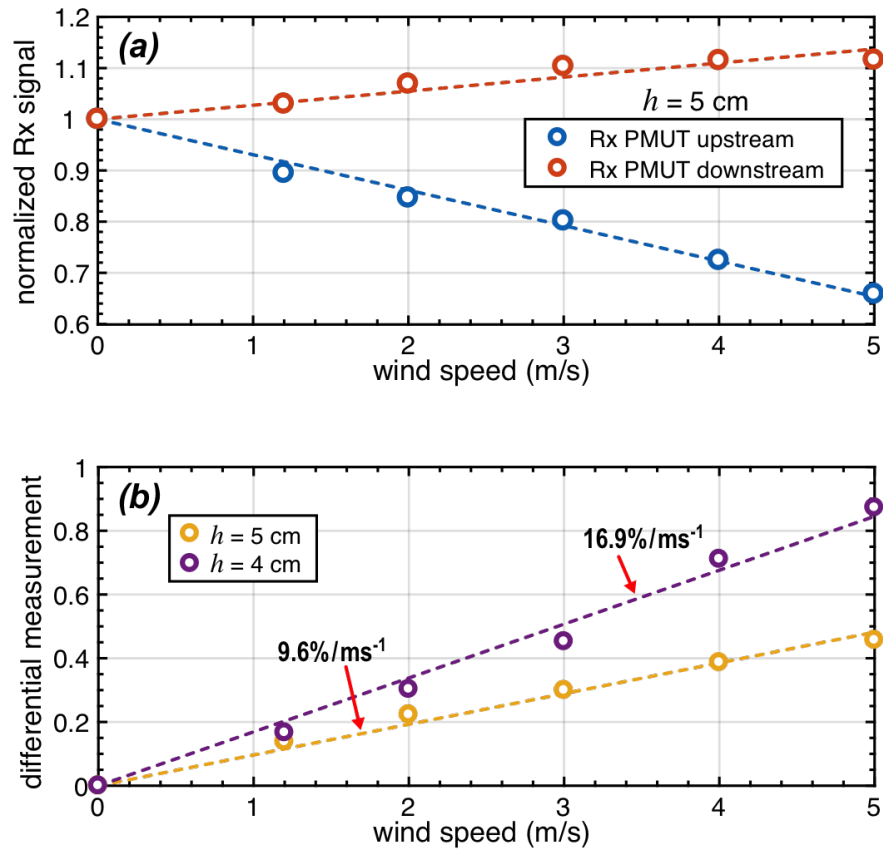
Figure 5.8: (a) Measured signal versus flow speed with a reflector height of 5 cm. In accordance with theoretical predictions, both the upstream and downstream configurations show a linear response for the range of tested flow speeds, and the upstream configuration shows a higher sensitivity than the downstream configuration. (b) Differential readings for two different reflector heights, exhibiting linear behavior and high sensitivity. As expected, the sensitivity increases for closer reflectors.

5.5 Conclusion and Outlook

In this chapter, we have introduced the first PMUT-based, single-chip sensor for measurement of both direction and speed of air flow. The sensor comprises multiple spatially distinct transducer elements, each of which can act as a transmitter or receiver, and the system does not require any voltages over 5 V. With a sensitivity as high as $16.9\%/\mathrm{ms}^{-1}$, it represents a more than 180% improvement over previously reported MUT-based air flow sensors [80]. As shown through analysis, simulation, and testing, the root of the high sensitivity lies in the high-performance PMUT architecture, the highly directional acoustic output due to the array dimensions, and most importantly, the spatial separation of elements. The differential output further boosts sensitivity and should also enhance reliability across a range of operation conditions. The increased sensitivity and func-

tionality displayed by our flow sensor should expand the application space of MUT-based flow measurement and allow more users to take advantage of this cost-effective miniaturized approach.

On another note, the flow sensor developed here has also served as a proof of concept for an operating principle that can be readily extended in several ways. For instance, a true vector flow sensor with x/y differentiation could be designed by separating PMUT elements in two dimensions as shown in Figure 5.9(a). Similar concepts could be used outside of flow measurements as well, such as the ultrasonic tilt sensor proposed in Figure 5.9(b). The development of such sensors is recommended as a topic of future research.
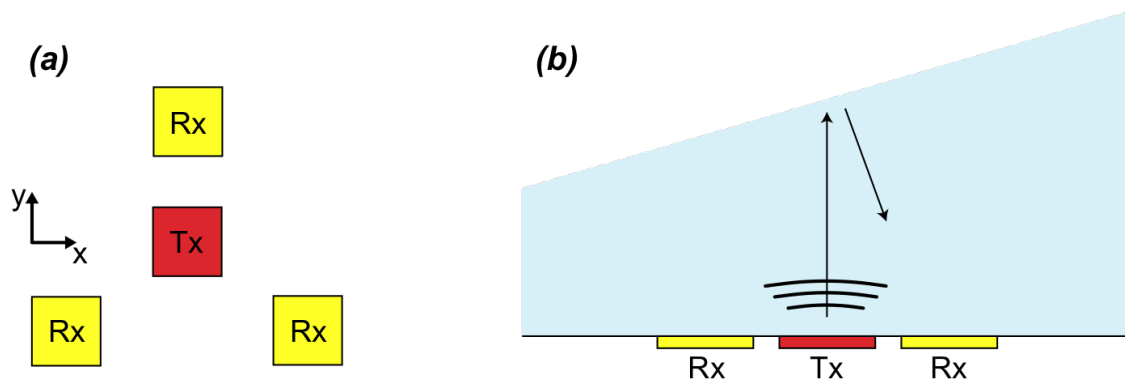
Figure 5.9: Proposed extensions of the operating principle used by the reported flow sensor. (a) Vector flow sensor capable of differentiating flows in the x and y directions; (b) Tilt sensor,

Chapter 6

Concentric Ring-shaped Bimorph PMUTs for High Power Output: Array Modeling and Design

Throughout the previous chapters, two high-performance piezoelectric micromachined ultrasonic transducer (PMUT) designs have been explored and utilized, namely the ring-shaped and dual-electrode bimorph (DEB) architectures. Each of these were shown to individually be capable of improving the acoustic performance of a PMUT as compared to conventional designs, and although the fusion of the two ideas is straightforward and has been alluded to, it has not yet been explored. Furthermore, a logical evolution from a standalone ring-shaped PMUT, considering the benefits of both high-performance architectures, is to create a multi-transducer array of concentric ring-shaped PMUTs. To this end, an equivalent circuit network model for analyzing concentric arrays of ring-shaped bimorph PMUTs is reported here and utilized to provide intuition on their design.

6.1   Introduction and Motivation

While the capabilities of micromachined ultrasonic transducers (MUTs) are notably improved by the use of high-performance designs, the performance of a single device is simply insufficient in most applications, and arrays of many transducers are employed instead. One such case is the flow sensor from Chapter 5, where an emphasis is placed on using the array geometry to tailor the acoustic beam-pattern, which in turn determines the sensitivity of the system. Additionally, most ultrasound systems require arrays in order to produce adequate acoustic power or intensity. For example, both standard imaging transducers and the previously mentioned flow sensor utilize arrays to collect echo signals with acceptable signal-to-noise ratio. Threshold acoustic intensities that are not feasible for single transducers are also necessary for various medical therapies, such

as ultrasound-induced hyperthermia for cancer treatment and low-intensity pulsed ultrasound (LI-PUS) for healing of tissue and bone [81], [82]. The range of intensities used in medical treatments ranges from over 100 W/cm^2 for hyperthermia [83], down to 5 W/cm^2 for lesion generation and interstitial treatments [84], [85], or $10-30$ W/cm^2 in LIPUS therapies [25]. Such high intensities are typically reached by using arrays with electronic phase delays to steer and focus the acoustic power [43].

To understand and estimate the performance of MUT arrays and help guide their design, an analysis of the full array must be performed. Coupled with the multi-physics nature of the transduction, the system complexity increases with the number of transducers in the array, quickly making the computation times of finite element analysis (FEA) simulations prohibitive. Instead, researchers have typically opted for an analytical approach that leverages equivalent circuit models. With the literature traditionally focused on circular MUTs, this has resulted in a well-established framework for the analysis of 2D arrays of transducers. For instance, an analytical approach was used to develop an equivalent circuit model for arrays of curved and flat PMUTs spaced on a rectangular grid [43]. Similar efforts have been undertaken in the field of CMUTs as well, such as the evaluation of the total and mutual radiation impedance between circular transducers with hexagonal spacing [86], which was later used to develop design guidelines for high-power CMUT arrays [87] and in an analysis of CMUT dynamics based on an equivalent circuit [88].

In contrast to the efforts mentioned above, concentric arrays of ring-shaped transducers have also been proposed. While inherently incapable of steering the acoustic beam laterally due to their axisymmetric structure, such arrays have drawn interest largely due to their simplified and improved acoustic focusing compared to linear arrays [89], [90]. On the other hand, concentric arrays also show promise in their ability to achieve high fill-factors [91]. As depicted in Figure 6.1
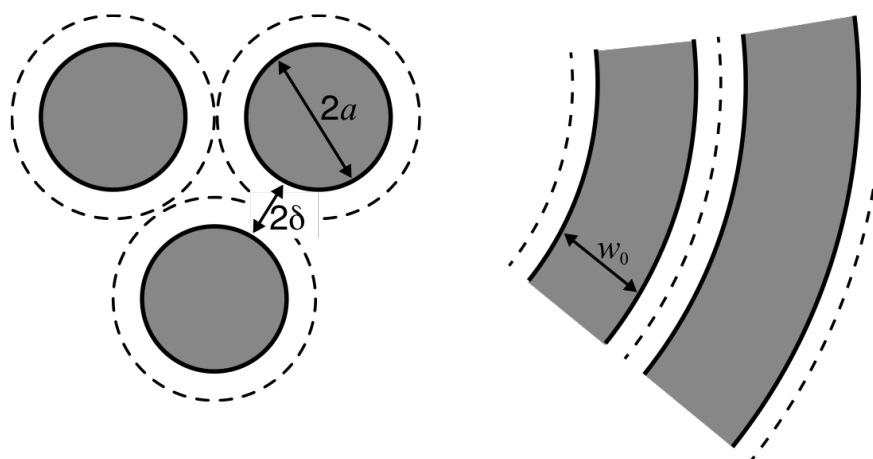
Figure 6.1: Comparison of the layouts and fill-factors of arrays comprising circular MUTs (left) and concentric ring-shaped MUTs (right). The gray area represents active area, where the dashed lines represent the spacing between transducers, which is typically limited by design rules.

the fractional reduction in active area associated with the standoff distance 2δ, which is typically limited by process-dependent design rules, can be much less for a concentric array than for closely packed circular transducers. By way of example, for $2a = w_0 = 100$ μm and $2\delta = 50$ μm, the fill-factors of the arrays of circular and ring-shaped transducers are 40% and 67%, respectively. Neglecting any effects on the dynamics of the individual transducers, the acoustic power generated by an array increases with the fill-factor, making concentric arrays well-suited for applications that require strong acoustic output.

Despite these potential benefits, there have been no modeling efforts on concentric MUT arrays to date, and thus their design remains largely unexplored and sub-optimal. As such, this chapter presents the derivation and validation of an equivalent circuit network model for concentric arrays of ring-shaped PMUTs. Considering the inherent advantages towards high-power arrays, the equivalent circuit model is developed for the bimorph PMUT architecture in order to boost transmit efficiency, however it is straightforward to adapt the same framework to unimorph or other PMUT designs. The utility of the equivalent circuit model is further demonstrated by extracting simplified design equations for PMUT arrays aimed at maximizing the transmitted acoustic power, which in turn also displays fundamental differences from the approach used for high-power CMUT design due to the nature of the drive-amplitude limitations in each.

6.2 Acoustic Coupling and Array Equations

A schematic of the layout and geometry of a concentric array of ring-shaped PMUTs is provided in Figure 6.2(a), where shaded regions represent areas where the transducer diaphragm is released and free to vibrate, white represents mechanically anchored regions, and the electrodes are omitted for clarity. All of the N ring-shaped PMUTs in the array have the same width w_0 for frequency-matching purposes, as described in previous chapters. Each PMUT is further characterized by its mean radius r_{0i}, where i is used to index the individual PMUTs, with $i = 1$ referring to the innermost transducer and increasing to N for the outermost transducer. The PMUT-to-PMUT pitch is $\Delta = w_0 + 2\delta$ so that the outer diameter is $OD = 2r_{01} + 2\Delta(N-1) + w_0$ and the array forms an annular acoustic aperture with outer radius $b_{ap} = OD/2$, inner radius $a_{ap} = r_{01} - w_0/2$, and area $A_{ap} = \pi(b_{ap}^2 - a_{ap}^2)$.

If each individual PMUT had no impact on its neighboring transducers, the entire array could be analyzed by solving the system equations defined by the circuit model from Chapter 3 for every PMUT, and then superposition could be used to calculate the quantity of interest (e.g., power output or input impedance). However, as each PMUT vibrates it generates an acoustic pressure that imparts a force on the other PMUTs in the array, thereby coupling all PMUTs within the array and altering their dynamics. We therefore model the array as N individual PMUTs as shown in Figure 6.2(b), each with stiffness k_i, mass m_i, turns ratio η_i, and applied voltage V_i as determined
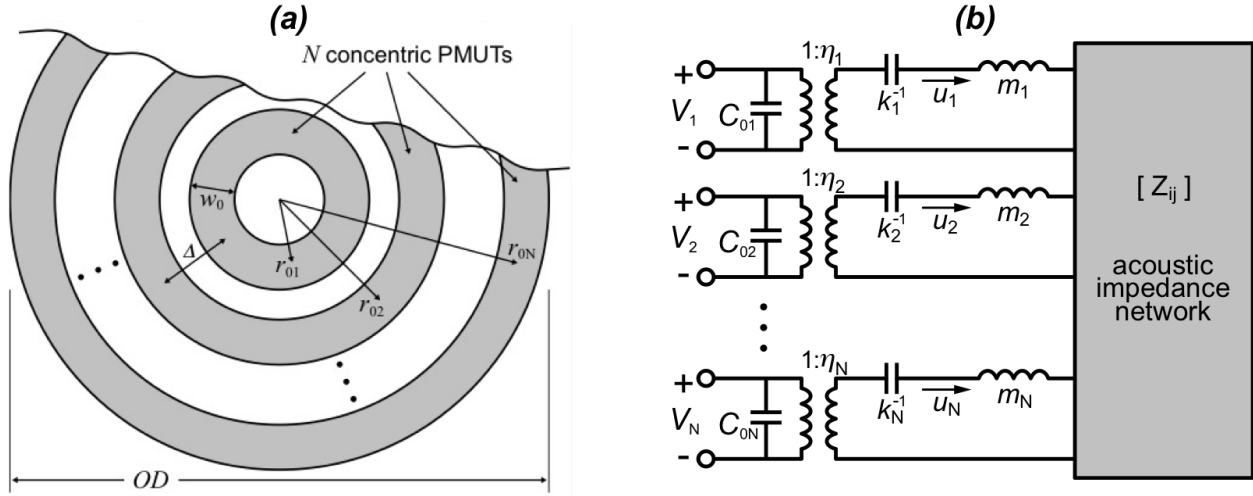
Figure 6.2: (a) Geometry and dimensions used to define arrays of concentric ring-shaped
PMUTs, with gray regions corresponding to released diaphragms and electrodes omitted; (b)
equivalent circuit model with N-port acoustic network coupling all PMUTs together.

by the standalone PMUT modeling in Chapter 3, that are coupled through an acoustic impedance
network that captures the mutual interactions between PMUTs and is a standard MUT array anal-
ysis technique. Following Figure 6.3, the nature of these mutual interactions can be intuitively
described by examining the simulated pressure field generated by a standalone ring-shaped PMUT
with $r_0 = 500\,\mu\text{m}$ and $w_0 = 100\,\mu\text{m}$ at 2 MHz in water. If a second PMUT were introduced to this
simulation, there would be several notable consequences: (1) the second PMUT would feel a force
from the acoustic field generated by the first PMUT; (2) this force would be highly dependent on
the location and size of the second PMUT; and (3) as the second PMUT vibrates, it would generate
its own acoustic pressure field that would in turn have an impact on the first PMUT. Mathemati-
cally, these interactions are modeled using the mutual acoustic impedance Z_{ij} between the i-th and
j-th PMUTs in the array:

$$Z_{ij} = \frac{F_{ij}}{u_j} = \frac{1}{u_j} \int_{A_i} p_j(r)\phi_i(r)\, dA_i, \tag{6.1}$$

where F_{ij} is the equivalent force on PMUT i from PMUT j; u_j is the spatial-average velocity of the
j-th transducer; $A_i = 2\pi r_{0i}w_0$ is the area of the i-th PMUT; $p_j(r)$ is the complex acoustic pressure
generated by transducer j; and $\phi_i(r)$ is the vibration modeshape of transducer i, which is the same
modeshape used in defining the equivalent circuit for standalone PMUTs in Chapter 3:

$$\phi_i(r) = \frac{15}{8}\left(1 - \left(\frac{r - r_{0i}}{w_0/2}\right)^2\right)^2. \tag{6.2}$$

It is worth noting that Z_{ij} can be equivalently conceptualized as the power delivered by transducer
i due to the pressure generated by transducer j divided by the product of their velocities, as is the
more common explanation in the literature. Furthermore, p_j can be expressed using the Rayleigh
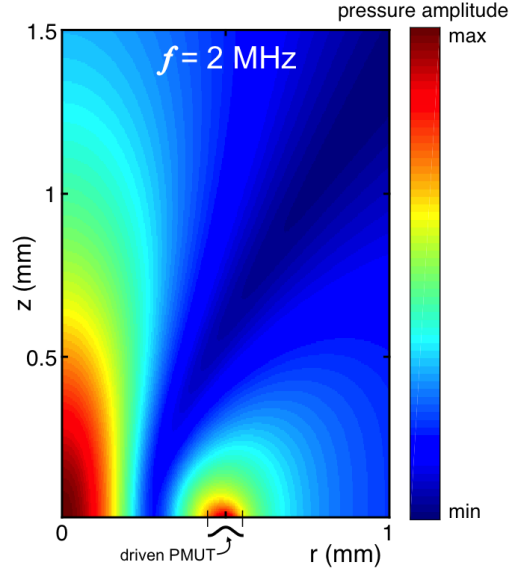
Figure 6.3: Simulated pressure field from a single PMUT with $r_0 = 500$ μm and $w_0 = 100$ μm, showing large fluctuations in the PMUT plane that are responsible for the strong position dependency of the mutual impedance.

integral in analogous fashion to (3.68):

$$p_j(r) = j\frac{\rho_a c_a k u_j}{2\pi} \int_{A_j} \phi_j(R,\theta)\frac{e^{-jkR}}{R} \, dA_j, \tag{6.3}$$

where ρ_a and c_a are the respective density and sound speed of the acoustic medium, k is the acoustic wavenumber, and the coordinates R and θ are defined in Figure 6.4 (α does not appear due to the assumed axisymmetric conditions). Using these coordinates, the mutual impedance simplifies to

$$Z_{ij} = j\rho_a c_a k \int_{a_i}^{b_i} \left[\iint_{A_j} \phi_j(R,\theta)e^{-jkR} \, dRd\theta \right] r\phi_i(r) \, dr. \tag{6.4}$$

As in the derivation of the self-radiation impedance of Chapter 3.3.4, (6.4) does not have a closed-form solution and must instead be evaluated by numeric integration, however it can be useful to express it in as a non-dimensional specific acoustic impedance z_{ij}:

$$Z_{ij} = \rho_a c_a A_i z_{ij} = \rho_a c_a A_i(r_{ij} + jx_{ij}). \tag{6.5}$$

Furthermore, $Z_{ij} = Z_{ji}$ as a corollary of acoustic reciprocity [48], however since each PMUT has a different area, $z_{ij} \neq z_{ji}$ if $i \neq j$. In the case of $i = j$ on the other hand, Z_{ij} is equivalent to the self-radiation impedance derived in Chapter 3.

Figure 6.5 provides an example of the specific mutual impedances between two concentric ring-shaped PMUTs of width $w_0 = 100$ μm and $r_{01} = 150$ μm as the mean radius of the innermost
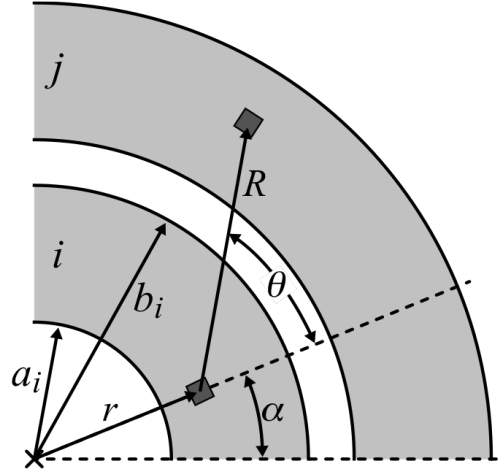
Figure 6.4: Coordinates used for evaluating the Rayleigh integral for mutual impedances.

PMUT, as evaluated with (6.4) and (6.5). The effect of changing frequency at a given pitch Δ is shown in (a)-(b), and the effect of changing Δ at constant frequency is shown in (c)-(d). In general, the curves for each condition share some characteristics, but the behavior including locations of zeros and maxima or minima are highly dependent on the exact layout geometry and acoustic medium. The difference in behavior between (a)-(b) and (c)-(d) is due to changes in the acoustic directivity: as the frequency changes at constant Δ, the directivity of both PMUTs changes ((a)-(b)), however as the pitch changes at constant frequency, only the directivity of PMUT 2 changes ((c)-(d)). This in turn indicates that ring-shaped PMUTs cannot be approximated as acoustic point-sources, which should be expected since $kr_0 > 1$ typically, whereas it is sometimes an acceptable simplification for arrays of circular PMUTs where each device is acoustically small. It is also notable that the radiation resistance between two neighboring PMUTs can be negative, indicating that each PMUT is absorbing power from the acoustic field generated by the other PMUT.

With this definition of mutual impedance, the force at the acoustical port of each of the N PMUTs can be expressed in terms of the individual velocities in matrix form as

$$
\begin{bmatrix} F_{a1} \\ F_{a2} \\ \vdots \\ F_{aN} \end{bmatrix} = \begin{bmatrix} Z_{11} & Z_{12} & \cdots & Z_{1N} \\ & Z_{22} & \cdots & Z_{2N} \\ & & \ddots & \vdots \\ \text{symm.} & & & Z_{NN} \end{bmatrix} \begin{bmatrix} u_1 \\ u_2 \\ \vdots \\ u_N \end{bmatrix} \quad \text{or} \quad \underset{\sim}{F}_a = \underset{\sim}{Z}_a \underset{\sim}{u} \tag{6.6}
$$

where $(\underset{\sim}{\ })$ denotes a matrix or vector variable, and $\underset{\sim}{Z}_a$ is an $N \times N$ acoustic impedance matrix with entries defined in (6.4) that is symmetric about the main diagonal. From (6.6), the input impedance to the acoustical network as seen by the i-th PMUT, Z_{ai}, can be expressed as

$$
Z_{ai} = \frac{F_{ai}}{u_i} = R_{ai} + jX_{ai} = \sum_{j=1}^{N} \frac{u_j}{u_i} Z_{ij}, \tag{6.7}
$$
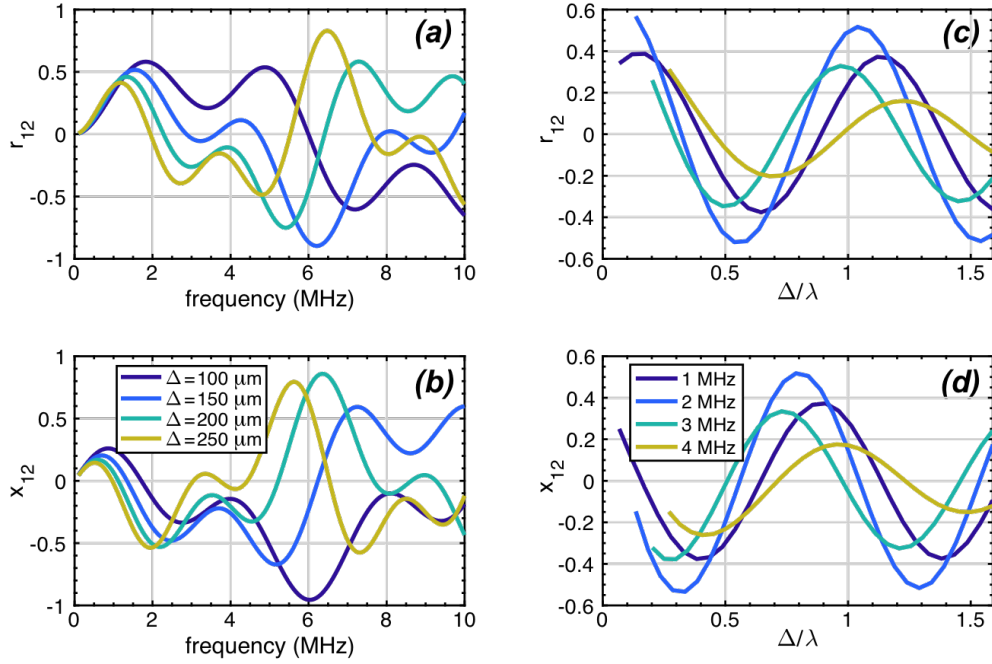
Figure 6.5: Specific mutual resistance (top row) and reactance (bottom row) between two concentric ring-shaped PMUT with the mean radius of the inner PMUT constant at $r_{01} = 150\,\mu\text{m}$. (a) and (b) show constant-pitch curves with variable frequency, (c) and (d) show constant-frequency curves with variable pitch.

where R_{ai} and X_{ai} are the radiation resistance and reactance of the i-th PMUT, each of which depends not only on the mutual impedances, but also on the velocity of all PMUTs. In order to relate the velocities to the driving voltages we define the mechano-acoustical impedance matrix $\mathbb{Z}_{ma}$ as

$$\mathbb{Z}_{ma} = \begin{bmatrix} Z_{m1} & & & \\ & Z_{m2} & & \\ & & \ddots & \\ & & & Z_{mN} \end{bmatrix} + \mathbb{Z}_a, \tag{6.8}$$

where the first (matrix) term is a diagonal matrix containing the mechanical impedances

$$Z_{mi} = \frac{k_i}{s} + s m_i, \tag{6.9}$$

where s is the complex frequency variable, and the lumped parameters for stiffness k and mass m are equivalent to the terms derived in the standalone ring-shaped PMUT equivalent circuit and are listed in Table 3.1. The equivalent mechano-acoustical impedance seen by the i-th PMUT can therefore be expressed as

$$Z_{eq}^i = \frac{\eta_i V_i}{u_i} = Z_{mi} + Z_{ai}, \tag{6.10}$$

which is the series combination of the mechanical impedance and the input impedance at the acoustical port of each PMUT. Furthermore, from (6.8), the $2N$ system equations can be written

$$\eta \underline{V} = \underline{Z}_{ma} \underline{u} \tag{6.11}$$

$$\underline{i} = \eta \underline{u} + s\underline{C}_0 \underline{V}, \tag{6.12}$$

where $\underline{i}$ and $\underline{V}$ are $N \times 1$ vectors of the individual PMUT currents and voltages, respectively; and η and $\underline{C}_0$ are $N \times N$ diagonal matrices of the individual PMUT turns ratios and clamped capacitances, respectively.

6.3 Array Performance

In order to analytically simulate the performance of an array of concentric ring-shaped PMUTs, (6.11) can be solved by pre-multiplying by the inverse of the mechano-acoustical impedance matrix

$$\underline{u} = \underline{Z}_{ma}^{-1} \eta \underline{V}, \tag{6.13}$$

which is then combined with (6.12) to solve for the currents $\underline{i}$, if desired. This process is repeated at each frequency of interest due to the frequency dependence of $\underline{Z}_{ma}$. Since the voltage, current, and velocity of each PMUT in the array will in general be different, it will be useful to define several array-wide quantities to succinctly describe the aggregate performance of all PMUTs. We first define the average velocity $\bar{u}$ as the total volumetric velocity of the array divided by the total vibrating area

$$\bar{u} = \frac{1}{A_v} \sum_{i=1}^{N} u_i A_i, \tag{6.14}$$

where $A_i = 2\pi r_{0i} w_0$ is the area of the i-th PMUT, and $A_v = \sum_i A_i$. As reference to the reader, since the displacement of ring-shaped PMUTs has been previously shown to be nearly independent of mean radius r_0, it is reasonable to expect that the velocity of each PMUT in the array is close to $\bar{u}$, with variations caused by the acoustic loading. Furthermore, using the radiation resistance R_{ai} defined in (6.7), the time-averaged acoustical power output of the i-th PMUT P_i and of the entire array P_{tot} can respectively be expressed as [48]

$$P_i = \frac{1}{2} R_{ai} |u_i|^2 \tag{6.15}$$

$$P_{tot} = \sum_{i=1}^{N} P_i. \tag{6.16}$$

Throughout the remainder of this work, various arrays and geometries will be simulated using the developed model, however the following are kept constant unless otherwise noted: (1) the

Table 6.1: Expressions for Concentric Array of Bimorph Ring-shaped PMUT Equivalent Circuit Network Elements

Parameter		Expression
Clamped capacitance	C_{0i}	$\varepsilon_{33}^T (1 - k_{31}^2) \dfrac{4\pi r_{0i} w_0}{h_{tot}}$
Coupling coefficient	k_{31}^2	$\dfrac{2 d_{31} e_{31,\mathrm{f}}}{\varepsilon_{33}^T}$
Transformer turns ratio	η_i	$\dfrac{45\pi}{8}\left(\dfrac{2 r_{0i}}{w_0}\right) e_{31,\mathrm{f}} h_{tot}$
Mechanical mass	m_i	$\dfrac{20\pi}{7}\rho_s r_{0i} w_0$
Mechanical stiffness	k_i	$\dfrac{1440\pi D_b r_{0i}}{w_0^3}$
Bending rigidity	D_b	$\dfrac{Y_0 h_{tot}^3}{12(1-\nu)}$
Total radiation resistance	R_{tot}	$\rho_a c_a A_v \left(\dfrac{w_0}{\Delta}\right)$

acoustic medium is assumed to be water, with $\rho_a = 1000 \text{ kg/m}^3$, $c_a = 1481 \text{ m/s}$, and neglecting absorption; (2) the PMUT diaphragm has two layers with $h_{bot} = h_{top} = 3$ µm for a total thickness $h_{tot} = 6$ µm and is entirely composed of aluminum nitride (AlN), implicitly assuming that the electrode layers will be sufficiently thin as to not have an impact; and (3) the bimorph structure is used, effectively doubling C_0 and η from their values for the standalone unimorph ring-shaped PMUT equivalent circuit in Chapter 3, but having no impact on the expressions for any other lumped parameters. It should be noted that while these diaphragms are thicker than those used in the previous sections of this dissertation, thin plate theory is still applicable since $w_0/h_{tot} > 10$. For convenience, the expressions for the lumped elements in the equivalent circuit for ring-shaped bimorph PMUTs are compiled in Table 6.1.

6.3.1 Finite Element-Based Model Validation

In order to validate the analytical modeling approach developed here, FEA simulations are performed in Comsol Multiphysics v5.0 (Comsol Inc., Burlington, MA, USA) and the results between the two analyses are compared via the output power. In FEA, the output power is calculated by

Table 6.2: Array geometries used in Section 6.3.

Parameter		Value	
		FEA and analytical model in Sect. 6.3.1	Prototype in Sect. 6.3.2
Number of PMUTs	N	6	15
Innermost mean radius	r_{01}	325 μm	175 μm
PMUT width	w_0	110 and 120 μm	130 μm
Pitch	Δ	225 μm	180 μm
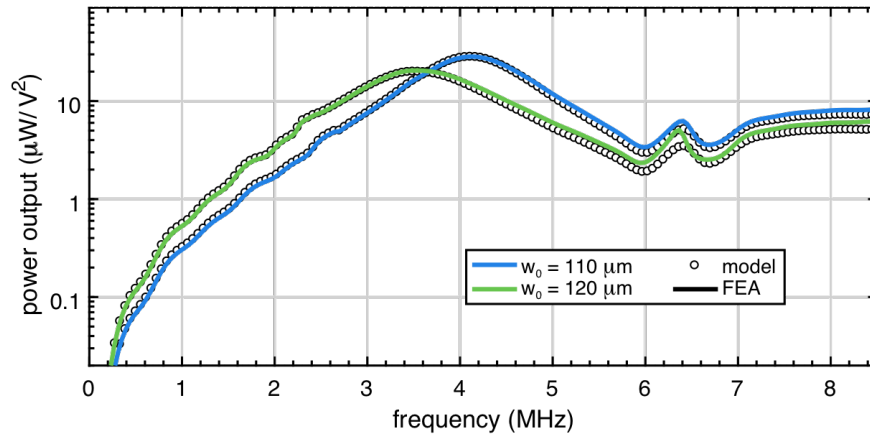
Figure 6.6: Comparison of acoustical power output as determined by FEA simulations (solid lines) and the developed equivalent circuit network model (circles) for example arrays of concentric ring-shaped PMUTs with two different ring widths, showing strong agreement between the two methods of analysis.

integrating the acoustic intensity over a surface S enclosing the entire array

$$P = \frac{1}{2} \iint_S \mathrm{Re}[p(\vec{u} \cdot \hat{n})^*] \, dS \tag{6.17}$$

where $\vec{u}$ is the acoustic particle velocity, $\hat{n}$ is the unit normal to surface S, and $(*)$ denotes complex conjugate. The simulated array has dimensions as compiled in Table 6.2 and two different values of $w_0 = 110$ and 120 μm, and all PMUTs are driven together with a 1 $\mathrm{V_{ac}}$ input voltage. A comparison between the output power as calculated from FEA simulations and the equivalent circuit network is provided in Figure 6.6. While the performance characteristics of each array and the impact of changing device dimensions will be covered in the remainder of this chapter, the two methods of analysis show excellent agreement in terms of amplitude and frequency of peak power output, existence of high-frequency fluctuations, and overall shape, thereby validating the developed equivalent circuit network model.

6.3.2   Performance Characteristics of a Prototype Array

As summarized in the rightmost column of Table 6.2, an array of 15 concentric ring-shaped PMUTs with 130 μm width, 180 μm pitch, and innermost mean radius of 175 μm is used as a prototype example in order to provide an in-depth examination of the performance behavior and relevant phenomena. To observe the effects of coupling between PMUTs through the acoustic medium, which is modeled by the mutual impedances, we compare the modeled results with a theoretical "uncoupled" case, wherein all mutual impedances are artificially set to zero so that $\mathbb{Z}_a$ contains only the diagonal entries of self-radiation impedances. Figure 6.7(a) displays the array-wide mean velocity $\bar{u}$ (thick lines) along with the velocity of PMUT number 7 (thin lines) both with and without the mutual coupling. As has been found for arrays of circular MUTs [43], the mutual effects reduce the mean velocity and increase the array resonance frequency. This is also observed in the corresponding acoustic power output plot in Figure 6.7(b), where the mutual effects reduce the peak power output from 55 to 40 μW/V^2, increase the peak-power frequency from 2 to 3 MHz, and increase the half-power bandwidth by over 100% from 1.5 to 3.1 MHz. Such effects have been shown in arrays of circular MUTs to be tunable to some degree by altering the array configuration and geometry since the mutual interactions are highly dependent on these factors, and can therefore be used to improve the array performance, e.g., in terms of bandwidth [92] or gain-bandwidth product [93]. Furthermore, this shows that designing arrays based on a model that does not take the coupling into account will produce quite inaccurate predictions.

In addition to the general shift in amplitude and frequency, less straightforward phenomenon are also displayed in Figure 6.7(a) and (b). In the artificially uncoupled case, PMUT 7 shows a velocity that nearly matches the array-wide average, with quasi-sinusoidal variations due to the fluctuations in self-radiation impedance, as described in Chapter 3. However, in the physical case where mutual interactions are considered, several high-Q resonance peaks are observed at lower frequencies (note that the plot has been cut and PMUT 7 achieves a simulated maximum velocity of $25\ \mathrm{mm/s/V}$, not shown). While the velocity of PMUT 7 has an overall trend that again correlates with the array mean, these low-frequency resonances represent a large deviation from $\bar{u}$ and are strongly dependent both on the array geometry as well as location within the array (i.e., PMUT 1, 7, and 15 all show different low-frequency behavior). The combined effect of the low-frequency resonances can be seen as minor fluctuations in the array-wide mean velocity, and as more pronounced peaks and valleys in the acoustic power output, especially at $1.8\ \mathrm{MHz}$ where the array output dips to less than 10 μW/V^2.

One way to investigate the physical origin of these fluctuations is to examine the velocity distribution of all PMUTs at the frequencies of interest. In doing so, we utilize the approach in [94] and first define the normalized velocity fluctuation $\bar{u}_f$ as

$$\bar{u}_f = \frac{1}{N|\bar{u}|_{\max}} \sum_{n=1}^{N} \big| |u_n| - |\bar{u}| \big|, \tag{6.18}$$
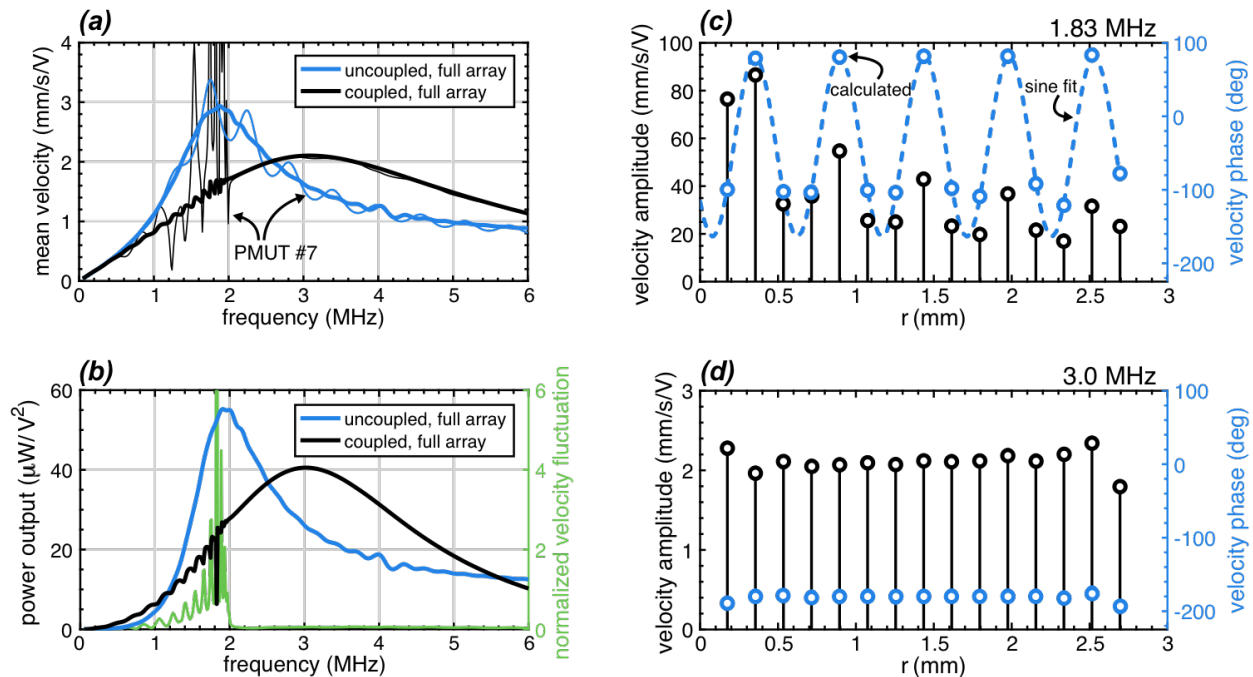
Figure 6.7: Calculated performance of the prototype array with dimensions summarized in Table 6.2. (a) The mean velocity and (b) the power output for both the artificially uncoupled and the coupled cases to show the effects of mutual interactions. The velocity amplitude and phase of each individual PMUT is provided at 1.83 MHz (c) and 3 MHz (d).

which is a measure of the PMUT-to-PMUT variation in velocity amplitude at each frequency. As shown in Figure 6.7(b), the valleys (peaks) in $\bar{u}_f$ exactly correspond with the peaks (valleys) in power output. This suggests that when the mutual interactions cause neighboring PMUTs to have widely varying velocities, the PMUTs transfer power between one another rather than radiating power away into the useful acoustic field. This type of behavior has been observed in arrays of circular MUTs, and has been attributed to the formation of Rayleigh-Bloch waves, which are dispersive guided-wave modes that are confined to the MUT-medium interface [94] and are caused by the mutual interactions. Such surface waves occur in periodic MUT arrays of both infinite and finite extent, where in finite arrays reflections from the array edge give rise to Fabry-Pérot waves that take place at frequencies where the element size is an integer number of wavelengths, cannot occur at frequencies above an upper cutoff frequency determined by the PMUT pitch, and exhibit phase velocities lower than that of the surrounding medium. Despite not radiating useful acoustic power, this phenomenon can be a significant source of cross-talk and may therefore play an important role in array performances [95].

The existence of this type of surface wave is further verified in Figure 6.7(c), which displays the amplitude (black) and phase (blue) of the velocity of each PMUT in the array at 1.83 MHz, where the phase is taken with respect to the input voltage. There is a general trend of decreasing velocity

amplitude with increasing radius, however repetitive variation patterns are also apparent. The phase of the individual PMUTs also varies drastically, and as shown by the dotted line sine fit, exhibits a very regular repetitive variation. Noting that axisymmetric waves far from the origin have a phase factor $e^{-j\omega r/v_p}$, where v_p is the phase velocity, the observed sinusoidal phase variations further suggest the existence of an interface wave. With the fitted wavelength of 544 µm at 1.83 MHz, the interface wave has a phase velocity of 996 m/s, which is less than the sound speed of water, as expected. In summary, the low-frequency fluctuations are due to the mutual interactions creating variable acoustic loading, which is dependent on both frequency and location within the array, and can give rise to trapped interface waves at specific frequencies.

In contrast, at frequencies above 2 MHz in the prototype array, the velocity fluctuation is dramatically reduced and the spurious resonances die out, producing smooth frequency response curves in terms of both velocity and power output. This is substantiated by the amplitude and phase distributions at 3 MHz shown in Figure 6.7(d), which are predominantly uniform: the velocity amplitude has an average value and standard deviation of 2 and 0.12 m/s, respectively, and the phase has an average value and standard deviation of -181° and 4.4°, respectively. With 3 MHz as the frequency of maximum power output, this shows that the array is most efficient when the velocities are nearly equal, despite the individual amplitudes being lower than in (c). Furthermore, noting that the phase is nearly -180° and that the turns ratio η is negative since $e_{31,f} < 0$, it is clear that the PMUT velocity is in-phase with the effective transformer force $\eta_i V_i$. Therefore, the imaginary part of the equivalent mechano-acoustical impedance Z_{eq}^i is approximately zero.

While the mechanical impedance is straight-forward to evaluate, the acoustic impedance is less obvious, yet still has a strong impact on the array as described above. To examine the acoustic impedance of the array, we first note that each PMUT sees a different input impedance to the acoustic network as shown in (6.7). In the interest of conciseness and clarity, we therefore use an approach related the one taken by Senlik *et al.* [86] to define a single effective acoustic impedance $\bar{Z}_a$ that is representative of the entire array

$$\bar{Z}_a = \left(\frac{1}{N} \sum_{i=1}^{N} \frac{\eta_i V_i - Z_{mi}\bar{u}}{A_i \bar{u}} \right) A_v, \tag{6.19}$$

which weighs the contribution of each PMUT to the representative acoustic impedance according to its area. In order to normalize this impedance, we define $\bar{r}_a$ and $\bar{x}_a$ as the real and imaginary parts of $\bar{Z}_a$ divided by $\rho_a c_a A_v$, respectively. Another useful approximation can be made by noting that at the array-wide resonance, all PMUTs are moving with nearly the same complex velocity. If this were exactly true, the total acoustic impedance of the array Z_{tot} could be written as [96]

$$Z_{tot} = \sum_{i=1}^{N} \sum_{j=1}^{N} Z_{ij}. \tag{6.20}$$

Figure 6.8(a) provides a comparison between the effective (black) and total (blue) acoustic impedance of the prototype array. The two methods show excellent agreement in both the real and imaginary components of the impedance, with small deviations occurring at frequencies below 2 MHz, where the complicated array loading effects discussed previously occur. In fact, if the velocity magnitude and phase of all N PMUTs were exactly equal, the two impedances would be equivalent.

A third approximation is also introduced, which is motivated by the similarity between a concentric array with all PMUTs moving at equal velocity and a piston vibrator with radius b_{ap} defined by the array aperture. With the fill-factor $f_F = w_0/\Delta$ defining the ratio of the total vibrating area to the total aperture area (i.e., $A_{ap}f_F = A_v$), we approximate the normalized impedance of the array as f_F^2 times the normalized impedance of a piston:

$$z_p = f_F^2 \Big[1 - \frac{J_1(2kb_{ap})}{kb_{ap}} + j\frac{H_1(2kb_{ap})}{kb_{ap}} \Big], \qquad (6.21)$$

where J_1 and H_1 are the first-order Bessel and Struve functions, respectively [48]. Shown as the green curve in Figure 6.8(a), this piston approximation offers a good prediction of the real part of the acoustic impedance with a 3.6% error at the array resonance of 3 MHz, however it is only accurate for the imaginary component at low frequencies when $\lambda \gg \Delta$. Similar behavior to this, wherein the acoustic impedance of a large ($kb_{ap} > 1$) array is approximated well by a piston radiator for the resistive component but poorly for the reactive component, has been observed both as a general trend (e.g., [48]) and in arrays of circular MUTs (e.g., [95]). While not explicitly shown, it was found that the reactive component of the total impedance could be approximated to first-order by $X_{tot} = \rho_a c_a A_v \Delta/\lambda$ rather than (6.21).

Further insights into the array dynamics can also be provided by examining the impedances seen by individual transducers. To this end, Figure 6.8(b) displays the acoustic impedance seen by PMUT 7 both as it operates within the array (black curve) and as a standalone device (blue curve), where the standalone case is equivalent to the artificially uncoupled case examined previously. Here, the impedance of the PMUT operating in the array is taken as the total impedance times the fractional area, $Z_{tot}(A_i/A_v)$. Within the array, the resistive impedance is mostly flat with respect to frequency, however its magnitude can be larger or smaller than when operating as a standalone device depending on the frequency. Interestingly, the reactive impedance of the standalone PMUT is substantially larger than that of the same PMUT operating within the array, indicating that the mutual coupling between PMUTs effectively reduces the mass-loading on the individual PMUTs within the array. Noting that resonance frequency $f_0 \propto m_{tot}^{-1/2}$, where the total mass m_{tot} has both mechanical and acoustical contributions, this decrease in reactive impedance is in fact the cause of the increase in resonance frequency that is observed in Figures 6.7(a)-(b).
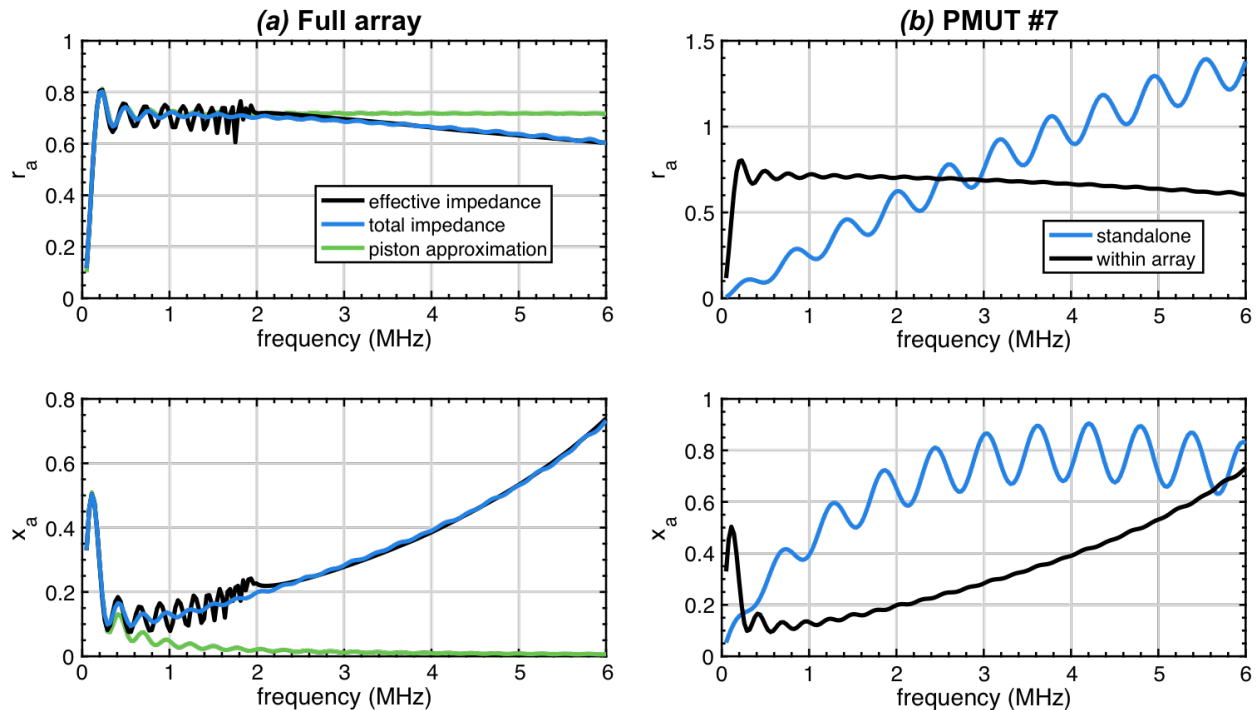
Figure 6.8: (a) Comparison between the effective, total, and piston acoustic impedances for the full prototype array, showing the real component of the impedance can be approximated by a scaled piston. (b) Inspection of changes in acoustic loading on PMUT 7 in the prototype array due to the mutual coupling, which tends to make the acoustic resistance more constant and reduces the acoustic reactance.

6.4 Design Equations for Increasing Acoustic Power Output

In order to design a concentric PMUT array with high power output, we must first identify which factors are the ones that limit power. In the field of CMUTs for example, vertical displacement, and therefore velocity, is limited by the thickness of the transduction gap, which can be 100 nm or thinner and is further reduced by the application of a bias voltage. Noting the fundamental relationship of $P = R_a|u|^2/2$, the question of maximizing power output therefore simplifies to the question of maximizing R_a, since it is assumed that it is possible to drive the CMUT with a sufficiently large voltage to take advantage of the full available displacement swing. To this end, high-power CMUT arrays are typically designed by picking layout dimensions, diaphragm thicknesses, and array configurations that produce the greatest feasible acoustic loading [87].

In contrast, the previously developed design guidelines are not applicable to PMUTs since they are not gap-limited transducers. Furthermore, mechanical nonlinearities are not a limiting factor in liquid-coupled PMUTs due to their relatively small displacements: the prototype array in the

previous section has roughly $1\,\mathrm{pm/V}$ sensitivity at resonance, so that even if a $1\,\mathrm{kV}$ driving voltage were used, the displacement would still be much less than the diaphragm thickness. Instead, PMUTs are typically limited by the input voltage, whether it be the maximum accessible voltage, or the maximum voltage that the piezoelectric material can withstand (as limited either by breakdown or other failure mechanisms). Since velocity is proportional to excitation voltage, the relevant metric by which to evaluate our PMUT arrays is then the output power per squared input volt, P/V^2.

To examine the design of high-power concentric PMUT arrays, we begin by assuming that all PMUTs are driven with the same voltage $V_1 = V_2 = \cdots = V_N$ and vibrate with the same complex velocity $u_1 = u_2 = \cdots = u_N$, which was shown to be a good approximation at resonance in Figure 6.7(d), so that the acoustic power output by the array from (6.16) simplifies to

$$P_{tot} = \frac{1}{2}|u_1|^2(R_{a1} + R_{a2} + \cdots + R_{aN}) = \frac{1}{2}|u_1|^2 R_{tot}, \tag{6.22}$$

where R_{tot} is the real part of the total acoustic impedance Z_{tot} defined in (6.20). As previously noted, the equivalent mechano-acoustical impedance of each PMUT at resonance is resistive, and with the only resistive impedance source being the acoustic impedance, the PMUT velocity at the array resonance may be expressed as

$$u_1 = \frac{\eta_1 V_1}{R_{tot}(A_1/A_v)}. \tag{6.23}$$

Interestingly, the combination of (6.22) and (6.23) shows that the acoustic power output per squared input volt increases as the radiation resistance decreases, which is in direct contrast to the basis of the design approach used for CMUTs. Furthermore, by inserting the expressions for the turns ratio and using the piston approximation for the radiation resistance according to (6.21) such that $R_{tot} \approx \rho_a c_a A_{ap}\mathrm{Re}\{z_p\}$, the power output per squared input volt is found as

$$\frac{P_{tot}}{V^2} = \frac{15.82}{\rho_a c_a} A_{ap}\, e_{31,\mathrm{f}}^2 \left(\frac{h_{tot}}{w_0^2}\right)^2. \tag{6.24}$$

With a remarkably simple form, (6.24) is valuable in identifying important design parameters and understanding how they impact array performance. Intuitively, the power output increases with the area of the acoustic aperture and the square of the thin-film piezoelectric constant $e_{31,\mathrm{f}}$, indicating that larger arrays of PMUTs with a more sensitive piezoelectric material will have improved acoustic performance. Perhaps less intuitive, however, is what does not appear in (6.24): power output is insensitive to pitch Δ and therefore also the fill-factor f_F. Furthermore, the diaphragm thickness h_{tot} and width w_0 do not matter on their own, but rather in relation to one another.

These effects are examined more thoroughly in Figure 6.9 by simulating three different concentric arrays of ring-shaped PMUTs with the developed equivalent circuit network model, all of which have the same outer diameter $OD = 5\,\mathrm{mm}$ and ratio h_{tot}/w_0^2, and therefore are predicted
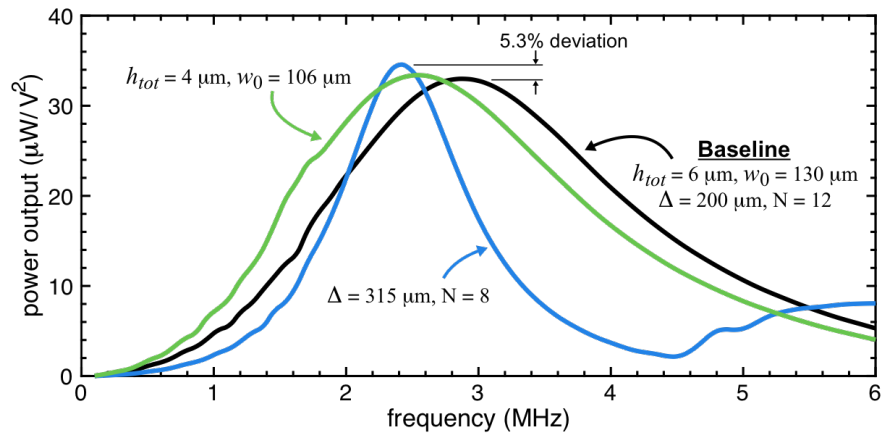
Figure 6.9: Comparison of the acoustical power output spectrum for a baseline array of concentric PMUTs (black curve), along with two other arrays that are similar to the baseline array except for: (blue curve) the pitch is increased and the number of PMUTs is correspondingly decreased; and (green curve) the thickness and width are increased while keeping h_{tot}/w_0^2 constant.

by (6.24) to have equivalent power outputs. The black curve represents the transmitted power from a baseline array, which has $N = 12$ concentric PMUTs separated by a pitch $\Delta = 200\,\mu\text{m}$ and with the same thickness and width as that of the prototype array from Section 6.3.2, and the other two curves represent arrays which differ from the baseline in specific ways as labeled. The power output shown in blue is for an array that is similar to the baseline, except with a larger pitch of $\Delta = 300\,\mu\text{m}$ and a corresponding reduction to 8 PMUTs in order to fit within the same OD. Despite the reduction in number of PMUTs and fill-factor, the power output has not substantially changed, as it is within 5.5% of that for the baseline array; the reason for this behavior is that the radiation resistance R_{tot} has dropped via a reduction in f_F, which in turn gives rise to an increase in the PMUT velocity according to (6.23) such that the net effect on power is minimal. The minor deviations in power output are not encompassed by (6.24) because the small changes in radiation impedance that cause the changes are neglected. The reduction in radiation resistance is also manifested in the transmitted power spectrum where, in conjunction with the increased mass-loading caused by the larger pitch, it results in a substantial reduction in bandwidth. The green curve, in contrast, displays the simulated output of an array with the same pitch and number of PMUTs as the baseline, but with thinner $h_{tot} = 4\,\mu\text{m}$ and less wide $w_0 = 106\,\mu\text{m}$ PMUTs used while maintaining the same ratio h_{tot}/w_0^2. In this case again, any changes in the radiation resistance are balanced by corresponding changes in velocity, so there is no substantial change in power output. Furthermore, since the fill-factor w_0/Δ is relatively close to the baseline case and there is negligible change in the acoustic mass-loading, the bandwidth of the array has not appreciably changed.

In contrast to the three arrays examined above, which all showed relatively equal power outputs, (6.24) predicts a high sensitivity on performance to the ratio of the thickness to the width squared. Interestingly, this ratio was also shown in Chapter 3 to be proportional to the unloaded resonance

frequency f_{0u}, which can be expressed for a homogeneous PMUT from (3.62) as

$$f_{0u} = \frac{3.573}{w_0^2}\sqrt{\frac{D_b}{\rho_p h_{tot}}} = 1.031\frac{h_{tot}}{w_0^2}\sqrt{\frac{Y_0'}{\rho_p}}, \tag{6.25}$$

where ρ_p and $Y_0' = Y_0/(1 - \nu_p)$ are the density and biaxial modulus of the PMUT diaphragm material, respectively. When immersed in a high-impedance acoustic medium, the resonance frequency drops to f_0 due to the extra acoustic mass-loading according to

$$f_0^2 = f_{0u}^2\left(1 + \frac{m_a}{m_m}\right)^{-1} \approx f_{0u}^2\left(1 + 0.11\frac{\rho_a\Delta}{\rho_p h_{tot}}\right)^{-1}, \tag{6.26}$$

where m_a and m_m are the respective acoustic and mechanical masses, and the final equality utilizes the first-order approximation to the acoustic mass as extracted from the total reactance. Combining (6.24) through (6.26) yields an alternate form of the array power output

$$\frac{P_{tot}}{V^2} = \frac{14.87}{\rho_a c_a}\left(\frac{\rho_p}{Y_0'}\right)A_{ap}e_{31,\text{f}}^2 f_{0u}^2 \approx \frac{14.87}{\rho_a c_a}\left(\frac{\rho_p}{Y_0'}\right)A_{ap}e_{31,\text{f}}^2 f_0^2\left(1 + 0.11\frac{\rho_a\Delta}{\rho_p h_{tot}}\right), \tag{6.27}$$

which reveals that the power output should be approximately proportional to f_0^2. To show this occurrence, arrays with $N = 6$ PMUTs, $OD = 3$ mm, $\Delta = 250$ μm, $h_{tot} = 6$ μm, and various values of w_0 are simulated using the developed equivalent circuit network model. The acoustic power output versus frequency for each array is provided in Figure 6.10(a), with a general increase in both resonance frequency and peak power output as w_0 decreases. Figure 6.10(b) explicitly shows this by plotting the peak power output versus resonance frequency for the eight simulated arrays, along with a curve fit to show that the simulations do indeed observe the predicted form $P_{tot} \propto f_0^2$ for f_0 up to 5 MHz. There is, however, a substantial drop in output power as the frequency increases further. The cause of this phenomenon is in fact a change in the total radiation resistance of the array; as shown by the (red) normalized radiation resistance curve for the $w_0 = 70$ μm array in Figure 6.10(a), R_{tot} increases dramatically at around 5 MHz, or equivalently when $k\Delta \approx 5.6$. At these frequencies, the approximation of the concentric array as a piston radiator breaks down, and the increase in R_{tot} results in diminished acoustic performance. Similar behavior has also been observed for arrays of circular CMUTs [86] and circular pistons [96], where a large jump in radiation resistance occurs at around $k\Delta = 6$.

The analysis presented above elucidates important considerations and rules for the design of high-power PMUT arrays. As the most straightforward effects, acoustic output can always be enhanced by increasing the aperture area and improving the piezoelectric materials; for example, changing the piezoelectric material to scandium-doped AlN ($e_{31,\text{f}} = 1.6$ C/m^2)[35] or PZT ($e_{31,\text{f}} = 14$ C/m^2)[33], is predicted to result in a power output that is 2.5× and 192× that of AlN PMUTs, respectively.

Nonetheless, materials and size considerations are often constrained by manufacturing capabilities or the desired application. To increase the acoustic power within typical limitations on
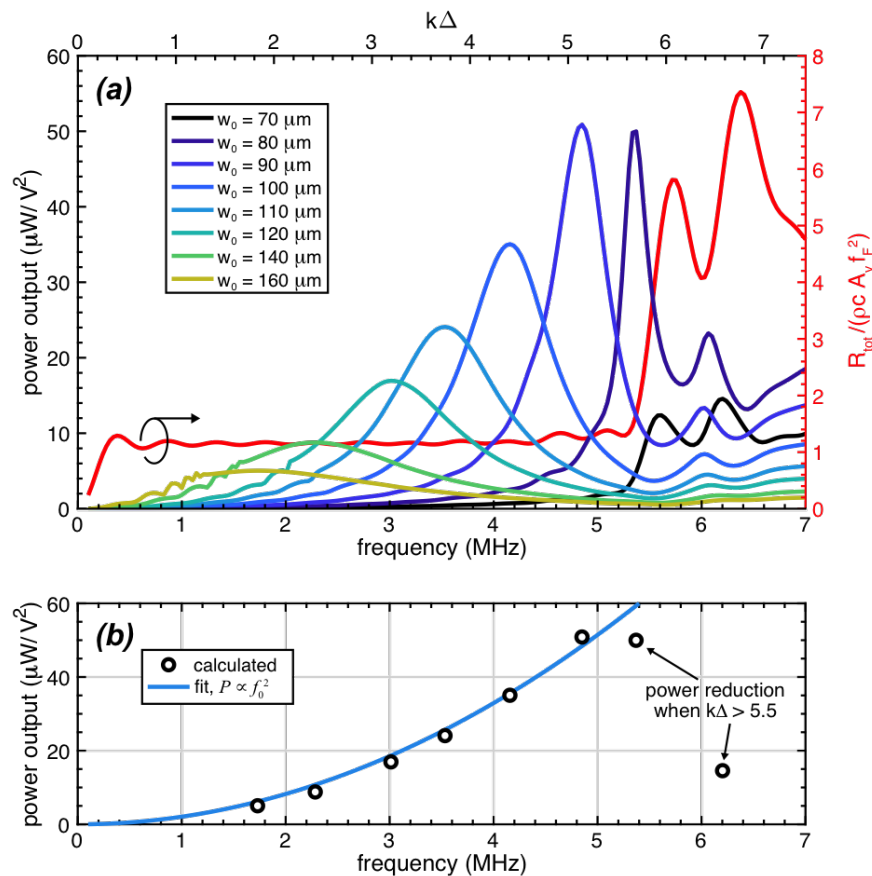
Figure 6.10: (a) Acoustic power spectrum for arrays with similar designs except with different w_0, with radiation resistance for $w_0 = 70\,\mu\text{m}$ on the right axis. (b) Peak power output versus resonance frequency for arrays in (a). Peak power output per squared input volt is nearly proportional to frequency squared, except when $k\Delta > 5.5$, where an increase in radiation resistance decreases the performance.

the other hand, it is ideal to increase frequency, which is achieved by increasing h_{tot}/w_0^2. While neglected in the approach used here, the improvement presented by increasing frequency will be diminished by acoustic attenuation, which also becomes stronger as frequency increases. The balance between output and absorption will also depend on the acoustic medium and working distance, and should therefore be accounted for in order to deliver a desired amount of acoustic power to a specific depth. Furthermore, while power output is shown to be relatively insensitive to pitch Δ, smaller values of Δ tend to increase the bandwidth and may therefore provide benefits in some applications, and it is of critical importance that the designer ensures $k\Delta < 5.5$ in order to prevent severely diminishing the power output.

6.5 Conclusion

In this chapter, an equivalent circuit network model for concentric annular MUT arrays is developed, with a specific focus on bimorph ring-shaped PMUTs. The analysis builds upon the equivalent circuit model for standalone ring-shaped PMUTs and includes the effects of each transducer on one another through the mutual acoustic impedance, which is derived from the acoustic Rayleigh integral. By comparing the resulting performance with the case of artificially uncoupled PMUTs, the mutual effects are shown to result in substantial changes in the array performance. The mutual effects are also shown to give rise to trapped interface waves at specific frequencies, which is a phenomenon that has also been observed in 2D arrays of circular transducers and results in a reduction in transmitted acoustic power at those frequencies.

Using the developed equivalent circuit model and leveraging well-supported approximations, design equations are obtained in order to simplify the complex problem of designing arrays for high acoustic power outputs. While agreeing with certain expected trends, these design equations also uncover several unanticipated results, including that the transmitted acoustic power is insensitive to fill-factor and can be boosted by increasing the frequency up to a fundamental limit determined by the pitch. By revealing such performance trends and enabling efficient analysis of multi-transducer arrays, the equivalent circuit network model is expected to be a useful tool for ultrasound transducer designers going forward. Furthermore, while developed in the context of bimorph PMUTs, it is envisioned that the model will be adaptable to other MUT architectures with only minor changes.

Chapter 7

Concentric PMUT Arrays for Focused Ultrasound and High Intensity Applications

Building upon the equivalent circuit network model developed in Chapter 6, we herein report on the fabrication and acoustic characterization of concentric arrays of ring-shaped piezoelectric micromachined ultrasonic transducers (PMUTs) based on aluminum nitride (AlN). The annular design is theoretically compared with a typical array of circular transducers in order to display the potential for strong acoustic output and effective phased-array focusing using concentric arrays. These theoretical advantages are experimentally confirmed, as fabricated prototypes are measured to have the highest reported normalized pressure output and focusing gain among PMUT arrays, both of which are due to the unique array geometry. Furthermore, the measured focal pressure exceeds 90 kPa with a low driving voltage of 6 V_{ac}, showing promise for systems that require high acoustic intensity. Considering their small size, the fabricated arrays should be especially appealing in catheter-based medical devices used for high intensity focused ultrasound (HIFU) treatments.

7.1   Introduction

In addition to its prolific use in medical imaging, the application space of ultrasound has grown to include nondestructive testing [97], wireless power transfer (WPT) [98], and minimally or non-invasive medical treatments [99]. While the desired performance specifications for ultrasound transducers (UTs) are in general system-specific, each of the mentioned applications benefits from UTs that are able to generate high acoustic intensities in controlled and confined regions. To accomplish this, ultrasound can be electrically focused by use of phased arrays, which are arrays of multiple UTs that are electrically driven with specific timing delays. Phased arrays are commonly used in medical imaging and NDT to improve signal-to-noise ratio and to enhance image resolution

[100]. Furthermore, the use of focused ultrasound can boost the efficiency of WPT systems [101], and is necessary in medical therapies to produce high acoustic intensities in the treatment zone without damaging surrounding tissues [15].

In this context, micromachined ultrasonic transducers (MUTs) show strong promise due to their low-cost wafer-based fabrication that allows for flexibility in designing multi-element arrays of densely packed transducers and tight integration with driving electronics, all with remarkably small footprints. As such, MUT-based ultrasound systems that utilize phased arrays have been the subject of numerous recent research efforts. Using piezoelectric MUTs (PMUTs), Lu *et al.* measured a $3\times$ increase in pressure output from electrical focusing, which enabled imaging of a steel phantom with $100\,\mu m$ resolution [34]. Employing PMUTs flip-chip bonded to a CMOS ASIC, Jiang *et al.* reported a $1.5\times$ contrast enhancement in ultrasound fingerprint images when using phased array focusing [33].

While the study of phased array PMUTs have thus far been limited to imaging applications, capacitive MUTs (CMUTs) for medical therapies have also been proposed, for instance in catheter-based high intensity focused ultrasound (HIFU) systems. These systems, for example, are designed to treat atrial fibrillation by using ultrasound to produce lesions in the left atrium that prevent future episodes [102], or of cancer by ablating tumors with focused ultrasound [85]. Such applications are particularly well-suited for MUTs, as traditional UTs are not readily manufacturable in a sufficiently small size to fit on a catheter and are therefore restricted to percutaneous therapies. Furthermore, a CMUT probe capable of simultaneous HIFU generation for ablation and imaging for treatment monitoring was proposed in a compelling work by Wang *et al.* [103], which could open the door to new medical treatments or make current operations safer and simpler. Due to the gap-limited displacement inherent to CMUTs, however, the imaging and ablation transducers require different membrane thicknesses and transduction gaps for efficient operation. An elaborate 11-mask fabrication process is required as a result, which increases cost and diminishes yield. This difficulty is escalated by the complex packaging that is necessary for patient safety due to the high voltages (over $100\,V$ each for DC bias and AC drive) used. In contrast to CMUTs, however, PMUTs do not require a bias voltage and are not gap-limited transducers, and may therefore be fabricated in a relatively simple process wherein imaging and high-power elements are formed in the same steps. Despite this, PMUTs have not been widely utilized in systems that require high acoustic intensities as they traditionally struggle to match the pressure output of their capacitive counterparts.

As such, we herein report on the development of new PMUT arrays for the generation of high acoustic intensities. Specifically, concentric arrays of ring-shaped PMUTs are proposed, which are motivated by a theoretical analysis that reveals the benefits of the annular structure over typical array designs, including a boost in pressure output and enhanced focusing ability. These theoretical findings are confirmed experimentally through acoustic characterization of several fabricated prototype arrays based on aluminum nitride (AlN). As presented in the last chapter, we find that the pressure output of concentric arrays of ring-shaped PMUTs is largely insensitive to fill-factor

but increases with operating frequency. The efficacy of phased array focusing is also investigated by measuring the resulting increase in peak acoustic intensity, showing that focusing is improved at higher frequencies and lower focal depths. Owing to their unique annular layout geometry, the fabricated arrays are shown to have the largest focusing gain and normalized pressure output both with and without focusing among reported PMUT arrays. With a measured focal intensity of 340 $\mathrm{mW/cm^2}$ at a low driving voltage of 6 $\mathrm{V_{ac}}$, the developed concentric PMUT arrays show feasibility for generating the intensities required in many applications.

7.2 Phased Array Comparison: Circular Versus Ring-shaped PMUTs

The de-facto standard in PMUT arrays is a 2-D grid of circular transducers, and therefore this is used as the benchmark by which to compare the concentric arrays of ring-shaped PMUTs developed here. Figure 7.1 presents a comparison of the layout geometries of the two designs: (a) the concentric array is made up of many ring-shaped PMUTs with equal width w_0 for frequency-matching purposes, spacing δ, and form an acoustic aperture with radius b_{ap}; and (b) the array of circular PMUTs utilizes a hexagonal packing scheme in order to achieve the highest possible fill-factor, and each individual PMUT has a radius a and spacing δ from any neighboring transducers. As shown in Figure 7.1(c), the optimal geometry for the purposes of acoustic focusing is that of equal-area elements [89], and so the radial boundaries of each element are not equally spaced. Therefore, in order to achieve effective acoustic focusing while maintaining frequency-matched transducers, subsets of PMUTs can be electrically connected in parallel to form "elements" or "channels" that may contain varying numbers of PMUTs in order to achieve nearly areas. In the remainder of this section, the two aforementioned array designs will be theoretically explored based on the fabricated designs presented in Section 3. The concentric array has 11 ring-shaped PMUTs with width $w_0 = 60$ μm and spacing $\delta = 50$ μm. The hexagonal-packed circle array has the same value of δ since the minimal spacing is typically specified as a design rule, and has 385 total PMUTs, each with radius $a = 35$ μm in order to have a simulated resonance frequency that matches with that of the ring-shaped PMUTs. Both arrays are circumscribed by the same circle with $b_{ap} = 1.28$ mm and are operated at 6 MHz.

Upon application of a driving voltage, the PMUTs vibrate with a spatial-average velocity u_{0i}, where i is used to index the individual transducers. The acoustic pressure field in the surrounding medium with density ρ_a and sound speed c_a can then be calculated by superposition [43]

$$p = j\frac{\rho_a c_a}{\lambda} \sum_i u_{0i} A_i \frac{e^{-j(kr_i - \omega\tau_i)}}{r_i} D_i(\theta_i), \tag{7.1}$$

where $j = \sqrt{-1}$ is the imaginary unit; λ is the wavelength; A_i is the transducer area; r_i and θ_i are

the respective distance and angle from the center of the PMUT to the field point of interest; τ_i is a time delay applied to the PMUT velocity; and D_i is the acoustic directivity of the transducer. Each of these quantities can, but do not necessarily, change from PMUT to PMUT. Furthermore, arrays are typically most efficient at frequencies where the variation in velocity between PMUTs is small, therefore we assume $u_{0i} = u_0$ is constant. In the far-field and along the main axis of the array at a distance z from the surface, (7.1) then simplifies to

$$p_{ff} = \rho_a c_a u_0 f_F \left(\frac{A_{ap}}{\lambda z} \right),$$ (7.2)

where $f_F = A_v/A_{ap}$ is the fill-factor of the array, where A_v is the total vibrating PMUT area, and A_{ap} is the aperture area, respectively. Noting the dependencies of (7.2), we define the normalized pressure output $\bar{p}$ as

$$\bar{p} = \frac{p}{2\rho_a c_a u_0 f_F} = \frac{1}{f_F} \sum_i \frac{A_i}{2\lambda} \frac{e^{-j(kr_i - \omega\tau_i)}}{r_i} D_i(\theta_i).$$ (7.3)

Since we are concerned with the on-axis pressure, and the center axis of all ring-shaped PMUTs in the concentric array are aligned, $D_i = 1$ for the concentric array. On the other hand, the main axis of the circular PMUTs are not aligned and so their directivity $D_i = 48J_3(ka\sin\theta_i)/(ka\sin\theta_i)^3$ must be accounted for [32].

A theoretical comparison of the on-axis acoustic output of the two example arrays is provided in Figure 7.2 with mineral oil ($\rho_a = 882$ kg/m^3, $c_a = 1483$ m/s) as the acoustic medium. The normalized pressures as defined by (7.3) without any applied phase delays (i.e., $\tau_i = 0$) are shown as the thin solid curves, with blue and black referring to the array of concentric rings and hexagonally-packed circles, respectively. The normalized pressure takes on a value between 0 and 1, indicating that the concentric array ($f_F = 55\%$) can generate $\sim 1.8\times$ the pressure of the arrays of circles ($f_F = 31\%$) with the same u_0. Furthermore, as r decreases from infinity, oscillatory behavior is observed in the near-field, where the complex exponential in (7.3) counters the $1/r$ hyperbolic rise. This phenomenon also reveals the operating principle of phased array focusing: with the appropriate choice of τ_i, the complex exponential can be made equal for all i, thereby allowing for drastic increases in pressure near the array. In the ideal case, every PMUT in the array can be controlled independently such that the theoretical maximum normalized pressure that can be achieved with phase focusing $\bar{p}_{fl}$ is

$$\bar{p}_{fl} = \frac{1}{f_F} \sum_i \frac{A_i}{2\lambda} \frac{D_i(\theta_i)}{r_i},$$ (7.4)

which is plotted as the dashed curves in Figure 7.2. Both arrays show a hyperbolic trend that decays to the far-field value at large z, showing that focusing is only possible in the near-field, however the concentric rings show a notably increased focusing limit due to a more efficient use of the area defined by the circumscribing circle and the fact that the maximum response axis of each transducer is aligned. In contrast to this theoretical focusing limit, in practice it is typically
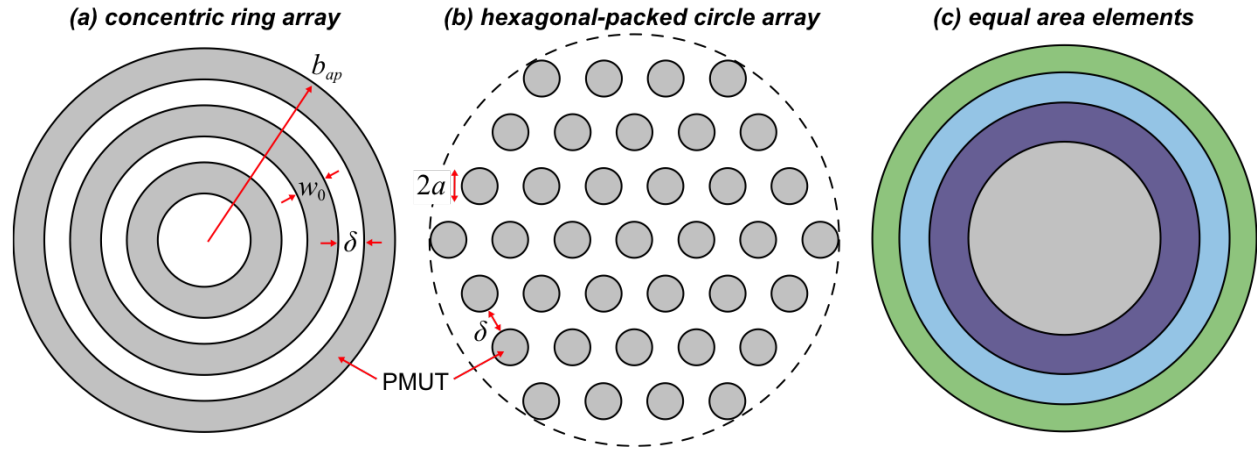
Figure 7.1: Comparison of layout geometries for (a) concentric array of ring-shaped PMUTs and (b) hexagonal-packed array of circular PMUTs. In practice, multiple transducers are connected in parallel to form elements; (c) presents a visual representation of equal area elements that optimize acoustic focusing.

not feasible to achieve independent delay control for all PMUTs in the array due to the system complexity it would entail. We therefore also evaluate $\bar{p}$ for the case of 4 channels, as shown as the thick solid curves in Figure 7.2, where the designated channel of each individual PMUT is determined by the equal-area segment from Figure 7.1(c) that contains its center, and the time delay is given by

$$\tau_i = (z_f - d_i)/c_a, \tag{7.5}$$

where $z_f = 2$ mm is the z-coordinate of the acoustic focus, and d_i is the distance from the center of the i-th element the focus. The concentric array phase focusing is considerably more effective at concentrating the acoustic power, as it achieves a normalized focal pressure of ~ 3.8, compared to ~ 2.9 for the hexagonal-packed circle array. This is consistent with previous reports (e.g., [89]), which contend that annular arrays require fewer elements to achieve high-quality acoustic focusing as compared to 2-D phased arrays.

7.3 Experimental Results

7.3.1 Device Fabrication

In order to evaluate the acoustic output of concentric arrays of ring-shaped PMUTs, prototype arrays were fabricated with the individual PMUTs having both dual-electrode bimorph (DEB) and dual-electrode unimorph (DEU) configurations. The DEB fabrication follows the process reported
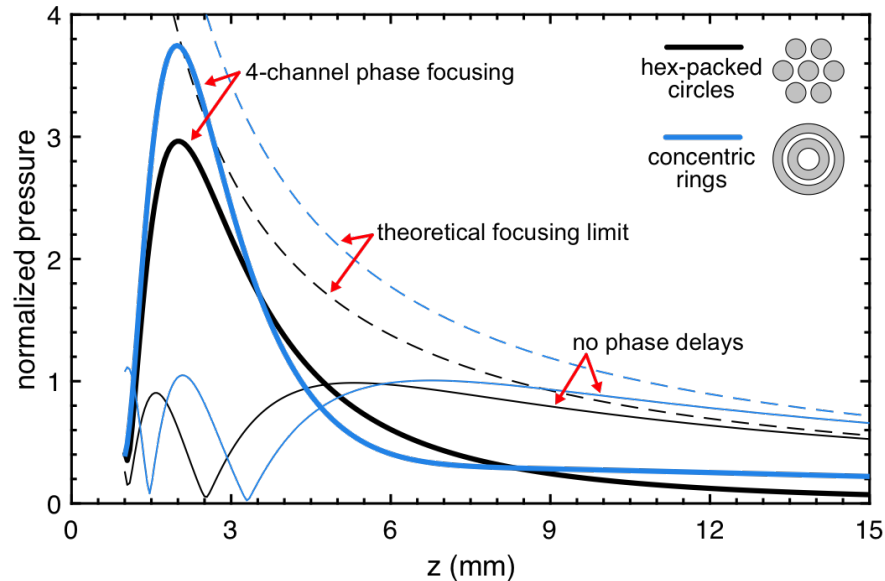
Figure 7.2: Theoretical axial pressure from arrays of concentric rings (blue) and hexagonal-packed circles (black), normalized by $2\rho_a c_a u_0 f_F$. The thin solid curves are for all transducers vibrating in-phase, the dashed curves represent the theoretical focusing limits, and the thick solid curves are calculated for 4-channel phase focusing.

in [25], and is briefly described as follows. A film stack composed of a 175 nm thick aluminum nitride (AlN) seed layer, 130 nm molybdenum (Mo) bottom ground plane, 830 nm active AlN layer, 60 nm SiO_2 barrier, and a 130 nm Mo middle electrode layer is deposited on a silicon (Si) wafer. The middle electrode and SiO_2 are patterned with a SF_6-based plasma etch, followed by a deposition of a 830 nm active AlN layer, 60 nm SiO_2 barrier, and 130 nm top ground Mo layer. The top electrode is patterned with the same SF_6 plasma etch, after which the mid-electrode and bottom-ground vias are etched by Cl_2-based RIE, and finally the PMUT diaphragms are released by a backside through-wafer DRIE process. The DEU fabrication closely mirrors this process, however a silicon-on-insulator wafer with a 1 μm buried oxide layer and 4 μm Si-device layer is utilized, and only the first 175 nm/130 nm/830 nm/60 nm/130 nm stack of AlN/Mo/AlN/SiO_2/Mo is deposited.

Top-view optical micrographs of an example DEB array are presented in Figures 7.3(a) and (b). The footprint of the fabricated arrays is a circle with diameter $2b_{ap} = 3$ mm to be sufficiently small for catheter-based applications, and different numbers of concentric PMUTs are connected in parallel to form 5 channels with approximately equal areas. Artificial dotted lines indicating the boundary of the released PMUT diaphragm are shown in the magnified image in (b), which also displays the dual-electrode PMUT structure. Each transducer has inner and outer electrodes designed for 50% areal coverage; the former is centered on the released diaphragm, and the latter extends inwards from the clamped boundaries. Figure 7.3(c) is a backside optical micrograph,

where the AlN seed layer is blue and indicates the released diaphragm areas, and the Si substrate, which acts as a mechanical anchor for the PMUTs, appears black due to surface roughness. Three radial anchors are also seen in this image, which are designed to increase yield; two copies of each array were fabricated, one with and one without these radial anchors. Especially in the DEB PMUTs which have over 1.7 µm of AlN, the yield was diminished by cracking in the PMUTs during dicing and final cleaning steps. We attribute this to residual stress in the AlN, which was 320 MPa for the DEB design and found to increase with the AlN thickness, causing the PMUTs to become very fragile without radial anchors that provide extra support. The high stresses are most likely due to target contamination within the deposition tool causing defects that propagate and grow as the subsequent AlN is deposited. In contrast, with a relatively sturdy Si device layer, high yield was obtained for the DEU designs both with and without the radial anchors. Cross-section SEM images of the DEB and DEU PMUTs are respectively provided in Figures 7.3(d) and (e) to show their composition and differences. The DEU diaphragm is about twice as thick as its DEB counterpart, and the inner and outer electrodes are patterned in the top Mo layer, whereas they are patterned in the middle Mo layer for the DEB design. The bottom Mo layer is a ground plane for both designs, and both the top and bottom Mo are grounded during operation for the DEB PMUTs.

7.3.2 Prototype Comparison

Three of the fabricated arrays, with designs D1, D2, and D3 as summarized in Table 7.1, were tested to compare their acoustic transmission performance. All three prototypes are composed of ring-shaped PMUTs with a small width of $w_0 = 60$ µm, as our simulations indicate that pressure output increases with resonance frequency, which decreases with w_0. D1 and D2 are DEB designs with radial anchors to address the previously mentioned yield issues, while D3 has a DEU structure without radial anchors. Designs D1 and D2 operate between 2-5 MHz, whereas D3 operates at a higher frequency range of 4-7 MHz due to its relatively thick diaphragm. The prototypes have spacing $\delta = 50$, 100, and 50 µm, so that $N = 11$, 8, and 11 concentric PMUTs fit within the aperture radius $b_{ap} = 1.28$, 1.38, and 1.28 mm for D1, D2, and D3, respectively. While the fabricated arrays have five channels as shown in Figure 7.3(a), the driving electronics used in testing have four outputs; channel 5 is therefore not used, and b_{ap} and N are representative of channels 1 through 4. Figure 7.4(a) provides an optical image of the D1 prototype mounted on a PCB and sealed with epoxy for testing. The acoustic output of the arrays is measured using the setup depicted in Figure 7.4(b). A custom 3D printed sample fixture that also serves as an acoustic tank is filled with mineral oil (not shown), the PMUTs are wired out to be driven by an arbitrary waveform generator (AWG, ArbStudio 1104, Teledyne LeCroy, USA) and the acoustic field is measured with a hydrophone (HGL-0200, Onda Corp., USA) connected to a preamplifier (AH-2010, Onda Corp., USA) that is mounted on an x-y-z stage with manual micrometer control.

The dual-electrode functionality of the fabricated arrays is first verified by measuring the acoustic output from channel 1 on prototype D1. Figure 7.5 shows the receive (Rx) signal from the
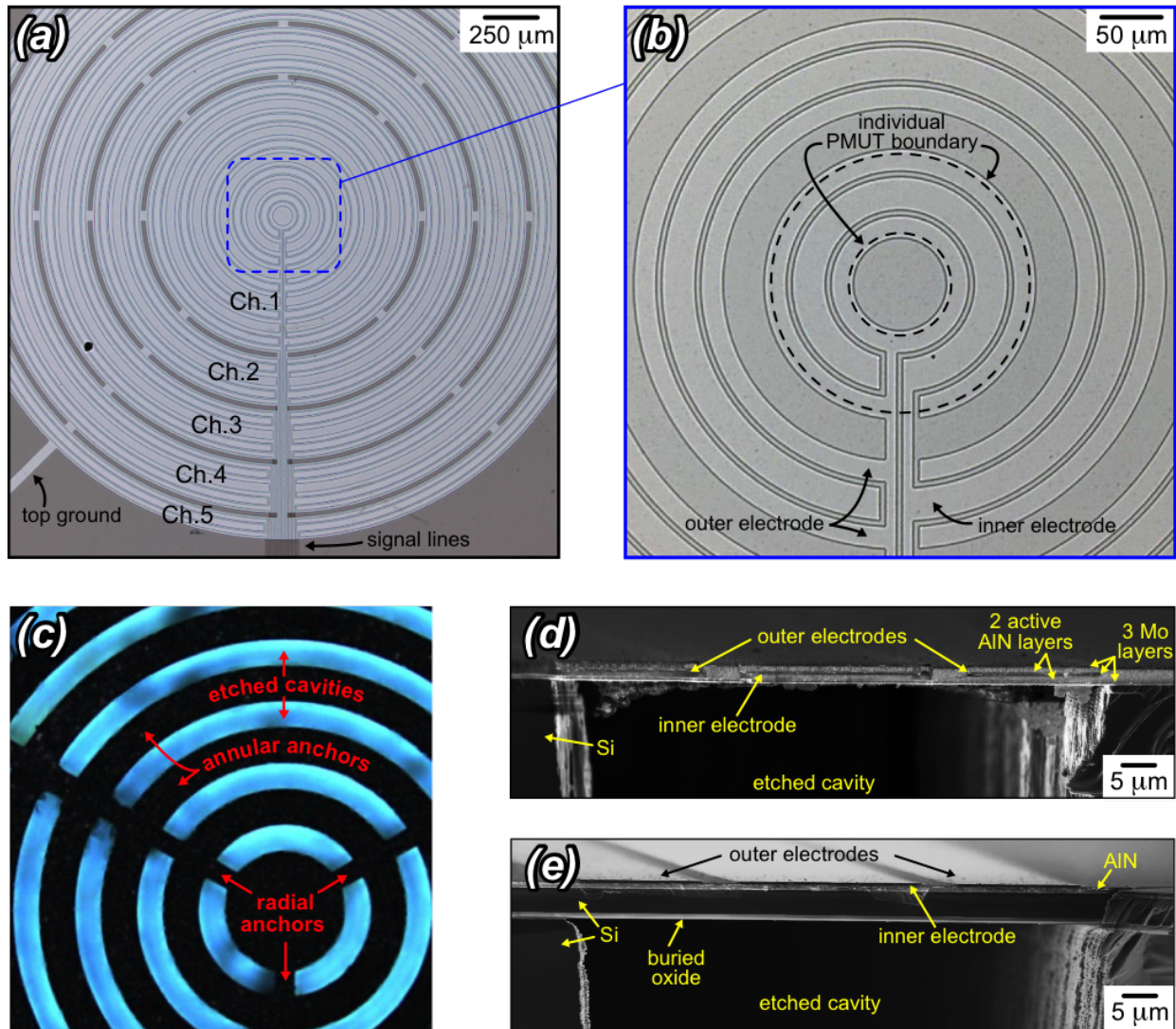
Figure 7.3: Top-view optical micrographs of (a) the full array and (b) the two innermost concentric PMUTs for prototype D1. (c) Backside optical micrograph, showing the radial anchors used for diaphragm support in D1 and D2. Cross-sectional SEM images of the (d) DEB and (e) DEU PMUT designs.

Table 7.1: Specifications of the concentric PMUT arrays fabricated and tested in Section 7.3.

Name	Design	Radial anchors	w_0 (µm)	δ (µm)	N	b_{ap} (mm)
D1	DEB	yes	60	50	11	1.28
D2	DEB	yes	60	100	8	1.38
D3	DEU	no	60	50	11	1.28
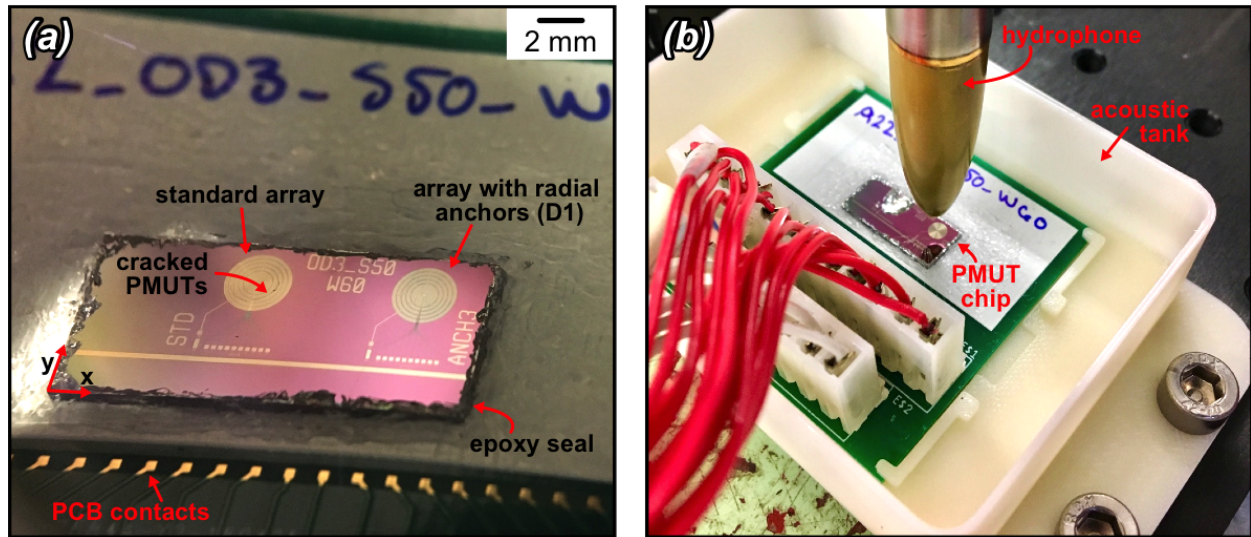
Figure 7.4: (a) PMUT chip with prototype D1 mounted on a custom PCB; (b) experimental setup used to measure the acoustic output of the PMUT arrays.

hydrophone placed at $z = 6.5$ mm and aligned to the center axis of the array when a 1 V_{ac}, 1 cycle, 4 MHz sine pulse is applied to the inner (green curve) and outer (blue curve) electrodes. It is worth noting that single cycle transmit waveforms are used repeatedly in this chapter as broadband excitations that allow for quantities to be calculated over a range of frequencies. As expected, the amplitudes are nearly equal and out-of-phase, implying that the array can be driven differentially in order to increase the output pressure. Indeed, when the inner and outer electrodes are driven simultaneously with the same voltage waveform as before but in a differential configuration (black curve), the hydrophone signal increases in amplitude to the sum of the amplitudes measured by each electrode driven individually, indicating an effective doubling of the pressure generated by the array.

In order to compare their performance, the transmit (Tx) sensitivity S_{Tx}, which we define as the axial output pressure per input volt, of each of the three prototypes is measured. In general, S_{Tx} is a function of both frequency and distance z, however the shape of S_{Tx} is independent of z in the far-field and instead only its magnitude changes with distance. To this end, the transmission of each prototype is measured by placing the hydrophone in the far-field at $z = 8$ mm, and driving the inner electrodes of channels 1-4 with a 1 V_{ac}, 1 cycle, sine pulse as before, but with frequency 4 MHz for D1 and D2 and 5 MHz for D3. The frequency spectrum of the Rx waveform RX is measured by taking the fast Fourier transform (FFT) of the hydrophone signal, and has been shaped not only by S_{Tx}, but also by the hydrophone Rx sensitivity H_{Rx} and the Tx waveform spectrum TX such that

$$RX(z, j\omega) = S_{Tx}(z, j\omega)\, H_{Rx}(j\omega)\, TX(j\omega), \tag{7.6}$$

where $\omega = 2\pi f$ is the angular frequency, and the dependencies of each term are explicitly shown.
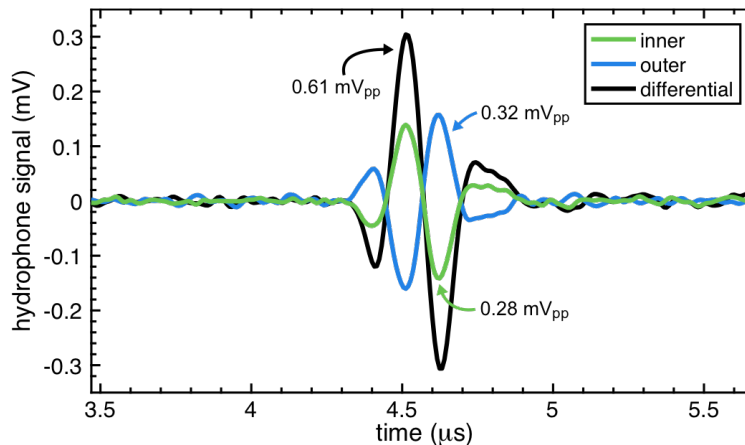
Figure 7.5: Comparison of the pressure pulse from Channel 1 on prototype D1 under different
drive schemes. The pressure generated by driving the inner (green) or outer (blue) electrodes are
out-of-phase and of comparable amplitude, so that the pressure output can be doubled by driving
differentially (black).

Following (7.6), the transmit sensitivity of each array is found by dividing the hydrophone sensi-
tivity and transmit waveform spectrum out from the FFT of the received pulse. Using this process,
S_{Tx} for each of the three prototypes is compared in Figure 7.6(a). The two DEB prototypes D1
and D2 show nearly equal peak pressure output at $1.2-1.3$ kPa/V, despite D2 having a substan-
tially lower fill-factor with larger PMUT spacing and three less concentric transducers than D1.
While perhaps non-intuitive, the fact that pressure output is independent of f_F is consistent with
our modeling presented in Chapter 6, and is a result of PMUT velocity increasing as f_F is reduced.
Instead, the reduction in fill-factor is manifested in S_{Tx} as a drop in 3 dB bandwidth from 4 MHz
for D1 to 2.7 MHz for D2, which is also predicted by our array models.

    In contrast, D3 achieves a high peak pressure output of 2.14 kPa/V despite its unimorph con-
struction with only one active piezoelectric layer. The reason for the increase in pressure relative
to the bimorph prototypes is two-fold: (1) due to its relatively thick diaphragm, D3 exhibits the
highest resonance frequency of all prototypes, which increases the acoustic power transmitted by
the array; and (2) D1 and D2 both have radial anchors, which have minimal impact on resonance
frequency but substantially diminish volume velocity and therefore transmit efficiency. As the pro-
totype with the largest pressure output, the $z-$dependence of the acoustic field generated by D3
is also investigated by repeating the previous measurement process as the hydrophone position is
varied between $z = 1.8$ and 10 mm as shown in Figure 7.6(b). The greatest pressure generated
by the array is 3.2 kPa/V, which occurs at $z = 4$ mm and $f = 4.5$ MHz. In order to compare the
concentric array design to previously reported PMUTs, we introduce a normalized pressure output
p_n as

$$p_n = p \, \frac{\lambda}{V A_{ap} \, e_{31,\mathrm{f}}}, \tag{7.7}$$
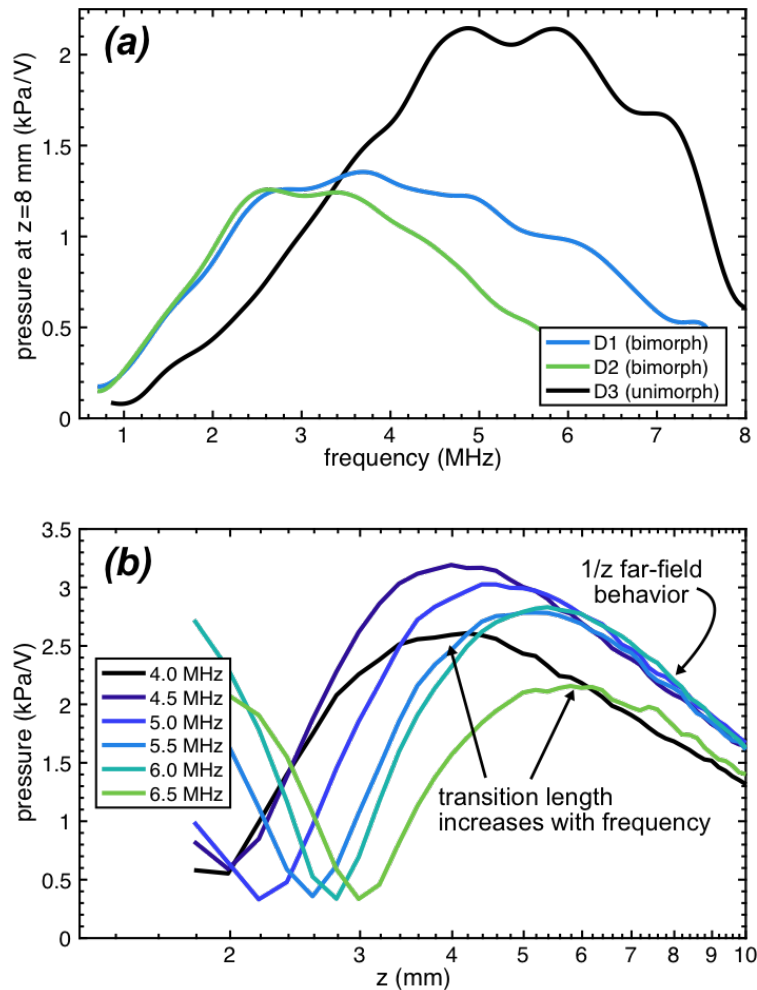
Figure 7.6: (a) Far-field transmit sensitivity for the fabricated prototypes without phase focusing,
(b) axial pressure profile from D3 at frequencies between 4 and 6.5 MHz without phase focusing.

which has units of pressure per area per energy density, and where p is the pressure amplitude, $e_{31,\mathrm{f}}$
is the thin-film piezoelectric constant, and V is the applied voltage as measured from the frequency
spectrum of the Tx waveform at the driving frequency. This definition of voltage is chosen to
account for the effects of the Tx waveform shape; a 1 V square and sine wave with frequency
f_0 have amplitudes of $4/\pi \approx 1.27$ and 1 V at f_0, respectively. While a more commonly reported
normalized pressure is the pressure per area per volt (e.g., [35]), the definition in (7.7) facilitates
comparison between PMUTs having different piezoelectric materials by dividing by $e_{31,\mathrm{f}}$, and
that are tested in various acoustic media by multiplying by λ. Intuition behind this approach to
compensating for the medium can be provided by (7.2) where the far-field pressure is shown to
be inversely proportional to λ, and indeed our simulations indicate that if immersed in FC-70
($c_a = 750\,\mathrm{m/s}$) prototype D3 would output almost twice the pressure as it does in mineral oil.
Using this definition, the normalized pressure measured from several reported high-performance

PMUT arrays are provided in Table 7.2, where the piezoelectric constants of AlN, ScAlN, and
PZT are assumed as $e_{31,f} = 1$, 1.6, and 14 C/m^2, respectively [33], [35]. Prototype D3 shows a
normalized pressure of $p_n = 184$ kPa/mm^2/(J cm^{-3}), which is the highest reported value among
PMUTs without focusing.

Furthermore, Figure 7.6(b) shows distinct near-field and far-field regions with the expected
oscillatory and slowly decaying pressure trends, respectively. The existence of the near-field is
particularly important, as it denotes destructive interference between the channels in the array and
phase-focusing is therefore limited to this region. One way to characterize the transition between
the near and far-field regions is the location of the last local maximum z^*; for a piston radiator with
area A_{ap}, this maximum occurs at $z^* = A_{ap}/\pi\lambda$, which leads to a predicted value of $z^* = 4.9$ mm
that is close to the measured value of 4 mm. The minor discrepancy is due to velocity phase
variations among the PMUTs in the array, caused by a combined effect of the unequal-length
electrical lines and the acoustic interactions between PMUTs, however the predicted behavior of
z^* increasing with frequency is observed.

7.3.3   Phased Array Focusing

The nature of the near-field interference is explicitly shown in Figure 7.7(a), which presents the
measured Rx signal from the hydrophone placed at $z = 2.9$ mm as each channel is driven inde-
pendently. The pressure pulse generated by Channel 1 arrives first and each subsequent channel
has an incrementally longer time-of-flight (ToF), so that when all channels are driven in unison
the resulting pressure amplitude is low. This also reveals the mechanism by which phased-array
focusing works: if Channel 4 were fired first, instead, and Channels 3 through 1 were each de-
layed by their corresponding ToF offset, then the pressures from all 4 channels would interfere
constructively and the resulting pressure would be boosted significantly.

Figure 7.7(b) presents the results of phase focusing with each channel driven by a 1 V$_{ac}$, 1
cycle, 5 MHz sine pulse with a time delay determined by the measured ToF offset as described
above, with all quantities calculated at 6 MHz. The black curve represents driving all channels
in unison (i.e., no focusing or time delays) and reaches a maximum pressure of $p_{nf} = 2.8$ kPa;
focusing at 2.9 mm (green curve) boosts the maximum pressure to $p_f = 10$ kPa by using time
delays of 128, 88, 48, and 0 ns for channels 1-4, respectively; and focusing at 1.9 mm (blue curve)
achieves a pressure of $p_f = 12.23$ kPa with time delays of 196, 136, 72, and 0 ns for channels
1-4, respectively. It is worth noting that the utilized time delays are similar to the theoretically
predicted values in (7.5), but are slightly different due to velocity phase variations caused by the
same effects that produce errors in the far-field length estimates. On the other hand, with focusing
at $z_f = 1.9$ mm, the normalized pressure is the highest among all reported phased PMUT arrays as
shown in Table 7.2. The axial pressure distribution also shows a strong agreement with simulations
for a 3 dB focal length of 1.2 mm, indicating that high pressures are confined to the expected

region. This is further confirmed in Figure 7.7(c), which shows the x and $y-$direction beam patterns at 6 MHz in the focal plane $z_f = 1.9$ mm as measured by collecting data at multiple hydrophone locations. The two measured beam patterns are nearly identical due to the annular symmetry of the array, and also agree well with simulations to predict a narrow 3 dB beamwidth of 235 µm. Sidelobes exist near ± 380 µm, however their pressure amplitude is below -14 dB and their effects are therefore expected be minimal.

While the data in Figures 7.7(a)-(c) pertain to D3, similar experimental efforts were performed on D1 and D2 for a broader evaluation of the efficacy of focusing using concentric PMUT arrays. As most applications that utilize phase-focusing require a threshold time-averaged acoustic intensity $I = p^2/2\rho_a c_a$, we define the focusing gain $G_f = (p_f/p_{nf})^2$ as the square of the ratio of the focal pressure to the maximum pressure achieved without focusing. The focusing gains measured with each of the three prototypes at different frequencies and focal depths are shown in Figure 7.7(d), along with dotted lines representing the theoretical gain as determined by (7.3). The measured gain has a general trend of increasing with frequency, which is consistent with the expectation that focusing improves as kb_{ap} increases, and is comparable with the theoretical value. Especially at higher frequencies, however, the measured G_f is larger than expected. This is likely due to velocity phase variations among the PMUTs in the no-focusing case reducing the pressure output by the array, whereas the theoretical value assumes all PMUTs vibrate in-phase. Nonetheless, the focusing gain is measured to be as high as 19 and 12.2 at 6 MHz for D3 focused at $z_f = 1.9$ and 2.9 mm, respectively. Compared with the previous reports in Table 7.2, these high values of G_f are due to the high-quality and 2-dimensional focusing that are inherent to annular arrays.

Even with effective acoustic focusing, arrays need to be driven with more than 1 V_{ac} to generate high acoustic intensities. To confirm that the pressure output scales with input voltage as predicted, the focal pressure from D3 driven with a variable-amplitude, 5 cycle, 6 MHz square wave pulse and with focusing delays for $z_f = 1.9$ mm is provided in Figure 7.8. Also plotted is the expected pressure output (blue curve), as scaled from the peak pressure in Figure 7.7(b). The two data show nearly perfect agreement, verifying that the concentric PMUT array acts as a linear transducer, and predicting a peak-to-peak pressure of 187 kPa, which corresponds to a time-averaged intensity of 0.34 W/cm^2, at the maximum voltage of the waveform generator 12 V_{pp}. This is promising for many high-intensity applications including catheter-based HIFU, as it suggests that an intensity of 1 W/cm^2 could be achieved with only 20 V_{pp} applied, which exceeds the intensity needed for some medical operations [104]. The voltage could also be further reduced, or the intensity further increased, if an 8-channel Tx circuit were available to enable a differential drive scheme that leverages the dual-electrode PMUT structure.

Table 7.2: Comparison of high-performance PMUT arrays with strong acoustic output.

Piezo Material	Medium	f (MHz)	Transmit Voltage	No Focusing		With Focusing		Focusing Gain G_f
				p (kPa)	p_n $\left(\frac{\text{kPa mm}^{-2}}{\text{J cm}^{-3}}\right)$	p (kPa)	p_n $\left(\frac{\text{kPa mm}^{-2}}{\text{J cm}^{-3}}\right)$	
AlN [35]	FC-70	9	25 V_{pp} sq.	3	50			
ScAlN [35]	FC-70	9	11 V_{pp} sq.	4	124			
PZT [38]	FC-70	10	18 V_{pp} sq.	75	72	225	217	9
AlN [34]	FC-70	8	18 V_{pp} sq.	13	165	40	496	9
AlN (this work)	mineral oil	4.5 / 6	1 V_{ac} sine	3.2	184	12.2	588	19

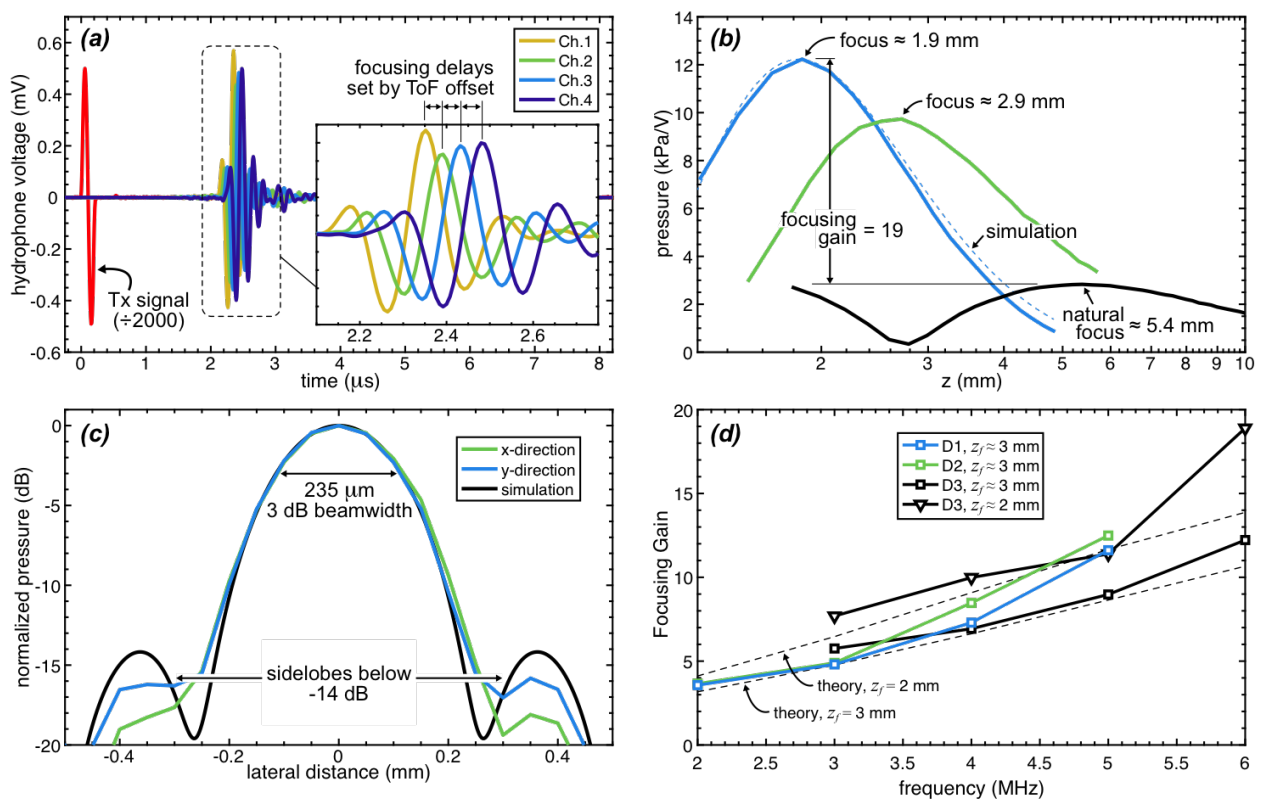**Figure 7.7:** Phased array focusing results for D3. (a) Pressure pulse from each channel, showing consecutively delayed arrivals. (b) Axial pressure comparison without focusing (black), and with phase focusing set to 3 mm (green) and 2 mm (blue). (c) Beam pattern in the x (green) and y (blue) directions in the focal plane for $z_f = 2$ mm. (d) Focusing gain for all tested prototypes, focusing distances, and frequencies.
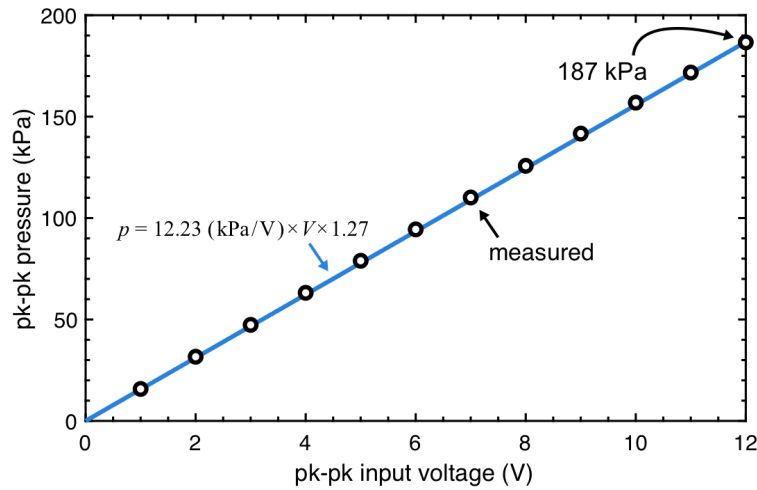
Figure 7.8: Measured pressure from D3 at focus $z_f = 2$ mm and different driving voltage amplitudes. The focal pressure scales as expected, reaching a maximum of 187 kPa at 12 V_{pp}.

7.4   Conclusion

This chapter proposes a concentric array of ring-shaped PMUTs for applications of ultrasound that require high acoustic intensities. Advantages associated with the annular array, including high pressure output using standard driving voltages and effective focusing via phased array operation, are explained using intuitive and theoretical arguments. Prototype arrays having both the usual DEU and high-performance DEB structures are fabricated using standard AlN microfabrication techniques, with small footprints that can be used in catheter-based ultrasound systems. While having a potential for greater pressure generation, the DEB arrays showed a lower performance than their DEU counterparts due to low operation frequencies and the need to introduce radial anchors for yield improvement. On the other hand, the DEU prototype exhibited an output pressure as high as 3.2 kPa/V in standard transmission, which was boosted to 12.2 kPa/V by applying phased array focusing at a depth of 2 mm. Furthermore, a linear relationship between focal pressure and applied voltage was observed for the full range of voltages allowed by our testing equipment, with a maximum measured pressure of 187 kPa peak-to-peak. With the expected linear operation range to extend well beyond this, the fabricated concentric PMUT arrays show feasibility to reach the intensity ranges required for medical operations. Furthermore, while the small footprint of the arrays tested here was chosen for relevancy in catheter systems, this work also indicates that concentric ring-shaped PMUT arrays would be useful in other fields, such was wireless power transfer and nondestructive testing.

Chapter 8

Conclusions and Future Works

8.1   Conclusions

This dissertation presents research on enhancing the performance of piezoelectric micromachined ultrasonic transducers (PMUTs) by devising and analyzing design improvements, and using these findings to demonstrate PMUT-based systems with improved capabilities. The ring-shaped PMUT is firstly introduced as a novel transducer architecture with several straightforward benefits, including increased pressure output and the ability to separately tune frequency and aperture size. An in-depth investigation of the dynamics of this design is presented through the development of an equivalent circuit model that relates the mechanical, electrical, and acoustical physical domains within a concise and easy to understand framework. This model is extensively validated with finite element simulations, and can be used to help optimize electrode layouts and reveal the benefits of the ring-shaped structure, such as improved electromechanical coupling compared to circular PMUTs. The model is also instrumental in explaining the cause of the broadband response exhibited by aptly designed ring-shaped PMUTs in liquid immersion, which is demonstrated to be an acoustically induced resonance. This behavior of fluctuations in acoustic impedance producing specific changes in transducer velocities has not been observed prior to this dissertation research, and demonstrates that design improvements need not be limited in scope to mechanical or material considerations as have been traditionally explored.

Aside from PMUTs operating as standalone transducers, array implementations have also been leveraged in this research. Arrays of bimorph PMUTs were used to demonstrate a single-chip flow sensor with differential readout, which derives its high sensitivity from spatially distinct transmitting and receiving PMUT elements. The appeal of this design also lies in its simplicity, as the single-chip package promises low power consumption and a small form-factor that should make for straightforward implementation, thereby promoting its widespread adoption. The fusion of the bimorph and ring-shaped PMUT design concepts, which both offer increased acoustic output,

is presented by proposing high-power arrays of concentric ring-shaped PMUTs. Such arrays are first explored analytically by developing an equivalent circuit network model that can predict the array performance by accounting for the acoustic coupling between PMUTs. Simple design equations are derived from this network model that reveal interesting phenomenon and help identify important layout considerations. Such details help guide the design of concentric PMUT arrays aimed at generating high acoustic intensities, which are fabricated with small footprints and combined with highly effective phased array acoustic focusing in order to demonstrate feasibility for catheter-based medical operations.

8.2 Future Works

Engineering efforts on PMUTs in our lab were initiated with the doctoral work of Sina Akhbari [105] and continued in this dissertation research. While many advances were made in the process, there remain an abundance of future directions to take this work within the rich field of PMUT innovation. As mentioned within Chapter 5, there are several interesting extensions presented by the flow sensor proposed in this work. The operating principle that was proven in the course of the sensor development is powerful and flexible, and could be readily adopted in two-dimensional flow measurement or serve as the foundation for a tilt sensor. In regards to the ring-shaped PMUT, the broad-band behavior could be leveraged to develop harmonic imaging systems with enhanced image contrast. Perhaps an even more promising route that is the most uniquely suited for PMUTs is to continue the development of catheter-based medical HIFU probes. While the initial findings presented here show strong potential in this realm, improving the stress-control in AlN deposition would enable high-yield DEB PMUTs with thicker diaphragms for higher resonance frequencies than those demonstrated here, and should drastically increase the generated acoustic intensities. Such improvements would also be furthered by adopting new materials with higher transduction efficiency such as ScAlN or PZT. With strong results, imaging PMUT elements could also be integrated in order to demonstrate an all-in-one ultrasound solution for HIFU operations with real-time monitoring.

Bibliography

[1]   World Health Organization. "Training in diagnostic ultrasound: essentials, principles and standards: report of a WHO study group". In: (1998).

[2]   B.W. Drinkwater and P.D. Wilcox. "Ultrasonic arrays for non-destructive evaluation: A review". In: *Ndt & E International* 39.7 (2006), pp. 525–541.

[3]   C. Biber et al. "The polaroid ultrasonic ranging system". In: *Audio Engineering Society Convention 67*. Audio Engineering Society. 1980.

[4]   D.L Miller et al. "Overview of therapeutic ultrasound applications and safety considerations". In: *Journal of Ultrasound in Medicine* 31.4 (2012), pp. 623–634.

[5]   C. Rubin et al. "The use of low-intensity ultrasound to accelerate the healing of fractures". In: *JBJS* 83.2 (2001), p. 259.

[6]   G.S. Kino. *Acoustic waves: devices, imaging, and analog signal processingPrentice-Hall Signal Processing Series*. Englewood Cliffs, Prentice-Hall, 1987.

[7]   J.F. Dias. "Construction and performance of an experimental phased array acoustic imaging transducer". In: *Ultrasonic imaging* 3.4 (1981), pp. 352–368.

[8]   T.L. Szabo. *Diagnostic ultrasound imaging: inside out*. Academic Press, 2004.

[9]   S.W. Smith, G.E. Trahey, and O.T. Von Ramm. "Two-dimensional arrays for medical ultrasound". In: *Ultrasonic Imaging* 14.3 (1992), pp. 213–233.

[10] B.T. Khuri-Yakub, O. Oralkan, and M. Kupnik. "Next-gen ultrasound". In: *IEEE Spectrum* 46.5 (2009).

[11] D.A. Horsley et al. "Piezoelectric micromachined ultrasonic transducers in consumer electronics: The next little thing?" In: *Micro Electro Mechanical Systems (MEMS), 2016 IEEE 29th International Conference on*. IEEE. 2016, pp. 145–148.

[12] P.C. Eccardt, K. Niederer, and B. Fischer. "Micromachined transducers for ultrasound applications". In: *Ultrasonics Symposium, 1997. Proceedings., 1997 IEEE*. Vol. 2. IEEE. 1997, pp. 1609–1618.

[13] R. Przybyla et al. "An ultrasonic rangefinder based on an AlN piezoelectric micromachined ultrasound transducer". In: *Sensors, 2010 IEEE*. IEEE. 2010, pp. 2417–2421.

[14] X. Jiang et al. "Monolithic 591× 438 DPI ultrasonic fingerprint sensor". In: *Micro Electro Mechanical Systems (MEMS), 2016 IEEE 29th International Conference on*. IEEE. 2016, pp. 107–110.

[15] B.T. Khuri-Yakub and Ö. Oralkan. "Capacitive micromachined ultrasonic transducers for medical imaging and therapy". In: *Journal of micromechanics and microengineering* 21.5 (2011), p. 054004.

[16] P. Muralt et al. "Piezoelectric micromachined ultrasonic transducers based on PZT thin films". In: *IEEE transactions on ultrasonics, ferroelectrics, and frequency control* 52.12 (2005), pp. 2276–2288.

[17] G.G. Yaralioglu et al. "Calculation and measurement of electromechanical coupling co-efficient of capacitive micromachined ultrasonic transducers". In: *IEEE transactions on ultrasonics, ferroelectrics, and frequency control* 50.4 (2003), pp. 449–456.

[18] S. Machida et al. "Highly reliable CMUT cell structure with reduced dielectric charging effect". In: *Ultrasonics Symposium (IUS), 2015 IEEE International*. IEEE. 2015, pp. 1–4.

[19] R.J. Przybyla et al. "In-air rangefinding with an AlN piezoelectric micromachined ultra-sound transducer". In: *IEEE Sensors Journal* 11.11 (2011), pp. 2690–2697.

[20] F. Sammoura and S.-G. Kim. "Theoretical modeling and equivalent electric circuit of a bimorph piezoelectric micromachined ultrasonic transducer". In: *IEEE transactions on ultrasonics, ferroelectrics, and frequency control* 59.5 (2012).

[21] J. Song et al. "Capacitive micromachined ultrasonic transducers (CMUTs) for underwater imaging applications". In: *Sensors* 15.9 (2015), pp. 23205–23217.

[22] Y. Lu et al. "Broadband piezoelectric micromachined ultrasonic transducers based on dual resonance modes". In: *Proc. IEEE MEMS*. 2015, pp. 146–149.

[23] T. Wang, T. Kobayashi, and C. Lee. "Micromachined piezoelectric ultrasonic transducer with ultra-wide frequency bandwidth". In: *Applied Physics Letters* 106.1 (2015), p. 013501.

[24] A. Hajati et al. "Three-dimensional micro electromechanical system piezoelectric ultra-sound transducer". In: *Applied Physics Letters* 101.25 (2012), p. 253101.

[25] S. Akhbari et al. "Bimorph piezoelectric micromachined ultrasonic transducers". In: *Journal of Microelectromechanical Systems* 25.2 (2016), pp. 326–336.

[26] H-Y. Tang. *Interface Electronics for Ultrasonic Transducers*. University of California, Berkeley, 2016.

[27] S. Akhbari et al. "Highly responsive curved aluminum nitride pMUT". In: *Micro Electro Mechanical Systems (MEMS), 2014 IEEE 27th International Conference on*. IEEE. 2014, pp. 124–127.

[28] S. Akhbari et al. "Self-curved diaphragms by stress engineering for highly responsive pMUT". In: *Micro Electro Mechanical Systems (MEMS), 2015 28th IEEE International Conference on*. IEEE. 2015, pp. 837–840.

[29] L. Lou et al. "Comparative characterization of bimorph and unimorph AlN piezoelectric micro-machined ultrasonic transducers". In: *Micro Electro Mechanical Systems (MEMS), 2016 IEEE 29th International Conference on*. IEEE. 2016, pp. 1090–1093.

[30] G-L. Luo et al. "Increased Output-Pressure PMUTs with a Sloped Profile Fabricated via Surface Micromachining". In: ().

[31] S. Akhbari et al. "Dual-electrode bimorph PMUT arrays for handheld therapeutic medical devices". In: *Micro Electro Mechanical Systems (MEMS), 2016 IEEE 29th International Conference on*. IEEE. 2016, pp. 1102–1105.

[32] Y. Lu, A. Heidari, and D.A. Horsley. "A high fill-factor annular array of high frequency piezoelectric micromachined ultrasonic transducers". In: *Journal of Microelectromechanical Systems* 24.4 (2015), pp. 904–913.

[33] X. Jiang et al. "Ultrasonic fingerprint sensor with transmit beamforming based on a PMUT array bonded to CMOS circuitry". In: *IEEE transactions on ultrasonics, ferroelectrics, and frequency control* 64.9 (2017), pp. 1401–1408.

[34] Y. Lu et al. "Pulse-echo ultrasound imaging using an AlN piezoelectric micromachined ultrasonic transducer array with transmit beam-forming". In: *Journal of Microelectromechanical Systems* 25.1 (2016), pp. 179–187.

[35] Q. Wang et al. "Design, fabrication, and characterization of scandium aluminum nitride-based piezoelectric micromachined ultrasonic transducers". In: *Journal of Microelectromechanical Systems* 26.5 (2017), pp. 1132–1139.

[36] Y. Lu, Q. Wang, and D.A. Horsley. "Piezoelectric micromachined ultrasonic transducers with increased coupling coefficient via series transduction". In: *Ultrasonics Symposium (IUS), 2015 IEEE International*. IEEE. 2015, pp. 1–4.

[37] K.M. Smyth. "Design and modeling of PZT thin film piezoelectric micromachined ultrasonic transducer (PMUT)". M.S. Thesis. Cambridge: Massachusetts Institute of Technology, 2012.

[38] Y. Lu and D.A. Horsley. "Modeling, fabrication, and characterization of piezoelectric micromachined ultrasonic transducer arrays based on cavity SOI wafers". In: *Journal of Microelectromechanical Systems* 24.4 (2015), pp. 1142–1149.

[39] Q-H. Qin. *Advanced mechanics of piezoelectricity*. Springer Science & Business Media, 2012.

[40] S. Akhbari et al. "Bimorph pMUT with dual electrodes". In: *Micro Electro Mechanical Systems (MEMS), 2015 28th IEEE International Conference on*. IEEE. 2015, pp. 928–931.

[41] Y. Qiu et al. "Piezoelectric micromachined ultrasound transducer (PMUT) arrays for integrated sensing, actuation and imaging". In: *Sensors* 15.4 (2015), pp. 8020–8041.

[42] M. Wasilik and A.P. Pisano. "Low-frequency process for silicon-on-insulator deep reactive ion etching". In: *Device and Process Technologies for MEMS and Microelectronics II*. Vol. 4592. International Society for Optics and Photonics. 2001, pp. 462–473.

[43] S. Akhbari, F. Sammoura, and L. Lin. "Equivalent circuit models for large arrays of curved and flat piezoelectric micromachined ultrasonic transducers". In: *IEEE transactions on ultrasonics, ferroelectrics, and frequency control* 63.3 (2016), pp. 432–447.

[44] Q. Wang and D.A. Horsley. "Using a mutual acoustic impedance model to improve the time domain response of PMUT arrays". In: *Ultrasonics Symposium (IUS), 2017 IEEE International*. IEEE. 2017, pp. 1–4.

[45] K.M. Smyth, C.G. Sodini, and S-G. Kim. "High electromechanical coupling piezoelectric micro-machined ultrasonic transducer (PMUT) elements for medical imaging". In: *Solid-State Sensors, Actuators and Microsystems (TRANSDUCERS), 2017 19th International Conference on*. IEEE. 2017, pp. 966–969.

[46] F. Akasheh et al. "Piezoelectric micromachined ultrasonic transducers: Modeling the influence of structural parameters on device performance". In: *IEEE Trans. Ultrason. Ferroelectr. Freq. Control* 52.3 (2005), pp. 455–468.

[47] Q. Xu et al. "Piezoelectric Micromachined Ultrasonic Transducers for Photoacoustic Imaging: Modeling and Simulation of Structural Parameters on Receive Performance". In: *X-Acoustics: Imaging and Sensing* 1.1 (2015).

[48] J.L. Butler and C.H. Sherman. *Transducers and arrays for underwater sound*. Springer, 2016.

[49] S. Shelton et al. "Improved acoustic coupling of air-coupled micromachined ultrasonic transducers". In: *Micro Electro Mechanical Systems (MEMS), 2014 IEEE 27th International Conference on*. IEEE. 2014, pp. 753–756.

[50] K. Smyth and S.-G. Kim. "Experiment and simulation validated analytical equivalent circuit model for piezoelectric micromachined ultrasonic transducers". In: (2015).

[51] K. Smyth et al. "Analytic solution for N-electrode actuated piezoelectric disk with application to piezoelectric micromachined ultrasonic transducers". In: *IEEE transactions on ultrasonics, ferroelectrics, and frequency control* 60.8 (2013), pp. 1756–1767.

[52] F. Sammoura et al. "An analytical analysis of the sensitivity of circular piezoelectric micromachined ultrasonic transducers to residual stress". In: *Ultrasonics Symposium (IUS), 2012 IEEE International*. IEEE. 2012, pp. 580–583.

[53] F. Sammoura et al. "An accurate equivalent circuit for the clamped circular multiple-electrode PMUT with residual stress". In: *Ultrasonics Symposium (IUS), 2013 IEEE International*. IEEE. 2013, pp. 275–278.

[54] J. Cho et al. "Optimization of electromechanical coupling for a thin-film PZT membrane: I. Modeling". In: *Journal of Micromechanics and Microengineering* 15.10 (2005), p. 1797.

[55] HS Choi et al. "A two-dimensional electromechanical composite plate model for piezoelectric micromachined ultrasonic transducers (pMUTs)". In: *Journal of Micromechanics and Microengineering* 20.1 (2009), pp. 1–12.

[56] F. Sammoura, S. Akhbari, and L. Lin. "An analytical solution for curved piezoelectric micromachined ultrasonic transducers with spherically shaped diaphragms". In: *IEEE transactions on ultrasonics, ferroelectrics, and frequency control* 61.9 (2014), pp. 1533–1544.

[57] S. Akhbari, F. Sammoura, and L. Lin. "An equivalent circuit model for curved piezoelectric micromachined ultrasonic transducers with spherical-shape diaphragms". In: *Ultrasonics Symposium (IUS), 2014 IEEE International*. IEEE. 2014, pp. 301–304.

[58] S. Shelton et al. "CMOS-compatible AlN piezoelectric micromachined ultrasonic transducers". In: *Ultrasonics Symposium (IUS), 2009 IEEE International*. IEEE. 2009, pp. 402–405.

[59] F. Sammoura et al. "A two-port piezoelectric micromachined ultrasonic transducer". In: *Applications of Ferroelectrics, International Workshop on Acoustic Transduction Materials and Devices & Workshop on Piezoresponse Force Microscopy (ISAF/IWATMD/PFM), 2014 Joint IEEE International Symposium on the*. IEEE. 2014, pp. 1–4.

[60] E. Ventsel and T. Krauthammer. *Thin plates and shells*. Marcel Dekker New York, 2001.

[61] M. Amabili, G. Frosali, and M.K. Kwak. "Free vibrations of annular plates coupled with fluids". In: *Journal of sound and vibration* 191.5 (1996), pp. 825–846.

[62] A.W. Leissa. *Vibration of plates*. Tech. rep. Ohio State University, Columbus, 1969.

[63] W.P. Rdzanek and Z. Engel. "Asymptotic formulas for the acoustic power output of a clamped annular plate". In: *Applied Acoustics* 60.1 (2000), pp. 29–43.

[64] J.N. Reddy. *Theory and analysis of elastic plates and shells*. CRC press, 2006.

[65] H.F. Tiersten. "Hamilton's principle for linear piezoelectric media". In: *Proceedings of the IEEE* 55.8 (1967), pp. 1523–1524.

[66] H.F. Tiersten. *Linear piezoelectric plate vibrations. 1969*.

[67] D.J. Leo. *Engineering analysis of smart material systems*. John Wiley & Sons, 2007.

[68] M. Lee and R. Singh. "Analytical formulations for annular disk sound radiation using structural modes". In: *The Journal of the Acoustical Society of America* 95.6 (1994), pp. 3311–3323.

[69] W.P. Rdzanek and W.J. Rdzanek. "Asymptotic formulas for the acoustic radiation impedance of an elastically supported annular plate". In: *Journal of Sound and Vibration* 301.3-5 (2007), pp. 544–559.

[70] A.S. Merriweather. "Acoustic radiation impedance of a rigid annular ring vibrating in an infinite rigid baffle". In: *Journal of Sound and Vibration* 10.3 (1969), pp. 369–379.

[71] C.J. Bouwkamp. "Numerical computation of the radiation impedance of a rigid annular ring vibrating in an infinite plane rigid baffle". In: *Journal of Sound and Vibration* 17.4 (1971), pp. 499–508.

[72] D.N. Stephens et al. "First in vivo use of a capacitive micromachined ultrasound transducer array–based imaging and ablation catheter". In: *Journal of Ultrasound in Medicine* 31.2 (2012), pp. 247–256.

[73] Y. Lu et al. "High frequency piezoelectric micromachined ultrasonic transducer array for intravascular ultrasound imaging". In: *Micro Electro Mechanical Systems (MEMS), 2014 IEEE 27th International Conference on*. IEEE. 2014, pp. 745–748.

[74] J. Jung et al. "Fabrication of a two-dimensional piezoelectric micromachined ultrasonic transducer array using a top-crossover-to-bottom structure and metal bridge connections". In: *Journal of Micromechanics and Microengineering* 23.12 (2013), p. 125037.

[75] L.C. Lynnworth and Y. Liu. "Ultrasonic flowmeters: Half-century progress report, 1955–2005". In: *Ultrasonics* 44 (2006), e1371–e1378.

[76] D. Han, S. Kim, and S. Park. "Two-dimensional ultrasonic anemometer using the directivity angle of an ultrasonic sensor". In: *Microelectronics Journal* 39.10 (2008), pp. 1195–1199.

[77] M.I. Haller and B.T. Khuri-Yakub. "A surface micromachined electrostatic ultrasonic air transducer". In: *IEEE transactions on ultrasonics, ferroelectrics, and frequency control* 43.1 (1996), pp. 1–6.

[78] M.S. Salim et al. "Capacitive micromachined ultrasonic transducers: technology and application". In: *Journal of Medical Ultrasound* 20.1 (2012), pp. 8–31.

[79] B.E. Eovino, S. Akhbari, and L. Lin. "Broadband ring-shaped PMUTs based on an acoustically induced resonance". In: *Micro Electro Mechanical Systems (MEMS), 2017 IEEE 30th International Conference on*. IEEE. 2017, pp. 1184–1187.

[80] G.T. Bui, Y-T. Jiang, and D-C. Pang. "Two Capacitive Micro-Machined Ultrasonic Transducers for Wind Speed Measurement". In: *Sensors* 16.6 (2016), p. 814.

[81] D.L. Miller et al. "Overview of therapeutic ultrasound applications and safety considerations". In: *Journal of Ultrasound in Medicine* 31.4 (2012), pp. 623–634.

[82] C. Rubin et al. "The use of low-intensity ultrasound to accelerate the healing of fractures". In: *JBJS* 83.2 (2001), p. 259.

[83] D.N. Stephens et al. "10 MHz catheter-based annular array for thermal strain guided intramural cardiac ablations". In: *Ultrasonics Symposium (IUS), 2015 IEEE International*. IEEE. 2015, pp. 1–4.

[84] J.E. Zimmer et al. "The feasibility of using ultrasound for cardiac ablation". In: *IEEE Transactions on Biomedical Engineering* 42.9 (1995), pp. 891–897.

[85] W.A. N'Djin et al. "Capacitive Micromachined Ultrasound Transducers for Interstitial High-Intensity Ultrasound Therapies". In: *IEEE transactions on ultrasonics, ferroelectrics, and frequency control* 64.8 (2017), pp. 1245–1260.

[86] M.N. Senlik et al. "Radiation impedance of an array of circular capacitive micromachined ultrasonic transducers". In: *IEEE transactions on ultrasonics, ferroelectrics, and frequency control* 57.4 (2010).

[87] F.Y. Yamaner et al. "High-power CMUTs: design and experimental verification". In: *IEEE transactions on ultrasonics, ferroelectrics, and frequency control* 59.6 (2012), pp. 1276–1284.

[88] H.K. Oguz, A. Atalar, and H. Köymen. "Equivalent circuit-based analysis of CMUT cell dynamics in arrays". In: *IEEE transactions on ultrasonics, ferroelectrics, and frequency control* 60.5 (2013), pp. 1016–1024.

[89] J.A. Brown, C.E.M. Demore, and G.R. Lockwood. "Design and fabrication of annular arrays for high-frequency ultrasound". In: *IEEE transactions on ultrasonics, ferroelectrics, and frequency control* 51.8 (2004), pp. 1010–1017.

[90] S.H Wong et al. "Capacitive micromachined ultrasonic transducers for therapeutic ultrasound applications". In: *IEEE transactions on Biomedical Engineering* 57.1 (2010), pp. 114–123.

[91] S. Na et al. "Design and fabrication of a high-power air-coupled capacitive micromachined ultrasonic transducer array with concentric annular cells". In: *IEEE Transactions on Electron Devices* 64.11 (2017), pp. 4636–4643.

[92] C. Bayram et al. "Bandwidth improvement in a cMUT array with mixed sized elements". In: *Proceedings-IEEE Ultrasonics Symposium*. Vol. 4. 2005, pp. 1956–1959.

[93] S. Olcum, M.N. Senlik, and A. Atalar. "Optimization of the gain-bandwidth product of capacitive micromachined ultrasonic transducers". In: *IEEE transactions on ultrasonics, ferroelectrics, and frequency control* 52.12 (2005), pp. 2211–2219.

[94] A. Atalar, H. Köymen, and H.K. Oğuz. "Rayleigh–Bloch waves in CMUT arrays". In: *IEEE transactions on ultrasonics, ferroelectrics, and frequency control* 61.12 (2014), pp. 2139–2148.

[95] A. Caronti et al. "Acoustic coupling in capacitive microfabricated ultrasonic transducers: Modeling and experiments". In: *IEEE transactions on ultrasonics, ferroelectrics, and frequency control* 52.12 (2005), pp. 2220–2234.

[96] H. Lee et al. "Effects of mutual impedance on the radiation characteristics of transducer arrays". In: *The Journal of the Acoustical Society of America* 115.2 (2004), pp. 666–679.

[97] B.W. Drinkwater and P.D. Wilcox. "Ultrasonic arrays for non-destructive evaluation: A review". In: *Ndt & E International* 39.7 (2006), pp. 525–541.

[98] S. Surappa, M. Tao, and L.F. Degertekin. "Analysis and Design of Capacitive Parametric Ultrasonic Transducers for Efficient Ultrasonic Power Transfer Based on a 1D Lumped Model". In: *IEEE transactions on ultrasonics, ferroelectrics, and frequency control* (2018).

[99] S.H. Wong et al. "Advantages of Capacitive Micromachined Ultrasonics Transducers (CMUTs) for High Intensity Focused Ultrasound (HIFU)". In: *Ultrasonics Symposium, 2007. IEEE*. IEEE. 2007, pp. 1313–1316.

[100] C. Fan et al. "A comparison between ultrasonic array beamforming and super resolution imaging algorithms for non-destructive evaluation". In: *Ultrasonics* 54.7 (2014), pp. 1842–1850.

[101] V.F-G. Tseng, S.S. Bedair, and N. Lazarus. "Phased array focusing for acoustic wireless power transfer". In: *IEEE transactions on ultrasonics, ferroelectrics, and frequency control* 65.1 (2018), pp. 39–49.

[102] K.L. Gentry and S.W. Smith. "Integrated catheter for 3-D intracardiac echo cardiography and ultrasound ablation". In: *ieee transactions on ultrasonics, ferroelectrics, and frequency control* 51.7 (2004), pp. 800–808.

[103] M. Wang et al. "Design and test of a monolithic ultrasound-image-guided HIFU device using annular CMUT rings". In: *Ultrasonics Symposium, 2008. IUS 2008. IEEE*. IEEE. 2008, pp. 459–462.

[104] H.Y. Song et al. "A study on the beamforming system with reconfigurable focusing depth for ultrasound-enhanced thrombolysis". In: *RF and Wireless Technologies for Biomedical and Healthcare Applications (IMWS-Bio), 2014 IEEE MTT-S International Microwave Workshop Series on*. IEEE. 2014, pp. 1–3.

[105] S. Akhbari. "Curved and bimorph piezoelectric micromachined ultrasonic transducers (PMUT)". Ph.D. Thesis. University of California Berkeley, 2016.

Appendix A

Evaluation of Self-radiation Impedance

The difficulty in evaluating (3.69) for the acoustic impedance is mostly due to the inner (bracketed) double integral. This integral, which we will denote $I_1(r)$ to explicitly state its dependency on r, is essentially a scaled pressure profile:

$$Z_a = j\rho_a c_a k \int_a^b I_1(r)\phi(r)r \, dr \tag{A.1}$$

$$I_1(r) = \iint_{A_v} \phi(r',\theta')e^{-jkr'} \, dr'd\theta, \tag{A.2}$$

where $\sqrt{r^2 + r'^2 - 2rr'\cos\theta'}$ is substituted for r in (3.15) to express the modeshape in terms of r' and θ'. At this point, an evaluation approach that accounts for the interdependence of the integration limits on r' and θ' must be devised. Attempting to directly integrate (A.2) by evaluating every function at every point and frequency can result in burdensome computation times, so some reformulation is desired. In this aim, we note that the exponential (phase) term in (A.2) is constant in θ', and can therefore factor θ' from the integration:

$$I_1(r) = 2 \int_0^{r+b} e^{-jkr'} \left[\int_{\theta'_a}^{\theta'_b} \phi(r',\theta') \, d\theta' \right] dr'. \tag{A.3}$$

Conceptually, this approach amounts to dividing A_v into infinitesimal circular strips that are each centered at a point at radius r (see Figure A.1), integrating the modeshape over all values of θ' on a given strip, then integrating over all strips. The factor of 2 reflects the fact that integrating over the specified range of θ' only accounts for half of the vibrating area. As shown in Figure A.1, depending upon whether or not the points $(r',\theta'=0)$ and $(r',\theta'=\pi)$ are in the domain A_v, four situations corresponding to four separately defined integration limits on θ' can occur. These four cases are summarized in Table A.1, and combined with (A.4) and (A.5), define the piecewise constant integration limits:

$$\theta'_a = \cos^{-1}\left((r^2 + r'^2 - a^2)/2rr'\right) \tag{A.4}$$

$$\theta'_b = \cos^{-1}\left((r^2 + r'^2 - b^2)/2rr'\right). \tag{A.5}$$

With the integration limits fully defined, (A.3) may be integrated numerically according to a method of choice. For the purposes of this dissertation, all integrals were approximated using the trapezoidal rule in Matlab, and the functions were evaluated at evenly spaced intervals between the integration limits, with 20 points in r, 100 points in r', and 100 points in θ'.

Table A.1: Summary of piecewise integration limits used to evaluate self-radiation impedance.

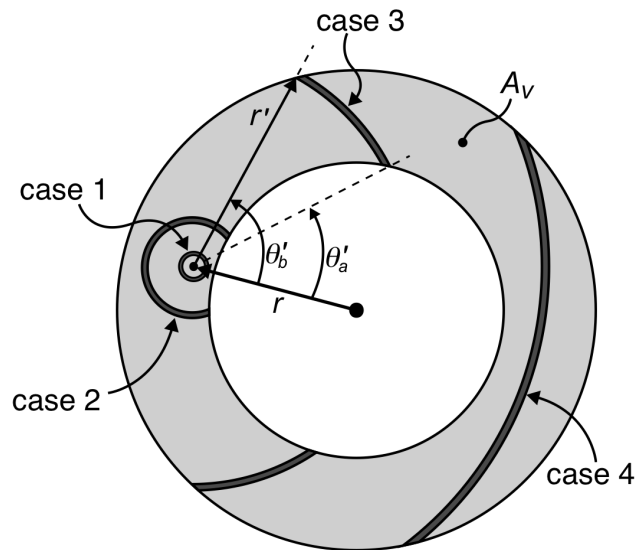| Case Number	Criteria	Integration Limits θ'_a	θ'_b
1	$r' < r - a$ and $r' < b - r$	0	π
2	$r' > r - a$ and $r' < b - r$	(A.4)	π
3	$r' > r - a$ and $r' > b - r$	(A.4)	(A.5)
4	$r' < r - a$ and $r' > b - r$	0	(A.5)

Figure A.1: Illustration of geometry and approach to numeric evaluation of the self-radiation impedance.